

Institut für Angewandte Physik
Fakultät für Mathematik und Naturwissenschaften
Technische Universität Dresden

Vapor Phase Growth of ZnO Single Crystals/Thin Films and Attempts for p-type Doping

Dissertation
Zur Erlangung des akademischen Grades
Doctor rerum naturalium

vorgelegt von

MSc Xi Zhang

geboren am 16.01.1982 in Xinyang, China

Eingereicht am 26.08.2013
Verteidigt am 03.03.2014

Gutachter 1: Prof. Dr. J. Weber
Gutachter 2: Prof. Dr. P. Schmidt

Contents

Abstract	1
Kurzfassung	3
Chapter 1 Introduction	5
Chapter 2 Basic properties of ZnO	9
2.1 Crystal structure	9
2.2 Electronic structure	12
2.3 Optical properties	15
2.3.1 Free exciton transition	16
2.3.2 Bound exciton transition	17
2.3.3 Two-electron-satellite transition	20
2.3.4 Donor-acceptor-pair transition	21
2.3.5 Phonon assisted recombination.....	22
2.4 Defects in ZnO	23
2.4.1 Intrinsic point defects.....	23
2.4.2 Extrinsic point defects	25
2.4.3 Extended defects.....	26
Chapter 3 Growth methods and experimental techniques	29
3.1 Growth methods of ZnO single crystals	29
3.1.1 Hydrothermal growth.....	29
3.1.2 Melt growth	31
3.1.3 Seeded chemical vapor transport growth.....	33
3.1.4 Open-system physical vapor transport growth	33
3.2 Growth methods of ZnO thin films	34
3.2.1 Review of main approaches for growing ZnO films.....	34
3.2.2 Vapor phase transport method for growing ZnO films	38
3.3 Processing techniques of ZnO samples	38
3.4 Characterization techniques of ZnO single crystals/thin films	40
3.4.1 Photoluminescence	40
3.4.2 X-ray diffraction analysis	43
3.4.3 SEM, EBSD and Cathodoluminescence	43
3.4.4 Electrical conductivity measurement.....	44
Chapter 4 Vapor phase growth of ZnO single crystals	45
4.1 Introduction	45
4.2 Growth principles and growth setup	45

4.3 Results	50
4.4 Dominant factors in crystal growth.....	55
4.4.1 Growth duration.....	55
4.4.2 Growth temperatures.....	56
4.4.3 Gas flow rates.....	57
4.4.4 Source material	59
4.5 Discussion.....	62
4.6 Conclusion	64
Chapter 5 Vapor phase growth of ZnO thin films on Si substrates.....	65
5.1 Introduction	65
5.2 Growth principles and growth setup	65
5.3 Results	69
5.4 DAP transitions in the as-grown films	74
5.5 Discussion.....	77
5.6 Conclusion	78
Chapter 6 Two unidentified PL emissions in vapor phase grown ZnO single crystals.....	79
6.1 Introduction	79
6.2 Details of the peak at 3.3643 eV	79
6.3 Details of the peak at 3.3462 eV	83
6.4 Isochronal annealing after hydrogenation	83
6.5 Possible microscopic origins of the peak at 3.3643 eV and 3.3462 eV	85
6.6 Conclusion	86
Chapter 7 Attempts for p-type doping in ZnO	87
7.1 Status of p-type doping in ZnO.....	87
7.2 Our attempts for p-type doping by nitrogen.....	92
7.2.1 Nitrogen doping from DC plasma.....	92
7.2.2 Nitrogen doping from RF plasma	94
7.3 Our attempts for p-type doping by antimony	95
7.4 Conclusion	97
Chapter 8 Outlook.....	99
Bibliography	102
Acknowledgement.....	114

List of Figures

Figure 2.1: Stick-and-Ball representation of ZnO crystal structure, (a) cubic rocksalt(B1), (b) cubic zinc blende (B3), and (c) hexagonal wurtzite (B4). Shaded gray and black spheres denote Zn and O atoms, respectively.....	9
Figure 2.2: The wurtzite structure of ZnO. O atoms are shown as larger gray spheres, Zn atoms as smaller black spheres. One unit cell is outlined for clarity	11
Figure 2.3: The band structures of wurtzite ZnO including spin-orbit interaction.....	13
Figure 2.4: Schematic band structure and symmetry of wurtzite ZnO, the three separate valence bands are due to spin-orbit interaction and crystal field splitting.....	14
Figure 2.5: Schematic diagram of neutral donor bound exciton complex [.....	18
Figure 2.6: A typical PL spectrum of ZnO single crystal measured at 4.2 K.....	18
Figure 2.7: A schematic drawing of the energy ranges of various bound excitons with the level scheme for the two-electron-satellites transition [.....	20
Figure 2.8: Formation energies as a function of Fermi-level position for native defects in ZnO. Results for both Zn-rich and O-rich conditions are shown [42].	24
Figure 3.1: Schematic illustration of autoclave for hydrothermal growth method.....	30
Figure 3.2: (a) schematic system of the pressurized melt growth and (b) schematic system of Bridgman growth with iridium crucible	32
Figure 3.3: Typical horizontal cylindrical ampoule for seeded chemical vapor transport growth	33
Figure 3.4: Schematic description of a PLD experimental set-up.....	35
Figure 3.5: Schematic diagram of an RF assisted MBE system.....	36
Figure 3.6: Schematic illustration of an RF magnetron sputtering system with DC power supply	37
Figure 3.7: Schematic illustration of vapor transport method for growing ZnO films on Si....	38
Figure 3.8: Sketch of the remote DC plasma setup	39
Figure 3.9: Sketch diagram of two different RF plasma setup: a) N ₂ plasma and b) N ₂ O plasma	40
Figure 3.10: Typical photoluminescence setup using He-Cd laser 325 nm excitation	41
Figure 4.1 Illustration of the open-system vapor transport process for ZnO single crystals growth in horizontal Al ₂ O ₃ tube and ZnO cone.....	46
Figure 4.2 (a) the growth tube of open-system vapor transport method in HT-1800 furnace, and (b) the temperature profile in the growth tube	48
Figure 4.3: Illustration of the open-system vapor transport process for ZnO single crystals growth using a ZnO ceramic tube	49
Figure 4.4: Illustration of the open-system vapor transport process for ZnO single crystals growth using an Al ₂ O ₃ ceramic tube	49
Figure 4.5: (a) original Al ₂ O ₃ ceramic tube, and (b) coated Al ₂ O ₃ ceramic tube with a layer of ZnO	49
Figure 4.6: Clusters of ZnO single crystals grown by vapor transport method using (a)~(b) only ZnO tube, (c) Al ₂ O ₃ tube + ZnO cone, (d) only Al ₂ O ₃ tube.....	50
Figure 4.7: (a) Typical as-grown needle-shaped ZnO single crystals and (b) SEM image of the	

surface morphology of a ZnO crystal labeled with the indices of crystalline planes51

Figure 4.8: (a) Kikuchi pattern of the as-grown crystals by electron backscatter diffraction (SEM-EBSD) technique, and (b) orientation of the crystal geometry with axial polar direction and surrounding crystalline planes.....51

Figure 4.9: Comparison of PL spectra of two samples grown under different growth conditions (for the growth details see Table 4.2); Inset presents a wider range PL spectra of the two samples (the intensities of the green band were multiplied by a factor of 40 for sample (a) and a factor of 4 for sample (b) for better clarity)52

Figure 4.10: Room temperature cathodoluminescence of needle crystal grown by vapor transport method.....53

Figure 4.11: PL spectra measured at 4.2 K for the comparison ZnO single crystals between (a) HT crystals purchased from Crystec GmbH and (b) one of our vapor phase grown crystals.....54

Figure 4.12: (a) The growth of ZnO crystals by vapor phase method at different duration hours while keeping other parameters the same56

Figure 4.13: The growth of ZnO crystals by vapor phase method at different temperatures while keeping other parameters the same57

Figure 4.14: The growth of ZnO crystals by vapor phase method at different N₂ flow rates while keeping other parameters the same58

Figure 4.15: The weight loss of source ZnO pellets vs. furnace temperature at following conditions (a) flow rates $f_{N_2} = 0.800$ slm, $f_{H_2} = 12$ sccm, $f_{O_2} = 12$ sccm, growth duration $t = 1$ h and (b) flow rates $f_{N_2} = 1.250$ slm, $f_{H_2} = 15$ sccm, $f_{O_2} = 3$ sccm, growth duration $t = 1$ h.....59

Figure 4.16: The weight loss of source ZnO pellets vs. N₂ flow rate at following conditions (a) furnace temperature $T = 900$ °C, flow rates $f_{H_2} = 6$ sccm, $f_{O_2} = 6$ sccm, growth duration $t = 1$ h and (b) furnace temperature $T = 1400$ °C, flow rates $f_{H_2} = 15$ sccm, $f_{O_2} = 3$ sccm, growth duration $t = 1$ h.60

Figure 4.17: The weight loss of source ZnO pellets vs. H₂ flow rate at following conditions (a) furnace temperature $T = 900$ °C, flow rates $f_{N_2} = 0.800$ slm, $f_{O_2} = 6$ sccm, growth duration $t = 1$ h and (b) furnace temperature $T = 1400$ °C, flow rates $f_{N_2} = 1.200$ slm, $f_{O_2} = 15$ sccm, growth duration $t = 1$ h61

Figure 4.18: The weight loss of source ZnO pellets vs. O₂ flow rate at following conditions (a) furnace temperature $T = 900$ °C, flow rates $f_{N_2} = 0.650$ slm, $f_{H_2} = 6$ sccm, growth duration $t = 1$ h and (b) furnace temperature $T = 1400$ °C, flow rates $f_{N_2} = 1.200$ slm, $f_{H_2} = 20$ sccm, growth duration $t = 1$ h61

Figure 4.19: The influence of supersaturation on the nucleation rate, growth rate and crystal size [.....62

Figure 4.20: Dendritic growth by high supersaturation of zinc vapor.....63

Figure 5.1: Illustration of the open-system vapor transport process for ZnO thin films on Si substrates in horizontal concentric Al₂O₃ tubes with ZnO powders as source materials66

Figure 5.2: Illustration of the open-system vapor transport process for ZnO thin films on Si substrates in horizontal concentric Al₂O₃ tubes with Zn powders as source materials ..68

Figure 5.3: Illustration of the open-system vapor transport process for ZnO thin films on Si substrates in horizontal concentric Al₂O₃ tubes with H₂O as the oxidizer and Zn powders

as source materials.....	68
Figure 5.4: Typical SEM image of ZnO thin films on Si substrates grown by the type I vapor phase method, the image (b) is an enlargement of the central area in the image (a) ...	69
Figure 5.5: The XRD spectra of a ZnO thin film on (100) Si substrates grown by the type I vapor phase method	70
Figure 5.6: The PL spectra of an ZnO thin film on Si substrates grown by the type I vapor phase method, the insert shows the spectra of wider range from UV to visible.....	70
Figure 5.7: Typical SEM image of ZnO thin films on Si substrates grown by the type II vapor phase method, the image (b) is an enlargement of the central area in the image (a) ...	71
Figure 5.8: The XRD spectra of ZnO thin films on a) (100) Si substrates and b) (111) Si substrates grown by the type II vapor phase method	71
Figure 5.9: (a) The PL spectra of ZnO thin film on Si substrates grown by the type II vapor phase method, the insert shows the spectra of wider range from UV to visible; (b) The excitation dependent PL spectra in the range between 3.138 eV and 3.308 eV of the same sample	72
Figure 5.10: Typical SEM image of ZnO thin films on Si substrates grown by the type III vapor phase method, (b) is the enlargement of image (a), and (c) is the image of the cross-section	72
Figure 5.11: The XRD spectra of ZnO thin films on (111) Si substrates grown by the type III vapor phase method	73
Figure 5.12: The PL spectra of ZnO thin film on Si substrates grown by the type III vapor phase method, the insert shows the spectra of wider range from UV to visible.....	73
Figure 5.13: The temperature dependent PL spectra of the ZnO films grown by the type III vapor phase method at the bound excitonic range, the insert plots the integrated intensity of the 3.367 eV peak vs. $1000/T$, where T is the measurement temperature in Kelvin.....	74
Figure 5.14: The excitation power dependent PL spectra of the as-grown ZnO thin films grown by the type II vapor phase method	75
Figure 5.15: The temperature dependent PL spectra of the as-grown ZnO thin films grown by the type II vapor phase method.....	76
Figure 5.16: The integrated intensities of the DAP broad peak and the peak at 3.314 eV. vs. $1000/T$, where T is the measurement temperature in Kelvin.	76
Figure 6.1: The PL spectra of an as-grown ZnO single crystal grown by vapor phase method, the spectra of the TES region was multiplied by a factor of 30 for better clarity	80
Figure 6.2: The linear relationship between the TES splitting and the corresponding donor binding energy [11], The P1 line and four other shallow donors (I4, I6, I9 and I10) are depicted according their donor binding energies	81
Figure 6.3: The temperature dependent PL spectra of the vapor phase grown ZnO crystals, and the insert shows the intensity of P1 line vs. the measurement temperature.....	82
Figure 6.4: The PL spectra of ZnO crystal sample after annealing in Ar atmosphere at different temperature up to 900 °C.....	82
Figure 6.5: PL spectra of the hydrogenated (red curve) and as-grown (blue curve) ZnO crystal samples in the range of (a) 3.38~ 3.35 eV and (b) 3.35~ 3.30 eV	83
Figure 6.6: The PL spectra of the hydrogenated ZnO crystal sample after annealing at	

different temperatures from 75 °C to 195 °C (a) at the bound exciton range and (b) at the TES region84

Figure 6.7: The normalized intensity of the P2 line and the TES of H_{BC} line at different annealing temperatures.....84

Figure 7.1: The alignment of the valence band maximum (VBM) and the conduction band minimum (CBM) of various semiconductors including ZnO, the dashed line indicates the universal level of hydrogen at the absolute energy scale87

Figure 7.2: (a) Formation energy as a function of Fermi level E_F for N_O in ZnO under Zn-rich conditions. E_F is referenced to the VBM, and the position of the (0/-) acceptor level is indicated. (b) Configuration coordinate diagram indicating optical absorption and emission energies for exchanging an electron with the conduction band.....89

Figure 7.3: Schematic dependence of the formation energy of charged defects on the Fermi energy position91

Figure 7.4: The PL spectra of the ZnO crystal sample (a) virgin sample and (b) sample after the N₂ DC plasma treatment at 300 °C, the insert shows wider range of spectra of both samples.93

Figure 7.5: The below band gap excitation PL spectra of the ZnO crystal sample (a) virgin, (b) after the N₂ RF plasma treatment at 150 °C, (c) after the N₂O RF plasma treatment at 200 °C95

Figure 7.6: The SEM images of Sb doped ZnO films by the type II vapor phase method with different molar ratio between Zn and Sb: (a) 5, (b) 15, and (c) 30.....96

Figure 7.7: The PL spectra of Sb doped ZnO films by the type II vapor phase method with different molar ratio between Zn and Sb: (a) 5, (b) 15, and (c) 30.....96

List of Tables

Table 2.1: Free and bound exciton recombinations and related properties of ZnO [1]19

Table 4.1: Chemical composition of the ZnO powder and Al₂O₃ ceramic tube47

Table 4.2: Growth parameters of two different crystals(a) and (b) used in PL measurement shown in Figure 4.952

Table 5.1: The dimensions of the Al₂O₃ growth tubes.....66

Table 6.1: The TES splitting of the P₁ line at 3.3643 eV.....81

Table 7.1: Summary of successful attempts to grow p-type doped ZnO [161]88

Abstract

The growth of ZnO single crystals and ZnO thin films on Si substrates by an open-system vapor phase method was studied in this thesis. The as-grown ZnO single crystals were investigated by means of photoluminescence (PL). Two unique emissions were observed in virgin and hydrogenated crystals. The up-to-now attempts for the p-type doping of ZnO were summarized and our doping studies were performed using nitrogen and antimony.

The seed-free and open-system vapor phase method is a simple and low cost approach to grow good quality ZnO single crystals. The growth parameters, including flow rates of N₂, H₂, O₂, and growth temperatures, have various influences on the crystal growth, and also on the optical properties of the as grown crystals. The as-grown crystals are c-axis oriented needle crystals, and the crystals typically have a maximum length of 40 mm and a maximum diameter of 1 mm. The needle-shaped crystals are n-type with main donors due to Al, Ga, and In impurities, as determined from the PL spectra.

Two unidentified PL emission lines (P₁ at 3.3643 eV and P₂ at 3.3462 eV) are observed in our vapor phase grown ZnO single crystals. P₁ is attributed to the recombination of an exciton bound to a shallow donor, which has a binding energy of 42.2 meV. Hydrogenation of the as-grown ZnO single crystal leads to the appearance of the P₂ line and a great reduction of the P₁ line. Subsequent isochronal annealing in the ambient atmosphere leads to gradual reduction of P₂ and the reappearance of P₁. The PL measurements indicate that hydrogen is involved in the defect origins of the P₂ line.

ZnO thin films were deposited on Si substrates by the vapor phase method. Three different types of configurations with alternative source materials and oxidizers were employed and compared. It is demonstrated that, methods with lower growth temperatures are easier to deposit homogenous ZnO films on Si substrate. Donor-acceptor-pair (DAP) transition at 3.245 eV and its phonon replicas were

observed in the PL spectra of the thin films, which are grown by the hydrogen-free vapor phase method. The appearance of DAP transition indicates the presence of acceptor in the films.

The long-standing challenge of p-type doping in ZnO is mainly attributed to the low valence band maximum (VBM) at the absolute energy scale, the spontaneous formation of compensating defects and the lack of appropriate acceptors with small ionization energy. Two attempts for the p-type doping of ZnO were performed by nitrogen diffusion into ZnO single crystals from plasma after the growth or by *in-situ* doping antimony during the growth of ZnO films. No hole conductivity could however be achieved in our doped samples.

Kurzfassung

In dieser Arbeit wurde das Wachstum von ZnO-Einkristallen und Dünnschichten auf Si durch chemische Gasphasenabscheidung in einem offenen System untersucht. Die hergestellten ZnO-Einkristalle wurden mit Photolumineszenzmessungen (PL) untersucht. Es konnten sowohl in unbehandelten als auch in mit Wasserstoff behandelten Proben zwei charakteristische Linien beobachtet werden. Sowohl die bisherigen Versuche zur p-Typ Dotierung von ZnO als auch die in dieser Arbeit durchgeführten Versuche mit Stickstoff und Antimon werden zusammengefasst und präsentiert.

Die Keimkristall-freie Gasphasenabscheidung (CVD) in offenen Systemen ist eine einfache und kostengünstige Methode zur Herstellung von qualitativ hochwertigen ZnO-Einkristallen. Die Wachstumsparameter, einschließlich der Flussraten von N_2 , H_2 und O_2 sowie der Wachstumstemperatur beeinflussen das Kristallwachstum sowie die optischen Eigenschaften der hergestellten Kristalle. Die hergestellten Kristalle wachsen typischerweise als entlang der c-Achse orientierte Nadeln mit Längen von bis zu 40 μm und Durchmessern von bis zu 1 μm . Die nadelförmigen Kristalle besitzen eine n-Typ Dotierung, welche hauptsächlich durch Verunreinigung mit Al, Ga und In verursacht wird.

Zwei bisher nicht identifizierte PL-Linien (P_1 bei 3,3643 eV und P_2 bei 3,3462 eV) wurden in den hergestellten Kristallen beobachtet. P_1 wird der Rekombination von Exzitonen an flachen Donatoren mit einer Bindungsenergie von 42,2 meV zugeordnet. Eine Wasserstoffbehandlung der hergestellten Kristalle führt zum Erscheinen der P_2 -Linie und einer starken Unterdrückung der P_1 -Linie. Anschließende isochronische Temperung in Luft führt zu einer schrittweisen Reduzierung der Intensität der P_2 -Linie und zu einer Verstärkung der P_1 -Linie. Photolumineszenzmessungen weisen auf eine Korrelation von P_2 mit Wasserstoff hin.

Zusätzlich wurden mit der CVD-Methode dünne ZnO-Schichten auf Si-Substraten abgeschieden. Drei unterschiedliche Konfigurationen mit verschiedenen Ausgangsmaterialien (ZnO-Pulver bzw. Zn-Pulver) und verschiedenen Oxidationsmitteln (O_2 bzw. Wasser) wurden untersucht und verglichen. Es wird gezeigt, dass mit den Konfigurationen mit geringerer Wachstumstemperatur am einfachsten homogene ZnO-Schichten auf Si abgeschieden werden können. Ein

Donator-Akzeptor-Paar-Übergang (DAP) bei 3,245 eV und die dazugehörigen Phononenrepliken wurden in den Schichten beobachtet, welche in einer Wasserstoff-freien Konfiguration abgeschieden wurden. Diese DAP-Übergänge sind ein Hinweis auf die Anwesenheit von Akzeptoren.

Die seit langem bestehende Herausforderung der p-Typ-Dotierung von ZnO hat ihre Wurzeln hauptsächlich in dem niedrig liegenden Valenzbandmaximum (VBM) auf der absoluten Energieskala, der spontanen Bildung von kompensierenden Defekten sowie dem Mangel an geeigneten Akzeptoren mit geringer Ionisierungsenergie. Zwei Versuche zur p-Typ-Dotierung von ZnO durch Behandlung der Kristalle mit N-Plasma bzw. durch *in-situ* Dotierung mit Sb während des Kristallwachstums wurden durchgeführt. Allerdings konnte damit keine nachweisbare Löcherleitung in den behandelten Proben erreicht werden.

Chapter 1

Introduction

ZnO has gained much attention as a promising semiconductor material for short-wavelength optoelectronic devices, such as transparent conductive oxides (TCO) [1], light emitting diodes (LED) [2], laser diodes [3] and solar cells [4, 5], because of its large exciton binding energy (60 meV), wide band gap (3.4 eV) at room temperature, and the availability of large area ZnO substrates [6]. However, some prospective applications of ZnO-based devices are hindered by the p-type doping problems in ZnO. The reasons for the difficulties of p-type doping can be briefly summarized into four points: i) Background donors and spontaneously formed defects compensate acceptors; ii) Acceptors in ZnO are located too deeply in the bandgap; iii) The solubility of p-type impurities is too low; iv) Hydrogen, as an always existing contamination, passivates acceptors by forming inactive acceptor-hydrogen complexes.

The growth of ZnO single crystals are typically achieved by three traditional methods: hydrothermal growth, melt growth and seeded chemical vapor transport [6]. To solve the fundamental problem of p-type doping in ZnO, the growth and doping of ZnO single crystals and thin films by vapor phase method were investigated. Hydrothermal growth provides the largest commercial available wafers, but inevitably results in the incorporation of alkali metals (Li and K) from aqueous mineralizers, which can seriously deteriorate the electrical properties of ZnO wafers [7]. Melt growth is still considered to be at the developing stage and suffers from the presence of grain boundaries in the crystals [8, 9]. Seeded chemical vapor transport provides the purest crystals among these three approaches, but encounters high costs due to low production rate, and nonconstant growth conditions due to the closed growth system [10]. A simple and low cost vapor phase method will be employed in this thesis, which can provide high purity ZnO needle crystals with good crystalline quality and flexibility in doping.

The integration of traditional silicon technology and future ZnO optoelectronics require the heteroepitaxial growth of ZnO thin films on Si substrate. It is more difficult than the deposition on hexagonal substrates for two reasons: i) the mismatch of the cubic and hexagonal crystal structures, ii) the appearance of SiO_x amorphous layers between Si substrate and ZnO films. We will show in this thesis that the open-system vapor phase method is capable of growing homogenous ZnO films on Si substrate. Three different types of configurations with alternative source materials and oxidizers were employed and compared. The DAP transition at 3.245 eV and its phonon replicas were observed in the deposited films, which were grown by hydrogen-free vapor phase method. The appearance of DAP transition indicates the presence of acceptors in the films.

In ZnO there are still many mysteries regarding the defect origins of the various sharp lines in the excitonic spectrum. Most origins of these sharp lines are donor impurities [11]. Reducing or removing these donor impurities can reduce the compensation and passivation of acceptors. Thus understanding these sharp emissions is important for solving the p-type doping problems. Two unidentified PL emissions (P₁ at 3.3643 eV and P₂ at 3.3462 eV) were observed in the as-grown and hydrogenated ZnO needle crystals. P₁ is demonstrated to originate from shallow donors. Further isochronal annealing of hydrogenated crystals suggests that hydrogen is involved in the microscopic origin of the P₂ line.

The substitutional atom (group V element N) at oxygen sites was believed to be the most promising candidate for shallow acceptor [6], however, recent calculations pointed out that N_O is actually a deep acceptor and has no contribution to the hole concentration at room temperature [12]. P, As, and Sb atoms at oxygen sites are also deep acceptors because of their larger ion radii size and larger lattice distortion [13]. In spite of this knowledge, defect complexes, such as Li_{Zn}-N_O, X_{Zn}-2V_{Zn} (X = P, As, Sb) were suggested to act as shallow acceptors [14, 15]. In order to introduce above acceptor complexes, two attempts for the p-type doping of ZnO were carried out by nitrogen diffusion into ZnO single crystals from plasma or by *in-situ* doping antimony during the growth of ZnO films.

The present thesis will be structured as following: Chapter 2 will give a short introduction of the fundamental considerations of ZnO as a semiconductor material. This chapter covers the crystal structure, electronic band structure, optical properties of ZnO materials, also the defects in ZnO, and the doping issues of ZnO. Chapter 3 deals with the general growth techniques for ZnO single crystals/thin films, and the techniques for sample processing and characterization. The following four chapters will present the experimental results: Chapter 4 describes the growth of ZnO single crystals by the open-system vapor transport method. Chapter 5 deals with the growth of ZnO thin films on silicon substrate by the vapor phase method. Chapter 6 focuses on two unidentified PL emissions at 3.3643 eV and 3.3462 eV in the virgin and hydrogenated crystals, which were grown by the vapor phase method. Chapter 7 summarizes the present knowledge of p-type doping in ZnO and presents doping study using nitrogen and antimony. Finally, chapter 8 summarizes the presented results and outlines remaining open questions of this thesis.

Chapter 2

Basic properties of ZnO

The first research of ZnO as a semiconductor material can be dated back to the 1930s [16], however, an enormous growth of ZnO related researches was witnessed in recent decades [6, 17, 18]. In this chapter, the basic properties of ZnO will be summarized.

2.1 Crystal structure

ZnO is a typical II-VI binary compound semiconductor. It has three different types of crystal structures: hexagonal wurtzite (B4) [19], cubic zinc-blende (B3) [20, 21] and rocksalt (B1) [22, 23], as illustrated in Figure 2.1. At ambient pressure, ZnO exclusively crystallizes in the hexagonal wurtzite structure. Zinc-blende ZnO is stable only by epitaxial growth on cubic substrates, while the rocksalt structure is a high-pressure metastable phase forming under ~ 10 GPa. Theoretical calculations also predicted that a fourth phase, B2 (cubic CsCl structure), may be possible at extremely high pressures (260 GPa), however, this phase has not yet been experimentally

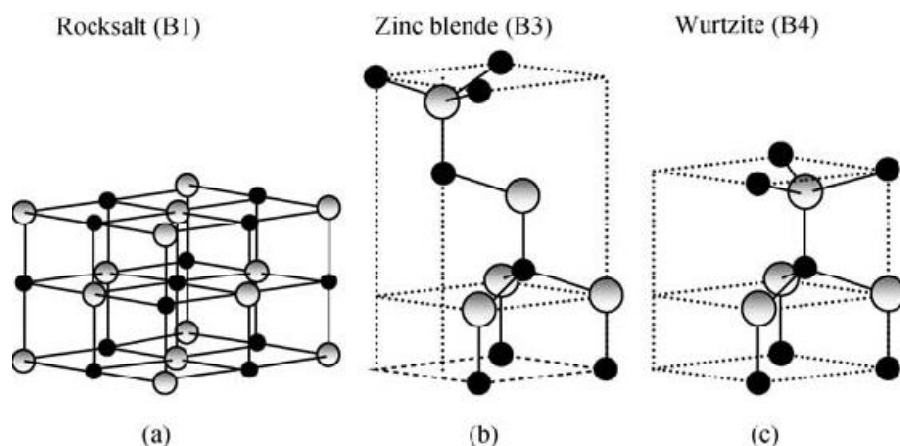


Figure 2.1: Stick-and-Ball representation of ZnO crystal structure, (a) cubic rocksalt(B1), (b) cubic zinc blende (B3), and (c) hexagonal wurtzite (B4). Shaded gray and black spheres denote Zn and O atoms, respectively [6].

observed [24].

Both zinc-blende and wurtzite structures have a tetrahedrally coordinated bonding geometry: each zinc ion has four oxygen neighbor ions in a tetrahedral configuration and vice versa. This geometrical arrangement, which is well known from, for example, the group-IV elements C (diamond), Si, Ge, is also common for II-VI and III-V compounds. The tetrahedral coordination is typical of sp^3 covalent bonding nature, but these materials may also have a substantial ionic character that tends to increase the bandgap beyond the one expected from the covalent bonding.

The main difference between the zinc-blende and wurtzite structure is the stacking sequence of Zn and O atoms bi-layers: (ABCABC \cdots) cubic close packing for the former and (ABAB \cdots) hexagonal close packing for the latter. The Zn-O bond has a fraction of ionic character, wurtzite ZnO has a mixture of ionic bonding and covalent bonding [20]. The zinc-blende ZnO has lower ionicity and is more covalent, compared to the wurtzite ZnO [25].

The zinc-blende structure shown in Figure 2.1b could be regarded as an arrangement of two interpenetrating face-centered cubic sub-lattices, displaced by 1/4 of the body diagonal axis. The primitive unit cell of zinc-blende is an oblique parallelepiped and contains one pair of ions, Zn^{2+} and O^{2-} . In Group theory, this lattice is classified by the point group $\bar{4}3m$ (international notation) or T_d (Schoenflies notation) and by its space group, denoted as $F\bar{4}3m$ or T_d^2 , respectively [26]. The zinc-blende ZnO thin layers can be grown on cubic zincblende substrates and zincblende ZnS thin layers are always used as the interlayers and/or nucleation layer due to a lack of suitable substrates with small lattice-mismatch. In a few reports, GaAs(001) substrate plus ZnS buffer layer with molecular-beam epitaxy [27, 28], $Al_2O_3(0001)$ substrate plus ZnS interlayer with thermal oxidation method [29] and Pt(111)/Ti/SiO₂/Si(100) substrates with sol-gel process [30] were used to synthesize zinc-blende ZnO layer. However, the single crystalline zinc-blende ZnO layer is still a challenge because of the strong tendency to form wurtzite subdomains within the zincblende matrix. The theoretically calculated lattice parameter for zinc-blende ZnO is 4.57-4.62 Å [31, 32], while the value estimated experimentally is 4.47 Å [27] and

4.18 Å [29] from different research groups.

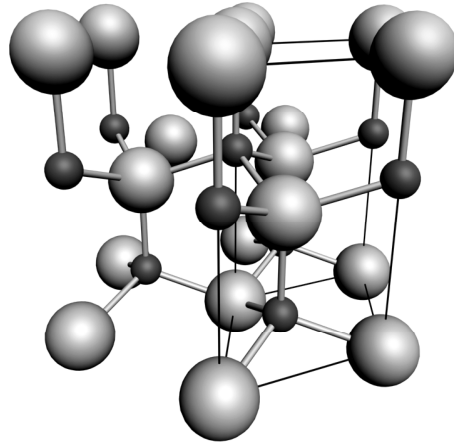


Figure 2.2: The wurtzite structure of ZnO. O atoms are shown as larger gray spheres, Zn atoms as smaller black spheres. One unit cell is outlined for clarity. [33]

In contrast to the cubic zinc-blende geometry, the hexagonal wurtzite lattice is uniaxial as shown in Figure 2.1c and Figure 2.2. The tetrahedral coordination in wurtzite structure gives rise to polar symmetry along the hexagonal axis (c axis in ZnO). This polarity is responsible for a number of the properties of ZnO, including its piezoelectricity and spontaneous polarization, and is also a key factor in crystal growth, etching and defect generation [33, 34]. The orientation of axes and faces in a wurtzite lattice is denoted by four-digit Miller indices $hkil$ ($i = -(h+k)$). The c -axis direction is referred to as $[0001]$, the surface perpendicular to the c -axis is the hexagonal (0001) plane. The Zn-terminated (0001) and O-terminated $(000\bar{1})$ faces are known to possess different chemical and physical properties [35].

The wurtzite lattice type is classified by the point group $6mm$ (international notation) or C_{6v} (Schoenflies notation) and by the space group $P6_3mc$ or C_{6v}^4 , respectively [26]. The lattice parameter of the hexagonal unit cell are $a = 3.2495$ Å and $c = 5.2069$ Å. From powder X-ray diffraction data taken between 4.2 K and 296 K, the temperature dependence of lattice parameters could be fitted by a [Å] = $3.24835 - 1.0811 \cdot 10^{-5} \cdot T + 6.820 \cdot 10^{-8} \cdot T^2 - 6.109 \cdot 10^{-11} T^3 + 2.143 \cdot 10^{-14} T^4$ [36]. The solid density at room temperature is 5.606 g/cm³, which corresponds to the atom concentration of

zinc or oxygen with $4.0 \times 10^{23}/\text{cm}^3$.

Rocksalt ZnO (schematically shown in Figure 2.1a) crystallizes in solid sodium chloride cubic structure; each ion is surrounded by six ions of the opposite charge as expected on electrostatic grounds. Because the reduction of lattice dimensions causes the interionic coulomb interactions to favor the ionicity more over the covalent nature, hexagonal wurtzite ZnO (B4) can be transformed to cubic rocksalt (B1) at relatively modest external hydrostatic pressures [6]. The space group symmetry of the rocksalt type of structure is $Fm\bar{3}m$ in the Hermann-Mauguin notation and O_{5h} in the Schoenflies notation [26], and the lattice constant is between 4.27-4.29 Å [6]. This structure has a sixfold coordination and a considerably enhanced space-filling factor. The pressure-induced phase transition from the wurtzite ZnO (B4) to the rocksalt (B1) occurs at approximately 10 GPa and a large volume shrinkage of about 17% also happens in this process [37, 38]. Defect doping can help to reduce the transition pressure, for example, 2at.% Mn-doped ZnO can reduce the onset transition from 9.5 GPa to 6 GPa, as compared to pure ZnO samples [39].

In conclusion, although ZnO shares three different types of crystalline structures with different properties, wurtzite ZnO is the most stable form at room temperature and atmospheric pressure. All the measured and discussed ZnO samples in following sections and chapters will be of wurtzite form.

2.2 Electronic structure

The knowledge of the electronic band structure is important when investigating the electrical and optical properties of semiconductor, or when evaluating materials for semiconductor devices. Several theoretical approaches with varying degrees of complexity and different simplified assumptions have been employed to calculate the band structure of ZnO (mainly for wurtzite). Among these calculations, density-functional theory within the local density approximation (LDA) [40, 41] method is mostly employed, however, the results of standard LDA calculations show distinct shortcomings, such as underestimated lattice constant, underestimated

bandgap [18, 42]. Several attempts have been made to adjust and correct the calculations. Some of the corrections are based on empirical reasoning or on a rigid shift of the conduction band [43]; others are based on non-self-consistent approaches [44], LDA+ U [45, 46], or calculations using a hybrid functional [47]. Besides the theoretical approaches, a number of sophisticated experimental methods have been employed to explore the band structure of wurtzite ZnO. Typically, angle-resolved photoelectron spectroscopy (ARPES) technique together with synchrotron radiation excitation have been commonly recognized as a powerful tool that enables the determination of experimental bulk and surface electronic band structures under the assumptions of k -conservation and nearly free electron model [48]. The combination of theoretical and experimental techniques allows determining a reliable band structure of wurtzite ZnO.

The calculated band structures of wurtzite ZnO including spin-orbit coupling [49] are shown in Figure 2.3, ZnO is a direct band gap ($E_g = 3.4$ eV at Γ point) semiconductor.

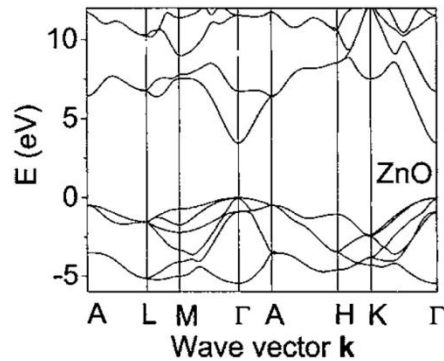


Figure 2.3: The band structures of wurtzite ZnO including spin-orbit interaction [49]

The band structure of ZnO reveals three very closely spaced valence bands (usually referred to as the A, B, and C bands; or heavy-hole, light-hole, and crystal field split-off bands, respectively, resulting from the spin-orbit coupling and crystal field splitting) near the Brillouin zone center (Γ point) [18], as illustrated in Figure 2.4. The symmetry ordering of the crystal field and spin-orbit coupling split levels at the valence band maximum (VBM) (Γ point, $k = 0$) in wurtzite ZnO has been a subject

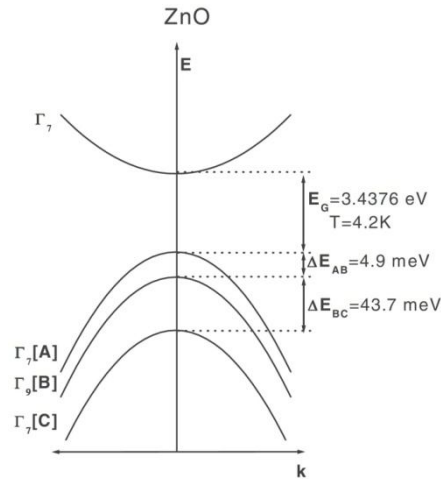


Figure 2.4: Schematic band structure and symmetry of wurtzite ZnO, the three separate valence bands are due to spin-orbit interaction and crystal field splitting [11, 50].

of controversy. Today the ordering of A(Γ_7), B(Γ_9), C(Γ_7) is commonly accepted [51, 52]. Experiment gives the splitting energies between the A, B, and C bands: $E_A - E_B = 4.9 \text{ meV}$, $E_B - E_C = 43.7 \text{ meV}$, and $E_g = 3.437 \text{ eV}$ for A valence band at 4.2 K [11, 50].

The lattice constant changes with temperature, as discussed in last section 2.1. Consequently, the electronic band structure also changes with temperature or pressure. The band gap of wurtzite ZnO (at Γ point, $k = 0$) decrease with increasing temperature, and the dependence is given by the empirical equation (2.1). Where the temperature coefficients are $\alpha = -5.5 \times 10^{-4} \text{ eV/K}$ and $\beta = -900 \text{ K}$ for temperature range up to 300 K [53].

$$E_g(T) = E_g(T = 0) - \frac{\alpha T^2}{T + \beta} \dots\dots\dots (2.1)$$

Band gap engineering is an important tool to develop new optoelectronic devices [54]. The band gap of ZnO can be finely tuned by alloying with MgO or CdO. When the alloying concentration of Magnesium is lower than 43at.%, $\text{Zn}_{(1-x)}\text{Mg}_x\text{O}$ crystal keeps still wurtzite structure, and the band gap $E_g \text{ (eV)} = 3.37 + 2.51x$ can increase up to 4 eV [55]. When the alloying concentration of Cadmium is lower than 69.7at.% [56], $\text{Zn}_{(1-y)}\text{Cd}_y\text{O}$ crystal is also still wurtzite structure, and the band gap $E_g \text{ (eV)} = 3.37 - 4.40y + 5.93y^2$ reduces to 2.9 eV [57]. The lattice constant also shows dependence

on the alloying concentration of Magnesium or Cadmium.

2.3 Optical properties

ZnO is a prospective material for optoelectronics owing to its direct wide band gap ($E_g = 3.37$ eV at 300 K) and effective radiative recombination. The large exciton binding energy of ~ 60 meV, allows an intense near band edge excitonic emission at room and even higher temperatures up to 700 °C [58]. The following topics will concentrate on the radiative recombination of ZnO.

Before reviewing the optical transitions in ZnO, the effective mass approximation (EMA) in semiconductors should be introduced. When the donor Bohr radius is much larger than the crystal lattice constant, a shallow donor atom can be compared with a hydrogen atom; the extra valence electron is only loosely bound to the positive ion. The loosely bound electron can be ionized easily by thermal or electrical excitations. The case for acceptor is similar but in opposite charges. The net effect of the crystal potential on the donor electron inside the crystal is to change the electron mass from the value in free space to the effective mass m^* and also to contribute the factor ϵ (the relative dielectric constant) in the Coulomb potential expression of the donor ion. This approach is known as the effective mass approximation (EMA) [59].

Similar notations are used to denote the bound states of shallow impurities. The energies of these bound states are given by the Rydberg series:

$$E - E_C(0) = -R / N^2 \quad (N = 1, 2, 3, \dots) \quad \dots\dots\dots (2.2)$$

R is the Rydberg constant for the donor electron and is related to the Rydberg constant for the hydrogen atom [$e^4 m_0 / (2\hbar^2)$] by

$$R = \left(\frac{m^*}{m_0}\right) \left(\frac{1}{\epsilon^2}\right) \left(\frac{e^4 m_0}{2\hbar^2}\right) \frac{1}{(4\pi\epsilon_0)^2} \quad \dots\dots\dots (2.3)$$

Being m_0 the free electron mass. The extent of the bound-state electron wave functions in real space is described by a donor Bohr radius, which is in analogy to the Bohr radius in the hydrogen atom [59].

2.3.1 Free exciton transition

In sufficiently pure ZnO semiconductor with good crystallinity the Coulomb interaction between the photoexcited electron in the conduction band and hole in the valence band correlates their motion and binds them together. This bound state of the electron-hole pair is a quasi-particle called exciton which is the fundamental quantum of excitation in a semiconductor [60]. The recombination of an electron and a hole will result in emission of a photon. The energy of the emitted photon is $h\nu = E_g - X$, where E_g is the band gap energy, and X is the exciton binding energy, the value for ZnO is 60 meV at room temperature, which is the highest for any direct band gap semiconductor besides the Cu-halides. The exciton has many features analogous to those of atomic hydrogen. The exciton can be assigned a Bohr radius which is given [61] by equation (2.4)

$$a_B^{exciton} = a_B^H \varepsilon \frac{m_0}{\mu} \dots\dots\dots (2.4)$$

Where a_B^H is the Bohr radius of a hydrogen atom, ε is the relative dielectric constant of the semiconductor, $\mu = \frac{m_e m_h}{m_e + m_h} m_0$ is the reduced mass of the exciton, m_e , m_h is the effective mass of electron and holes in semiconductor, and m_0 is the free electron mass. In ZnO the exciton Bohr radius $a_B^{exciton}$ is approximately 2 nm [6, 11]. This is a length of several lattice constants, and the effective mass approximation is valid in ZnO. The related free exciton recombinations between the electron in conduction band and hole in three valence bands are usually denoted by A-, B- and C- exciton. Availability of high quality ZnO single crystals provides the opportunity to observe free exciton transitions in low temperature photoluminescence (PL), and reflectance measurement. Compared with the B- and C-exciton, the PL technique can much easier probe the A-exciton at $k = 0$ point, because the recombination of the A-exciton in ZnO is strongly allowed. The overall symmetry of an excitonic wavefunction is given by the direct product of the symmetries of the electron and hole wavefunctions [62], for the A-exciton is [50, 63]

$$\Gamma_7 \otimes \Gamma_7 = \Gamma_1 \oplus \Gamma_2 \oplus \Gamma_5 \dots \dots \dots (2.5)$$

Because the Γ_2 exciton is forbidden without an external magnetic field according to the selection rules in wurtzite ZnO [50, 52], two peaks of A-exciton transition could be observed in the PL spectrum of ZnO (labeled as A_T and A_L). A_T has Γ_5 symmetry and transverse character; A_L has Γ_1 symmetry and longitudinal character. The term transverse and longitudinal refer to the orientation of the polarization associated with exciton (electron-hole pair) as it travels through the lattice with wave vector k . The energy position of A_T and A_L in the PL spectrum at 4.2 K is 3.3759 eV and 3.3772 eV, respectively, according to B. K. Meyer's assignment [11]. A_T is the reference for the determination of the bound exciton localization energy. The picture of the free excitonic PL features used throughout this thesis is based on the assignment and explanation by B. K. Meyer et al. [11].

2.3.2 Bound exciton transition

There is a large number of imperfections in the crystal structure of real semiconductors. Free electrons and holes can be scattered or bound to defects and impurities. Excitons will also bind to imperfections in the lattice, losing some of their energy in this process. They become localized around the imperfections and trapped until their recombination. The photons emitted from the recombination of localized excitons have smaller energies than the photons emitted from the recombination of free excitons. The energy difference is called the localization energy E_{loc} of bound excitons, which is determined by the nature of the imperfections [11]. If the thermal energy of the environment is higher than E_{loc} for a specific impurity, excitons are quickly delocalized through phonon interactions. Impurities in ZnO all have their own unique and characteristic localization energy. This result allows the possibilities to qualitatively detect defects and impurities by low temperature photoluminescence. In fact, most of the PL intensity over the UV to visible range is from bound excitonic recombinations [62].

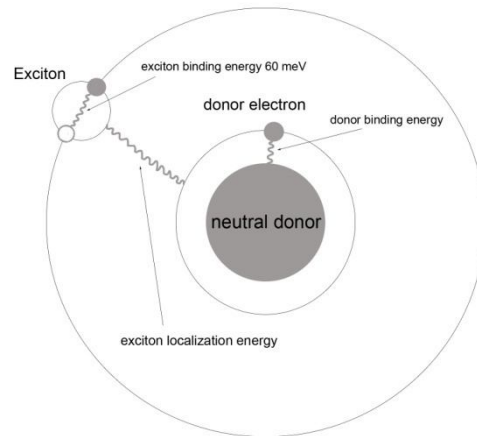


Figure 2.5: Schematic diagram of neutral donor bound exciton complex [64].

ZnO is naturally n-type with the dominant imperfections as donor impurities. Excitons can bind to neutral donors forming a complex called a neutral donor bound exciton, D^0X , as shown in the schematic diagram [64] in Figure 2.5 without

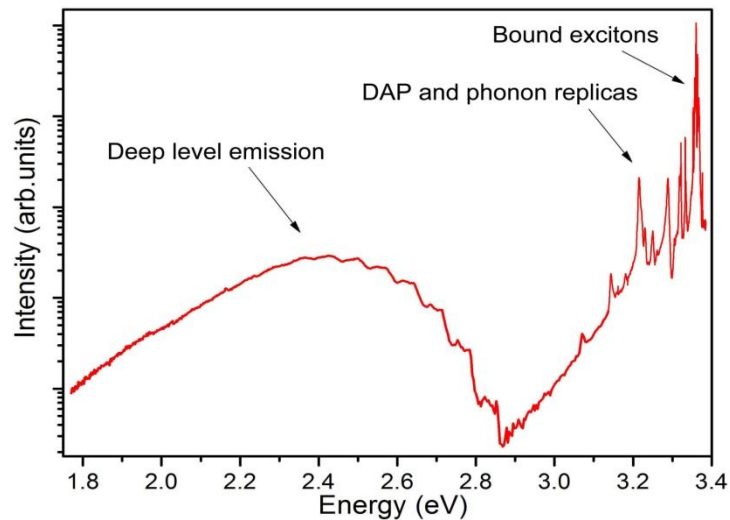


Figure 2.6: A typical PL spectrum of ZnO single crystal measured at 4.2 K.

consideration of proper dimension. For typical neutral donors in ZnO, the exciton localization energies are in the range of 10-30 meV [11]. A typical PL spectrum of bulk ZnO is shown in Figure 2.6, many narrow peaks are seen in the bound excitonic region and usually dominate the PL spectrum of ZnO at low temperatures.

The excitonic peaks have been labeled historically with I_x notation for ZnO, the

numbering convention $I_0 \sim I_{11}$ are listed in Table 2.1. The origin of these peaks is still unclear in most cases. The identified ones are, I_4 : H-related, I_6, I_{6a} : Al-related, I_8 : Ga-related

Table 2.1: Free and bound exciton recombinations and related properties of ZnO [11]

Line	Wavelength (nm)	Energy (eV)	Localisation energy (meV)	Two-electron-satellite separation ($2P_{xy} - 1S$) in (meV)	Donor binding energy (meV)	Chemical identity
A_L^a	367.12	3.3772				
A_T^a	367.26	3.3759				
I_0	367.63	3.3725	3.4			
I_1	367.71	3.3718	4.1			
I_{1a}	368.13	3.3679	8.0			
I_2^b	368.19	3.3674	8.5			
I_3^b	368.29	3.3665	9.4			
I_{3a}	368.34	3.3660	9.9			
I_4	368.69	3.3628	13.1	34.1	46.1	H
I_5	368.86	3.3614	14.5			
I_6	368.92	3.3608	15.1	38.8	51.55	Al
I_{6a}	368.96	3.3604	15.5	40.4	53	
I_7	369.01	3.3600	15.9			
I_8	369.03	3.3598	16.1	42.1	54.6	Ga
I_{8a}	369.08	3.3593	16.6			
I_9	369.37	3.3567	19.2	50.6	63.2	In
I_{10}	369.76	3.3531	22.8	60.2	72.6	
I_{11}	370.28	3.3484	27.5			

^a A_L and A_T are the longitudinal and transversal free A-exciton states. A_T is the reference for the determination of the bound exciton localisation energy

^b I_2 and I_3 are assigned to ionised donor bound exciton recombination lines

and I_{10} :In-related. These are A-excitons bound to donor defects, B-excitons can also be bound to donor defects, with a separation of 4.9 meV between corresponding PL peaks due to the A, B valence band splitting [11].

Ionized donors can also trap excitons and form ionized donor bound excitons, denoted as D^+X . Emissions from I_0 to I_2 were determined to be D^+X recombinations. I_0, I_1, I_2 are the ionized donors belonging to I_{6a}, I_8, I_9 respectively [65]. The localization energy E_{loc} of the D^+X complex is only a few meV.

The appearance of ionized donors at Helium temperatures indicates the existence of acceptors in the sample which are partially compensating the donor concentration. Neutral acceptors can also bind excitons and form A^0X complexes, however, the A^0X emission was absent in the PL spectrum of ZnO. A^0X peaks should appear at lower energies than the D^0X peaks since they are expected to have a higher localization energy with following order [11, 61, 66].

$$E_{Loc}^{D^+X} < E_{Loc}^{D^0X} < E_{Loc}^{A^0X} \dots \dots \dots (2.6)$$

The Hayne's rule relates the donor binding energy E_D (also called donor ionization energy) with the localization energy E_{Loc} of the donor bound exciton by $E_{Loc} = a E_D$ [11, 61], where a is the linear coefficient. More generally E_{Loc} is given by $E_{Loc} = A' + B'E_D$, and A' and B' could be determined from the experiment, such as $A' = -3.8$ meV, $B' = 0.365$ in Ref [11]. The Haynes' rule is also valid for the ionized donor bound exciton D^+X [65].

2.3.3 Two-electron-satellite transition

One unique characteristic of the neutral donor-bound exciton transition D^0X is the Two-Electron-Satellites (TES) transition in the spectral region of 3.32-3.34 eV. These transitions involve radiative recombination of an exciton bound to a neutral donor, leaving the donor in the excited state (2s, 2p states), thereby leading to a transition energy that is less than the D^0X energy by an amount equal to the energy difference between the first excited(2s, 2p) and ground state of the donor. The usual observation of the D^0X peak, of course, occurs when the donor final state is the ground state [18].

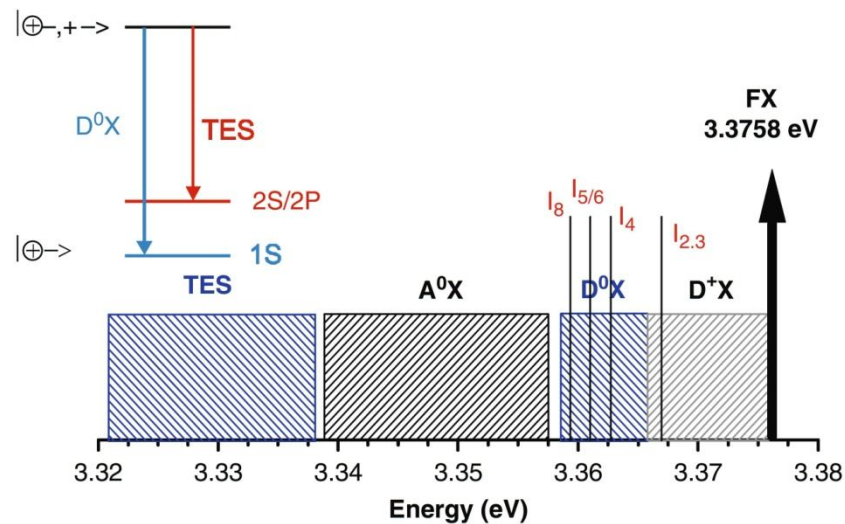


Figure 2.7: A schematic drawing of the energy ranges of various bound excitons with the level scheme for the two-electron-satellites transition [67].

The TES transition together with other bound exciton recombinations are

schematically shown in Figure 2.7 [67], the level scheme for the TES transition is also depicted. The energy distance between the 1s and 2p state, also the energy separation between D^0X and TES recombination, is 3/4 of the donor binding energy (E_D) in the simple hydrogen-like effective-mass-approach (EMA). Therefore, by determining the position of the TES, the related donor binding energy can be estimated.

2.3.4 Donor-acceptor-pair transition

The presence of both donors and acceptors in semiconductors provides a radiative recombination channel known as donor-acceptor-pair (DAP) transition. If the wavefunctions of an electron on a donor and a hole on an acceptor overlap, the electron and the hole can recombine. The energy of the emitted photon resulting from radiative DAP transition is given by equation (2.7) [61]

$$\hbar\omega_{DAP} = E_g - (E_D + E_A) + \frac{e^2}{4\pi\epsilon\epsilon_0 R_{DA}} - m\hbar\omega_{LO} \quad \dots\dots\dots (2.7)$$

The second term is the sum of neutral donor binding energy and neutral acceptor binding energy; the R_{DA} in the Coulomb energy term is the effective distance of many discrete, well-defined distances between donors and acceptors. The zero-phonon DAP band is therefore a broad band, which consists of several discrete lines corresponding to the discrete distances. The last term describes longitudinal optical (LO) phonon replica with a energy of 72 meV, $m = 0, 1, 2 \dots$. With increasing excitation intensity, the number of occupied donor and acceptor centers increases and their average distance necessarily decreases. As a result one can expect a blue-shift of the emission maximum of the DAP recombination due to the Coulomb term in equation (2.7). This is a characteristic feature of DAP transition. In addition, with increasing temperature, a line emerges at higher energies than the DAP peak and takes over in intensity, this is the free-to-bound transition, in which free electrons recombine with the stronger bound acceptor holes [67]. When the donor concentration is much higher than the acceptor concentration, the Coulomb interaction item could also be given by another

form: $aN_D^{1/3}$ [68], where N_D is the donor concentration and the coefficient $a = 3 \times 10^{-5}$ meV·cm; The DAP transition allows a rough estimate of the acceptor binding energy or impurity concentrations.

2.3.5 Phonon assisted recombination

The phonon, which is the quantized crystal lattice vibration, can interact with electron, hole and also exciton. This coupling leads to phonon replicas commonly seen in the PL and the absorption spectrum of many semiconductors. At low temperatures, Fröhlich coupling with the longitudinal optical (LO) phonons is the main origin of the exciton-phonon coupling in polar materials with a large ionic character like ZnO [69, 70]. The exciton-phonon coupling is enhanced when the total binding energy of the exciton complex is comparable to the LO-phonon energy [71]. This can explain why the aluminum-related I_{6a} exciton complex in ZnO generally shows much stronger LO phonon replicas than other exciton complexes [62].

An indicator of the strength of the exciton-phonon coupling is the Huang-Rhys factor S . Using the Frank-Condon approximation, the integrated intensity ratio of the m^{th} LO-phonon replica to the zero-phonon line (ZPL) of an emission peak is given by [72, 73]

$$\frac{I_m}{I_0} = \frac{S^m}{m!} e^{-S} \quad (m = 1, 2, 3, \dots) \quad \dots\dots\dots (2.8)$$

Here, S represents the average number of phonons produced during radiative recombination of a given transition and is directly proportional to the exciton-phonon coupling strength [73]. In addition, Fano resonances [74], a quantum mechanical coupling phenomena that occurs between a discrete level and a continuum of states, often appears in polar semiconductors like ZnO, since the discrete state of exciton LO-phonon coupling sits on top of the continuum states of exciton acoustic-phonon coupling [73, 75]. The intensity of first LO replica of I_{6a} exciton is greatly reduced by the Fano resonance, and is sometimes even much lower than that of the second LO

replica.

2.4 Defects in ZnO

Defects such as vacancies, interstitials, substitutions, dislocations, and stacking faults usually exist in the ZnO lattice. These imperfections in semiconductors are sometimes vital, providing free electrons or holes necessary for functional devices; and are sometimes fatal, compensating the donors or acceptors unintentionally to deteriorate device properties [76]. Common defects in the ZnO lattice will be discussed in this section.

2.4.1 Intrinsic point defects

In thermodynamic equilibrium and in the dilute regime, the concentration c of an point defect or complex in ZnO depends on its formation energy E^f and is given by the expression:

$$c = N_{sites} N_{config} \exp\left(-\frac{E^f}{k_B T}\right) \dots \dots \dots (2.9)$$

Here, N_{sites} is the number of sites in the lattice (per unit volume) where the defect can be incorporated. N_{config} is the number of equivalent configurations in which the defect can be incorporated. k_B is the Boltzmann constant, and T is the temperature in Kelvin. The formation energy of a point defect is not a constant, but depends on the growth or annealing conditions [77], and more practically, the Zn-rich or O-rich environment and the Fermi level. Defects often introduce energy levels in the band gap of the semiconductor; these levels involve transitions between different charge states of the same defect [42]. The relative stability of the various charge states is determined by the formation energy E^f [77, 78],

$$E_{D,q}^f(E_F, \mu) = E_{D,q} - E_H + q(E_V + E_F) + \sum n_i \mu_i \dots \dots \dots (2.10)$$

Where D is the defect, q is the charge state of the defect (e.g., +2, +1, 0, -1, -2), $E_{D,q}$ and E_H are the total energies of the *host+defect* and the *host-only* supercell,

respectively. E_V is the bulk valence band maximum, E_F is the Fermi level referenced to the bulk valence band maximum, n_i is the number of added or removed atoms to create the defect, and μ_i is the chemical potential of the defect species.

The value of the Fermi level where charge states q and q' are equal in formation energy defines the transition level [78] $\varepsilon(q/q')$:

$$\varepsilon(q/q') = \frac{E_{D,q'} - E_{D,q}}{q - q'} - E_V \quad \dots\dots\dots (2.11)$$

The formation energies as a function of Fermi level position for native defects in ZnO are shown in Figure 2.8. Although locating at the same Fermi level and having the same charge, the same defect shows quite different formation energies in Zn-rich and O-rich conditions, because of the different chemical potentials of the defect species at different conditions. Besides the formation energy, the migration barrier of point defects is also important, which determines the mobility of the defect species.

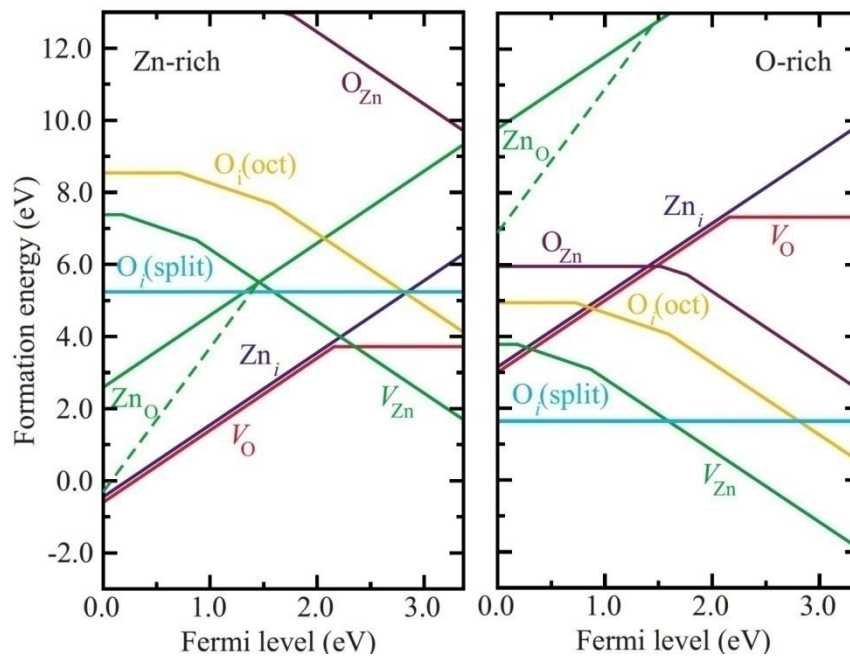


Figure 2.8: Formation energies as a function of Fermi-level position for native defects in ZnO. Results for both Zn-rich and O-rich conditions are shown [42].

Oxygen vacancy (V_o) can be easily created by annealing in oxygen-deficient environment. Experiments show that the oxygen vacancy locates mainly near the

surface of the ZnO crystal within 1 μm . The oxygen vacancy is a deep and negative- U donor, where the $2+$ charge state is more thermodynamically stable [79]. Oxygen vacancy was frequently believed to be the origin of the green luminescence band centered around 2.4 eV [80], but this assignment seems to be not correct by recent investigations: electron irradiation, which produces O vacancies and other defects, leads to a reduction in green luminescence and an increase in PL bands near 600 and 700 nm [81, 82]. Also, the configuration coordinate diagram calculated for the O vacancy does not show any transitions consistent with the green emission [83].

Zinc vacancy (V_{Zn}) is a deep acceptor with energy level $E(0/-1) = 0.18$ eV and $E(-1/-2) = 0.87$ eV. These levels are too deep to act as shallow acceptors [42, 84]. In contrast to V_{O} , V_{Zn} is suggested to account for the green luminescence [79].

Interstitial zinc (Zn_i) is a shallow donor. It has a high formation energy in n-type ZnO and is a fast diffuser with migration barriers as low as 0.57 eV. Therefore, even if it is formed, the interstitial zinc is not stable at room temperature due to the fast diffusion [42, 85].

2.4.2 Extrinsic point defects

Hydrogen is unintentionally incorporated into ZnO and exists in three different forms: interstitial hydrogen, substitutional hydrogen and hydrogen molecules. Interstitial hydrogen (H_i) [86] and substitutional hydrogen at the oxygen vacancy (H_{O}) are shallow donors [87] and can induce n-type conductivity in ZnO [88, 89]. The electrically inactive hydrogen molecule (H_2) also exists in ZnO [90]. In addition, substitutional acceptors could be passivated by the formation of acceptor-hydrogen complexes, like $N_{\text{O}}\text{-H}$ [91], $\text{Li}_{\text{Zn}}\text{-H}$ [92].

Group-I metal impurities (Li, Na, K) are detected in hydrothermally grown ZnO crystals in noticeable concentrations. Li and Na substitute the sites of Zn and act as acceptors. However, these acceptors are compensated by the simultaneously introduced donors: Li and Na on the interstitial sites [93, 94]. There were a few reports of p-type ZnO samples doped with Li or Na [95], however, further

confirmation is missing. Cu is also a common trace impurity in ZnO crystals. Cu forms a deep acceptor level and is a candidate for the green luminescence band in ZnO [96, 97].

Group-III impurities (Al, Ga, In) always exist in ZnO crystals independent of the growth methods. Al, Ga and In atoms on Zn sites are shallow donors. These donors are the chemical origin of I_6 , I_8 and I_9 bound exciton recombinations in the PL spectrum of ZnO [11]. They are also an important source for the natural n-type conductivity in ZnO.

Group-V impurities (N, P, As, Sb) were supposed to be the prospective candidates for the p-type doping of ZnO. Among them nitrogen has particularly drawn the widest attentions for two reasons: i) nitrogen has a similar ionic radius as the oxygen atom, and ii) nitrogen gases are convenient dopants. But recent investigations from both theory [98] and experiments [12] show that nitrogen is actually a deep acceptor with ionization energy of 1.3 eV in ZnO. First-principles calculations predict that P, As and Sb are also deep acceptors [99, 100]. In spite of this, there are reports of shallow acceptor levels induced by As [101] and Sb [102].

2.4.3 Extended defects

Dislocations frequently exist in ZnO crystals. The density of dislocations is determined by etching the surface and counting the etch pits. Hetero-epitaxial layers typically contain threading dislocation densities of 10^9 cm^{-2} , due to the lattice mismatch near the interface [79]. The typical PL lines Y_0 , Y_1 and Y_2 at 3.333 eV, 3.336 eV and 3.346 eV, respectively, all originate from structural defects (most probably dislocations) [103].

Bulk ZnO samples, epitaxially grown ZnO layers, and ZnO nanostructures frequently exhibit a characteristic emission band at 3.314 eV, which is ascribed to (e , A^0) transition of a conduction band electron to an acceptor. The acceptor state is caused by stacking faults and has an ionization energy of 130 meV [68].

The atoms in grain boundaries have different local environments from those in

ideal bulk lattice. Defects at grain boundaries play an important role in ZnO varistors [104]. First principles calculations reveal that, the deep acceptor N_O in normal ZnO lattice turn to be shallow acceptor in the grain boundaries region, which makes p-type grain boundary embedded between n-type ZnO grains [105, 106].

Absorbed species and dangling bonds may result in surface state levels in the band gap of ZnO. An exciton bound to a surface defect was proposed to be the origin for the commonly observed emission at 3.367 eV in ZnO structures. Surface exciton emissions are easier to appear in thin films and nanostructured samples, and will be strongly affected by the detailed nanostructure morphology [107-109].

Chapter 3

Growth methods and experimental techniques

In this chapter, the methods of growing ZnO single crystals and thin films will be reviewed; the processing and characterization tools of samples will be introduced and explained.

3.1 Growth methods of ZnO single crystals

If a comparison between GaN and ZnO is made, very often two advantages of ZnO will be mentioned. One is the huge variety of different growth techniques available to fabricate ZnO; the other is the possibility to grow thin films homoepitaxially on ZnO substrates, which eliminates the lattice-mismatch on foreign substrates. High quality single ZnO crystals are important not just for basic investigations but also for device applications.

3.1.1 Hydrothermal growth

In the hydrothermal method (also called solvothermal method), water is used as a polar solvent and the ZnO solute (nutrient) are placed in an autoclave which can simply be described as a pressurized vessel designed to heat aqueous solutions above their boiling point. Generally, about 70 - 90% of the autoclave volume can be filled [7, 110]. Figure 3.1 shows the schematic illustration of a hydrothermal growth system. The nutrient which is composed of sintered ZnO pellets is dissolved in the hotter zone which is located at the bottom section of the autoclave (with temperature T_1 in Figure 3.1). The aqueous solution saturated in the lower part is transported by convective motion of the solution to the upper zone housing the ZnO seed crystals

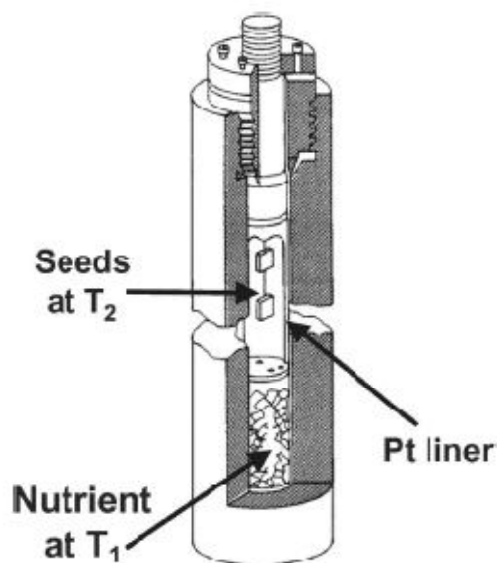


Figure 3.1: Schematic illustration of autoclave for hydrothermal growth method [111].

suspended by Pt wires. The upper zone is maintained at a lower temperature (T_2 in Figure 3.1) to provide supersaturation. The temperature difference, ΔT , between the growth zone and the dissolution zone should be smaller than 20 K. The control of ΔT within 3 K is necessary to suppress the tendency towards spontaneous nucleation and flawed growth of ZnO [111]. The seeds and the particular nutrients are placed into a Pt crucible, which is also frequently referred to as the liner [112]. The volume between the autoclave and the liner is filled with a suitable amount of distilled water for pressure balancing to prevent the liner from serious deformation.

The hydrothermal growth of ZnO is performed in a temperature range from 300 to 430 °C at a pressure from 70 to 250 MPa. Under such conditions, water can reach a supercritical state. The enhanced acidity and diffusivity of water above the supercritical point favors ionic process such as dissolution of ZnO. However, the solubility of ZnO in supercritical water remains insufficient for hydrothermal growth, which makes the use of mineralizers necessary. Mineralizers increase the solubility of ZnO by forming metastable compounds, which later decompose at the growing crystals face. LiOH, NaOH, KOH, Li_2CO_3 and H_2O_2 have been employed as mineralizers. And the best solvent for ZnO is an appropriate mixture of KOH and LiOH [113].

An important feature of the hydrothermal method is that more than one seed crystal can be placed into the autoclave and more than one crystal can be grown at a time. Hydrothermal growth is a bulk growth method for ZnO, and freestanding wafers up to 3 inch in diameter (Tokyo Denpa) have been produced [110].

3.1.2 Melt growth

The melt growth of ZnO presents two unique challenges: i) the dissociation of ZnO into Zn and O₂ at the melting point which is as high as 1975 °C; ii) the high equilibrium total vapor pressure (1.06 bar) above ZnO at the melting point. Therefore, to maintain the ZnO melt stable, the total pressure of oxygen-containing atmosphere in the growth chamber must be considerably larger than 1.06 bar. However, the prevention of corrosion of the crucible containing molten ZnO under highly oxidizing conditions is a serious challenge [111]. Two different modification of the Bridgman technique were proposed and implemented recently: 1) pressurized melt growth with water-cooled crucible [9], and 2) utilizing iridium crucible and CO₂ atmosphere [8].

1) *Pressurized Melt Growth*: The pressurized melt growth process developed by Cermet Inc employs a skull melting of ZnO and a positioning system typical for the Bridgman technique. The vessel is a high pressure melting apparatus wherein the melt is contained in a water-cooled crucible under oxygen overpressure (see Figure 3.2a for a simplified schematic diagram). ZnO powder is chosen as starting material and melting is accomplished by radio frequency (RF) induction heating at about 1900 °C. Once the melt state is attained, the crucible is slowly lowered down from the heated zone to allow controlled crystallization of the melt, meanwhile, the hot crucible was cooled by water to reduce the corrosion. In this way, ZnO boules up to 50 mm in diameter have been achieved [111].

2) *Bridgman Growth with Iridium Crucible*: Although it was initially believed that there is no suitable material which can withstand elevated temperatures near 2000 °C

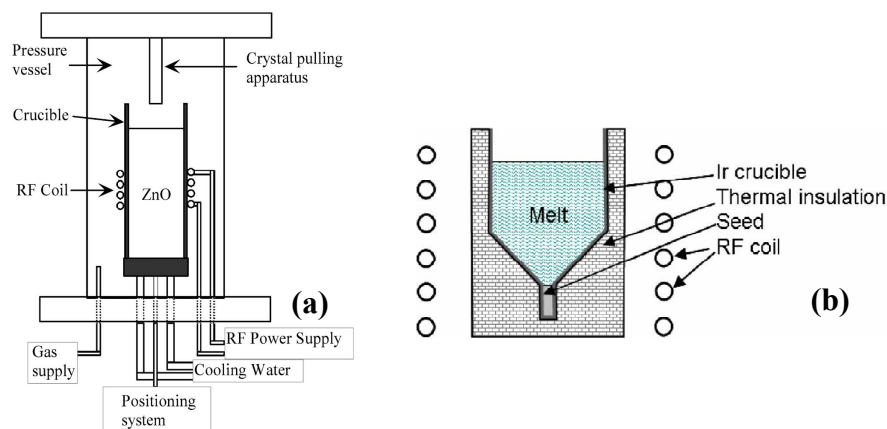


Figure 3.2: (a) schematic system of the pressurized melt growth and (b) schematic system of Bridgman growth with iridium crucible.

in oxygen-containing atmosphere, Schultz et al. [114] have demonstrated that the Iridium crucible has a sufficiently low oxidation rate when exposed to elevated oxygen pressures at 1975 °C (melting point of ZnO). However, the oxidation rate of Ir is serious in the range of 1000 – 1200 °C and the Ir crucible will be destroyed during heating. Oxidation rate of iridium exposed to elevated oxygen partial pressures is at a maximum at around 1000 °C. This problem was solved by using the gas CO₂. At temperatures around 1000 °C the pressure of oxygen resulting from CO₂ dissociation is sufficiently low to avoid Ir oxidation/deterioration, but high enough to keep the ZnO melt stable at 1975 °C [115].

The growth setup is schematically illustrated in Figure 3.2b. The growth chamber is evacuated and then filled with either a mixture of 6 vol% CO₂ in Ar or with pure CO₂ to a pressure of 17.5 bar. The crucible with ZnO powder is heated up to 1975 °C. At the melting point of ZnO, the total pressure inside the growth chamber reaches approximately 19 bars. The electrical power is switched off, the crucible is cooled down slowly and ZnO melt begins to crystallize. Single crystal ZnO boules of 33 mm in diameter and 40 mm in length have been successfully grown by this technique, and 33 mm diameter wafers were cut from such boules [111, 116].

The melt growth offers multiple crystal orientations (*c*-, *a*-, and *m*-plane) made by three-dimensional nature of growth, and *in-situ* doping control of semi-insulating or heavily n-type conductivity [18].

3.1.3 Seeded chemical vapor transport growth

In the method of seeded chemical vapor transport (SCVT), chemical reactions and crystal growth take place in a closed horizontal glass ampoule [117]. Pure ZnO powder used as the nutrient is placed at the hot end (hot zone) of the tube that is kept at about 1150 °C, after dissociation reactions the material is transported to the cooler end of the tube, which is maintained at about 1100 °C, by using H₂ as a carrier gas. The reaction in the hot zone is $\text{ZnO(s)} + \text{H}_2\text{(g)} \rightarrow \text{Zn(g)} + \text{H}_2\text{O(g)}$ (if small amount of graphite powders were mixed into the nutrient, corresponding reaction will be $\text{ZnO(s)} + \text{C(s)} \rightarrow \text{Zn(g)} + \text{CO(g)}$ [118]). At the cooler end, ZnO is formed by the reverse reaction, assisted by a single-crystal seed, as shown in Figure 3.3. To maintain the proper stoichiometry, a small amount of water vapor is added. 2 inch diameter ZnO crystal with 1 cm in thickness has been achieved after 150-175 hours' growth [111]. Seeded chemical vapor transport using chlorine and carbon as transporting agents has also been used to achieve ZnO crystal growth at moderate temperatures of 950 – 1000 °C [119]. The unique feature of SCVT method is the high purity of as-grown single crystals at the expense of low growth rate and output.

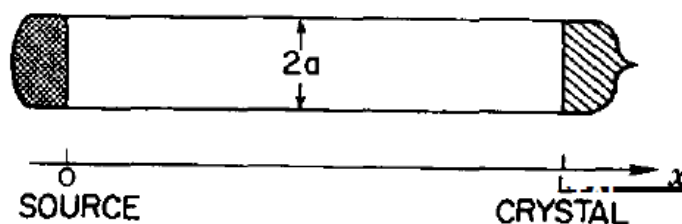


Figure 3.3: Typical horizontal cylindrical ampoule for seeded chemical vapor transport growth

3.1.4 Open-system physical vapor transport growth

Hydrothermal growth is presently believed to be the only approach which is capable of providing commercially mass production of ZnO crystals; however, the hydrothermal crystals inevitably incorporate alkali metals (K and Li) from aqueous

mineralizers [112] and small amounts of metallic impurities from the solution.

Melt growth seems to be a promising method to compete with hydrothermal growth. However, it is still considered to be at the developmental state, and the near-term goal is to avoid the grain boundaries and thermal stress, which result from the considerable temperature gradient near the crucible wall. Pressured melt growth also suffers from high concentrations of residual impurities.

Although seeded chemical vapor transport (SCVT) method provides the lowest concentration of residual impurities among the three approaches, SCVD has a very low growth rate. In addition, SCVT is usually performed in a sealed glass ampoule, the pressure and vapor ingredients inside the ampoule could vary from their starting point after several hours' reaction and growth. These varieties definitely affect the quality of as-grown ZnO crystals. In addition, thermal stress will appear during the cooling of the ampoule wall [120].

To grow good quality ZnO single crystals, a low-cost and open-system vapor transport growth under atmospheric pressure is adopted in this thesis [121-125]. Briefly, ZnO pellets were reduced to Zn vapor at elevated temperature (T_1 varied from 800 to 1300 °C) by the incoming H_2 gas. N_2 was employed as carrier gas to transport the Zn vapor to the growth zone. O_2 was introduced into the furnace chamber from the opposite direction to oxidize the zinc vapor in the region of higher temperatures (T_2 could be varied from 1000 to 1400 °C). ZnO nucleates spontaneously on the zinc oxide cone and grows to needle-shaped single crystals [124]. The growth duration was chosen from 1 h to 40 h. More detailed growth procedures will be described and discussed in chapter 4.

3.2 Growth methods of ZnO thin films

3.2.1 Review of main approaches for growing ZnO films

Pulsed Laser Deposition (PLD): PLD [126] uses high energy pulsed laser radiation to vaporize by photon absorption the surface of the ZnO target material to be

deposited as a thin film on a substrate. A schematic PLD system for the growth of thin films is shown in Figure 3.4. Intense laser pulses of nanosecond duration range are focused in a vacuum chamber onto a target surface where they are absorbed. Above a

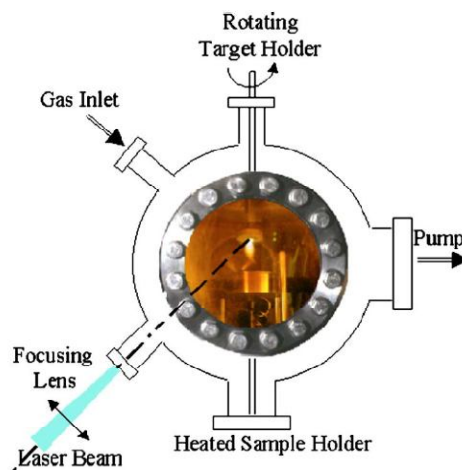


Figure 3.4: Schematic description of a PLD experimental set-up

threshold power density depending upon the target material (generally around 50 mW/cm^2), significant material removal from the target occurs in the form of an ejected luminous plume whose species are collected on a substrate. The substrate can be heated to certain temperature to ensure the growth of crystalline material. PLD allows the growth of thin films in oxygen pressure (from 10^{-6} to 1 mbar) with the same composition as that of the target. This makes PLD particularly well suited for growing thin films of oxides, such as ZnO. Crystalline ZnO films can be obtained by PLD at temperature as low as $200 \text{ }^\circ\text{C}$ [127]. The high kinetic energy of the species (10-100 eV) emitted from the target enables an enhanced surface mobility of these species on the growing films [128].

Metalorganic Chemical Vapor Deposition (MOCVD): In MOCVD [126] ultra-pure gases are injected into a reactor and finely controlled to deposit a very thin layer of atoms onto a prepared substrate. The well-controlled film growth is based on the chemical reactions of various gaseous, liquid and solid precursors. With consideration of the cost, safety, purity, availability, growth rate and the key problem of premature reactions between the Zn metalorganic compounds and the oxidants, DEZn,

$(C_2H_5)_2Zn$, is the most used Zn precursor in the MOCVD growth of ZnO epitaxial films, and O_2 , CO_2 , N_2O or t-BuOH as oxygen sources are mostly used with a separate injector geometry. Since MOCVD growth has the thermodynamic equilibrium characteristic, high quality ZnO films on various substrates have been successfully obtained [126]. Finally, hydrogen and carbon incorporation poses a substantial problem during the MOCVD growth of ZnO at low temperature [51].

Molecular Beam Epitaxy (MBE): MBE is an extremely versatile vacuum deposition technique for preparing thin semiconductor layer. For materials containing O, as in the case of ZnO, the gas species are provided in their reactive state, by an RF plasma.

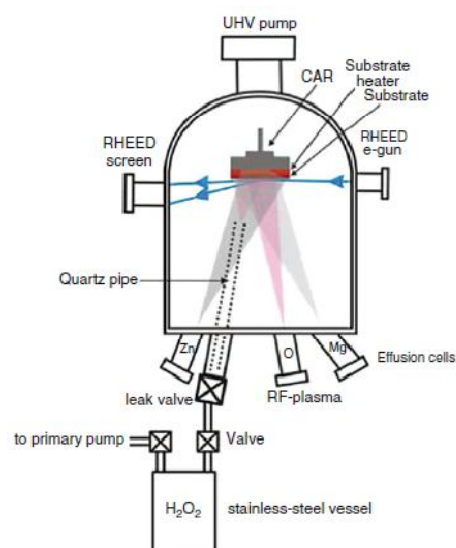


Figure 3.5: Schematic diagram of an RF assisted MBE system

The main advantage of MBE is its precise control over the growth parameters and *in situ* diagnostic capabilities. MBE growth is carried out under conditions that are governed by the kinetics, rather than by mass transfer [129]. Thin films are formed on a heated substrate through various reactions between thermal molecular beams (atomic beams in the case of RF activated oxygen) of the constituent elements, which participated in the form of surface species. The typical growth rate of slightly more than one monolayer per second, is sufficiently low to allow migration of the impinging species on the surface (in the case of ZnO, one monolayer constitutes

a O/Zn bilayer) [18]. For ZnO films deposition by MBE, Zn metal and O₂ are usually used as the source materials. Because of the high molecular bonding energy of O₂ [130], sources of reactive radical oxygen species are needed. Typically an MBE deposition system for ZnO growth consists of a conventional MBE chamber, but with added equipment, such as a RF source. A schematic diagram for a typical RF assisted MBE system is shown in Figure 3.5.

RF Magnetron Sputtering: The schematic diagram of a typical RF magnetron sputtering system [18] is shown in Figure 3.6. In magnetron sputtering, the growth is usually carried out in an ambient of O₂/Ar + O₂, with ratios ranging from 0 to 1 at a

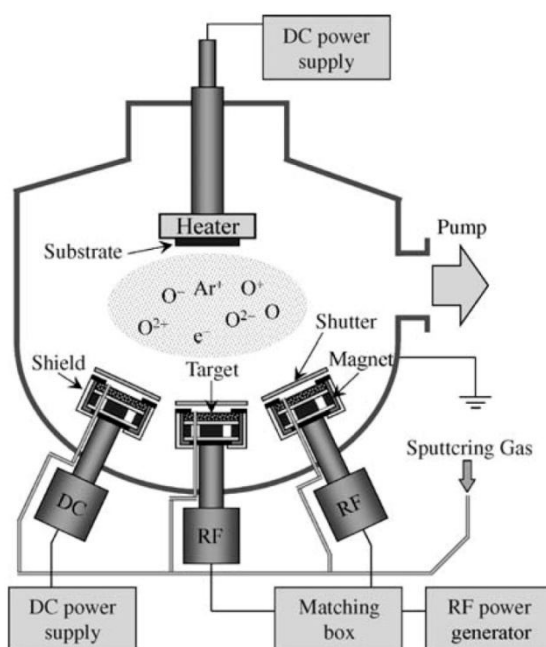


Figure 3.6: Schematic illustration of an RF magnetron sputtering system with DC power supply

pressure of $10^{-3} - 10^{-2}$ Torr. O₂ serves as the reactive gas and Ar acts as the sputtering enhancement gas. ZnO can also be grown by DC sputtering from a Zn target in an Ar + O₂ gas mixture. The RF power applied to the plasma is tuned to regulate the sputtering yield rate from the ZnO target. The target is pre-sputtered for 5 – 15 min before the actual deposition begins to remove any contamination on the target surface, this makes the system stable, and allows optimized deposition conditions.

3.2.2 Vapor phase transport method for growing ZnO films

In order to integrate future ZnO devices with Silicon IC technology, the growth of ZnO films on Si substrates has attracted a great deal of attentions [131-133]. In this thesis we grow ZnO films on silicon substrate by a simple and low cost vapor transport method.

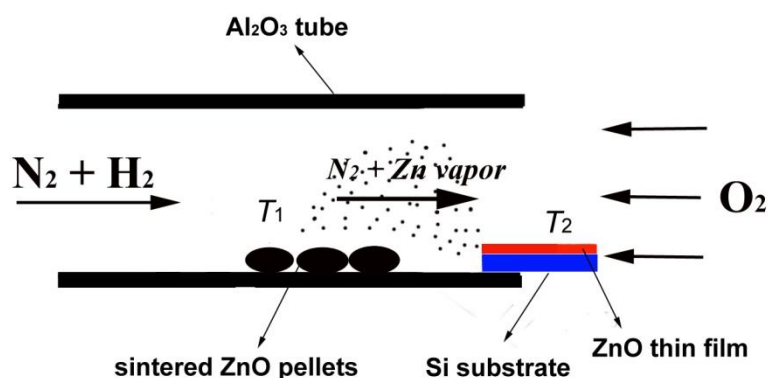


Figure 3.7: Schematic illustration of vapor transport method for growing ZnO films on Si

As shown in Figure 3.7, the main setup is a horizontal Al_2O_3 ceramic tube in a furnace. Zn vapor was produced from ZnO pellets by reduction in H_2 gas at temperature T_1 . Si substrate, which was etched by 10 vol% HF solution, was placed at the end of Al_2O_3 ceramic tube with higher temperature T_2 . N_2 was employed as carrier gas to transport the zinc vapor to the growth region. O_2 was introduced into the furnace chamber to oxidize the zinc vapor on the surface of Si substrate. ZnO layer was subsequently formed on the surface of the Si substrate. Besides the sintered ZnO pellets, ZnO powers and Zn powders are also used to provide the source of zinc vapor. More details of the ZnO films growth on Si substrates will be given in chapter 5.

3.3 Processing techniques of ZnO samples

The needle-like ZnO single crystals and ZnO thin films samples were carefully collected from the growth tube. In addition, both as-grown ZnO samples and commercially bought ZnO crystals are subjected to several processing procedures for various characterizations and investigations.

Etching of ZnO crystals was performed at room temperature in orthophosphoric acid, with an etching speed of about $0.6 \mu\text{m}/\text{min}$.

The thin film samples on Si substrate were cut by a diamond knife and the cross section after cutting was mechanically polished to ensure the characterization of scanning electrons microscopy (SEM).

The annealing of ZnO samples was performed in a furnace with temperatures from $50 \text{ }^\circ\text{C}$ to $1000 \text{ }^\circ\text{C}$ under flowing Argon atmosphere. Some samples were annealed in sealed glass ampoules, which were filled with gases (such as O_2 , H_2 , N_2) of 0.5 bar after evacuation of air, and the hot ampoules were finally quenched to room temperature in water in seconds.

The DC remote plasma treatment of ZnO crystal was performed in a setup shown in Figure 3.8 [134]. Single N_2 gas or N_2+O_2 mixture with 1:2 volume ratios was

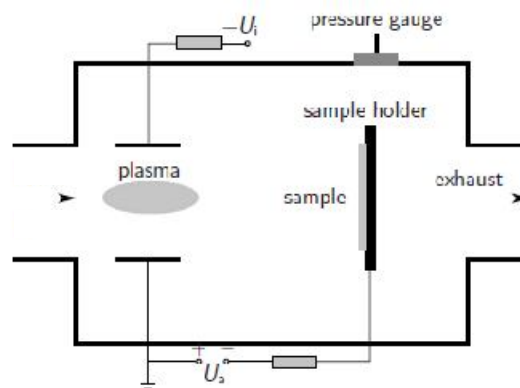


Figure 3.8: Sketch of the remote DC plasma setup [134]

introduced into the chamber with a pressure of 0.4 mbar and temperature of $300 \text{ }^\circ\text{C}$. The bias voltage is set to 510 V and the acceleration voltage is set to 200 V. When the gas passes through the space between two plate electrodes, the gas molecules are

ionized and the DC plasma forms with a pink color. The ion hit to the sample surface with the help of acceleration field.

The radio-frequency (RF) plasma treatment was carried out by 2 different setups and gas sources are N_2 (home-built RF plasma setup) and N_2O (Roth&Rau microsystem, AK800 Inline PECVD), respectively. The sketch of the two different RF plasma setup are shown in Figure 3.9.

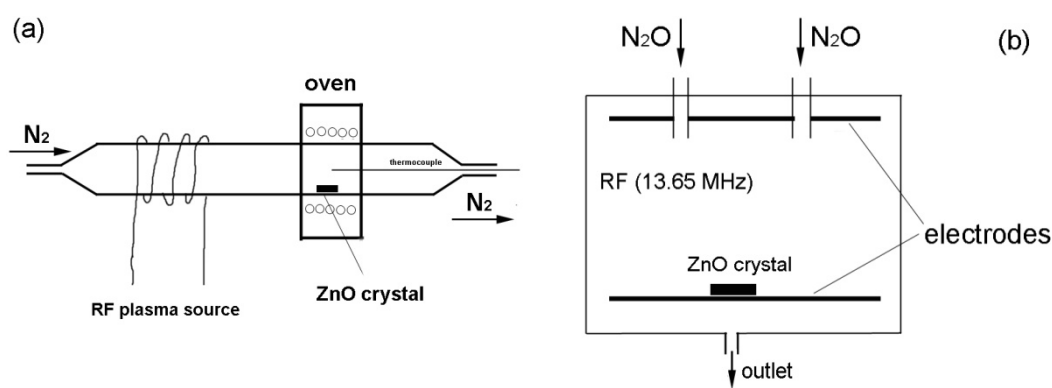


Figure 3.9: Sketch diagram of two different RF plasma setup: a) N_2 plasma and b) N_2O plasma

3.4 Characterization techniques of ZnO single crystals/thin films

3.4.1 Photoluminescence

Photoluminescence (PL) spectroscopy is a direct probe of a semiconductor's electronic band structure. It can be used to qualitatively address materials purity and structural quality by studying the PL features intrinsic to the material, such as the band-to-band transition and free excitonic features. Impurities or structural defects could also be detected by PL. The non-destructive nature and easy parameter control by laser excitation make PL spectroscopy a powerful technique for semiconductor characterization. The experimental set up used for the PL spectroscopy measurements is shown in Figure 3.10 [62]. ZnO samples were placed inside liquid Helium in an Oxford cryostat, which can keep the temperature of sample constant between 3.5 K and 300 K, with the help of a PID temperature controller. A typical He-Cd laser,

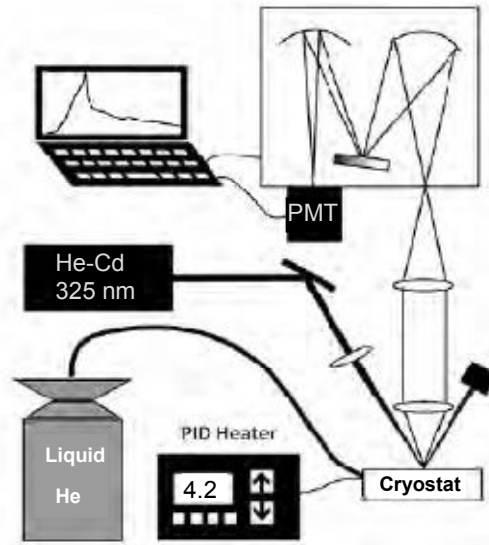


Figure 3.10: Typical photoluminescence setup using He-Cd laser 325 nm excitation

which is operating at 325 nm (3.815 eV) with 3 mW power, provided above band gap excitation of the samples. Light emitted in the direction normal to the sample surface was focused by a lens with high UV transmission and was dispersed by a $f = 1$ m. single grating monochromator (SPEX, 1740X) equipped with a 1200 rules/mm UV-blazed diffraction grating and detected by a Peltier-cooled photomultiplier (PMT) (Hamamatsu, R943-02). PL signals were processed by lock-in technique. A stepper motor attached to the grating sinebar lead screw gave a minimum spectral step size of 0.00415 nm although 0.01 nm was usually sufficient for the sharpest bulk ZnO PL spectrum. Spectrometer slit width were in the range of 10 -200 μ m. The PL spectra of ZnO samples were typically recorded in four separate spectral ranges (366 ~ 370 nm, 370 ~ 375 nm, 375 ~ 395 nm and 395 ~ 700 nm) with different slit widths for signal collecting. The different spectra were normalized to one spectrum.

With consideration of the actual photomultiplier response and different absorption coefficient of optical lens and filter at different wavelength from UV to visible, the relative intensity of recorded spectrum could be somewhat varied. The measurement system was calibrated with reference to the well-known spectrum of blackbody radiation [135]. In addition, wavelength calibration of the spectrometer is also performed with reference to the known peaks of reference samples.

The peak position in the PL spectra may change from sample to sample due to the strain, surface modification or small systematic errors in the experiment. A single PL spectrum is usually not sufficient to unambiguously identify the origin of specific peaks [62]. Temperature dependent and excitation power dependent PL spectra can provide additional supports for peak identification.

The temperature dependence of the intensity can be used to establish the activation energy for bound exciton transitions if the emission intensities (absolute intensity or integrated intensity of one peak) can be determined. The PL intensity can be modeled by the fit to the following equation:

$$I(T) = \frac{I(0)}{1 + A \exp\left(\frac{-E_a}{k_B T}\right)} \dots\dots\dots (3.1)$$

where $I(0)$ is the PL intensity at $T = 0$ K, A is related to the efficiency of the decay channel, k_B is the Boltzmann constant, and the energy terms E_a is the activation energy of the decay channel. For bound exciton transition the activation energy corresponds to the localization energy of the exciton [73].

The excitation power (laser intensity) can be very easily varied by simply placing a neutral filter with a known transmission curve in front of the laser. The excitation power can be precisely varied over three orders of magnitude from 0.1 mW to 50 mW. The excitation power dependence of the PL emission can be described in general by a power law.

$$I \propto P^k \dots\dots\dots (3.2)$$

Where I is the emission intensity of observed peak, P is the laser excitation power and k is a coefficient which depends on the nature of the recombination process. For free and bound excitons, k is shown to be $1 < k < 2$; and for free-to bound and DAP transitions, k is shown to be $k < 1$ [136, 137]. In addition, a characteristic of the DAP transition is the blue shift of peak maximum with increasing excitation power [59].

3.4.2 X-ray diffraction analysis

The structure and crystal quality of ZnO semiconductor can be determined by X-ray diffraction (XRD), XRD is a non-contact and non-destructive tool for characterization. It is based on the Braggs law: $n\lambda = 2d\sin\theta$, where n is the order of refraction, λ is the wavelength of the incident X-rays (typically with a Cu $K\alpha$ line at $\lambda = 0.15405$ nm), d is the distance between atomic planes in the lattice and θ is the angle of incidence. The diffraction pattern (the intensity of diffracted x-ray beam vs. 2θ angle) can be used as fingerprint to determine the crystal structure of the material, The angular position of the peaks in diffraction pattern give an indication of the lattice parameters; while the width (rocking curve) of the peaks give an indication of the uniformity of the crystal, where the width of the peak is roughly proportional to the defect density. An URD 6 (Seifert-FPM) diffractometer with a Cu $K\alpha$ x-ray tube and a step size of 0.01° was used for 2θ scan between 20° and 80° at room temperature.

3.4.3 SEM, EBSD and Cathodoluminescence

Scanning electron microscopy (SEM) is a non-contact, non-destructive technique for imaging the surface topography. The mode “secondary electron imaging” is mainly used to examine the surface morphology with typical resolutions in the order of 5 -10 nm. The mode “backscatter electron imaging” is used to qualitatively analyze the chemical element compositions near the sample surface by employing energy dispersive X-ray spectroscopy (EDX). The surface morphologies of the needle-shaped ZnO crystals, thin films and film cross-section were examined by a FEG-SEM, Carl Zeiss Ultra 55 at 10 KV acceleration voltages. The elemental analysis of local areas on the sample surface was conducted in the same SEM which was equipped with EDX detector (DBruker axs, XFlash detector 4010).

When an electron beam is incident on a tilted crystalline sample, electron backscatter diffraction (EBSD) patterns can be formed on a suitably placed phosphor screen. The diffraction pattern consists of a set of Kikuchi bands which are

characteristic of the sample crystal structure and orientation [138]. The position of the Kikuchi bands can be analyzed automatically. They allow to calculate the crystal orientation of the sample region that formed the pattern [139]. The crystallographic orientations of the ZnO needle-shaped crystals were determined by EBSD using an HKL Nordlys EBSD detector and Channel5 software, and conducted with the sample tilted at a angle of 70° [124].

Cathodoluminescence (CL) is the emission of photons of characteristic wavelengths from a material that is under high energy electron bombardment. The electron beam is produced by the accelerating field in the SEM. With the addition of a spectrometer it is possible to record a scan of the CL intensity vs. wavelength of a semiconductor. The CL of ZnO samples was also measured in the same SEM equipped with CL accessory under 10 KV accelerating voltages, and the CL signal is dispersed by the monochromator equipped with 500 rules/mm grating and detected by CCD camera with step size of 0.4 nm at room temperature.

3.4.4 Electrical conductivity measurement

Electrical characterizations of the ZnO samples were carried out by Current-Voltage curves (I-V) and thermoelectrical measurement. I-V curves were employed to measure the resistivity of shaped needle-crystal samples at room temperature. Thermoelectrical measurements were also used to determine the carrier type. The Ohmic contacts in these measurements were made of In-Ga alloy.

Chapter 4

Vapor phase growth of ZnO single crystals

A low-cost and open-system vapor phase method was used to obtain high quality ZnO single crystals with low defect concentrations. The technique has the flexibility of doping during the crystal growth.

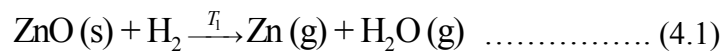
4.1 Introduction

The traditional growth methods (hydrothermal, melt growth, and seeded chemical vapor transport), have the drawbacks of high complexity, relatively high cost and incorporation of Alkali metals. We used instead an open-system vapor phase method [121-123, 125] to grow needle-shaped ZnO single crystals. The oxidation of Zn vapor was performed in a heated open growth tube. In this work, three different growth tubes were employed: i) Al₂O₃ tube + ZnO cone, ii) ZnO tube, and iii) Al₂O₃ tube. In the first type of growth tube, the structure of ZnO cone can provide larger areas for nucleation. This is beneficial to produce more ZnO crystals in one growth. However, the ZnO ceramics can be destroyed by reacting with H₂ transport gas after long-term growth. As a result, the growth with Al₂O₃ tube was proposed with a layer of polycrystalline ZnO coated on the Al₂O₃ tube tip prior to the growth of ZnO single crystals. Furthermore, the dominant factors, including growth temperatures and gas flow rates, in the crystal growth were also investigated in this chapter.

4.2 Growth principles and growth setup

The growth principles of ZnO single crystals by our open-system vapor transport method are described in Figure 4.1. The growth tube consists of a Al₂O₃ ceramic (AdValue Technology, inner diameter of 38.5 mm and length of 380 mm) and a cone made of ZnO ceramics (diameter of 44.5 – 80 mm and length of 80 mm). The ZnO

ceramics was made of ZnO powders (Pharma 8, Grillo Zinkoxid GmbH) by isostatically pressing and 1200 °C sintering. The source materials for the ZnO pellets used during growth are made of the same ZnO powders by isostatically pressing and sintering at 800 °C. The main contaminants of the Al₂O₃ tube material and the ZnO powder are given by the vendors and listed in Table 4.1. The ZnO pellets placed in the horizontal tube were reduced to zinc vapor at elevated temperatures (T₁ varied from 800 to 1300 °C) by the incoming H₂ gas (see equation (4.1)),



N₂ was employed as carrier gas to transport the zinc vapor to the growth zone. O₂ was introduced into the furnace chamber from the opposite direction to oxidize the

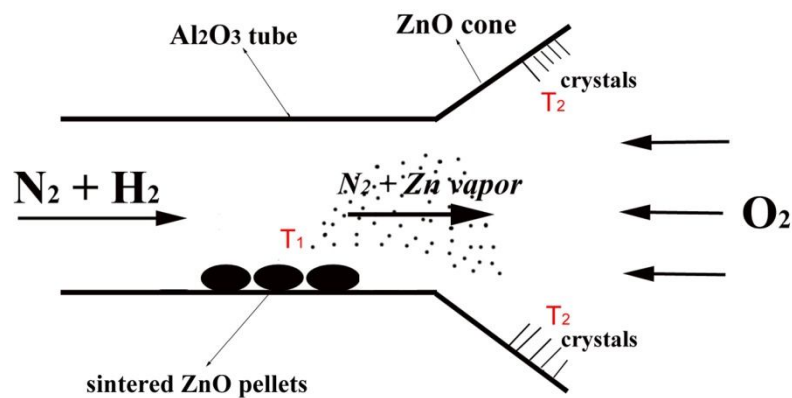
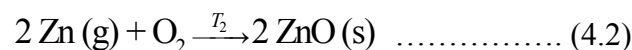


Figure 4.1 Illustration of the open-system vapor transport process for ZnO single crystals growth in horizontal Al₂O₃ tube and ZnO cone.

zinc vapor (see equation (4.2)) in the region of higher temperatures (T₂ could be varied from 1000 to 1400 °C),



ZnO nucleates at the zinc oxide cone and grows to needle-shaped single crystals at atmospheric pressure. The usual gas flow of H₂, O₂ and N₂ was chosen to be 5-50, 5-50, 500-1200 sccm (standard cubic centimeters per minute), respectively. The

growth duration was chosen from 1 to 40 h.

Table 4.1: Chemical composition of the ZnO powder and Al₂O₃ ceramic tube.

Items	Chemical composition	Content
ZnO powder	ZnO	99.9%
	Pb	10 ppm
	Cu	0.1 ppm
	Cd	1 ppm
	Fe	2 ppm
	Mn	0.1 ppm
	S	10 ppm
	Cl	10 ppm
Al ₂ O ₃ ceramic tube	Al ₂ O ₃	>99.5%
	SiO ₂	<0.1%
	Fe ₂ O ₃	<0.05%
	R ₂ O	<0.1%

The growth was performed in the HT-1800 high temperature furnace (Linn High Therm GmbH) equipped with constant water cooling and a precise digital mass flow controller meter (MKS 647C and 1179B), as shown in Figure 4.2(a). The temperature profile in the growth tube was plotted along the tube axis in Figure 4.2(b), where $x = 0$ indicates the end point of the Al₂O₃ tube outside the oven. Temperature distribution inside the tube is the most important parameter that can greatly influence the single crystal growth of ZnO. Higher temperatures lead to more zinc vapor production and to a higher growth velocity of ZnO single crystals. As depicted in Figure 4.2(b), ZnO source pellets were placed at the gray color reductive region at temperature T_1 , which was located at 39 -43 cm along the tube axis. ZnO single crystals formed at the gray color growth region at temperature T_2 , which was located at 49-50 cm along the tube axis.

In addition to the above growth configuration in Figure 4.1, two other configurations for the growth of ZnO single crystals were used. Figure 4.3 shows the use of ZnO ceramic tube without cone, ZnO single crystals grew on the tip of ZnO tube instead of the inner surface of the ZnO cone. Both configurations in Figure 4.1 and Figure 4.3 had ZnO ceramics, and ZnO ceramics can be eroded by H₂ gas. Both

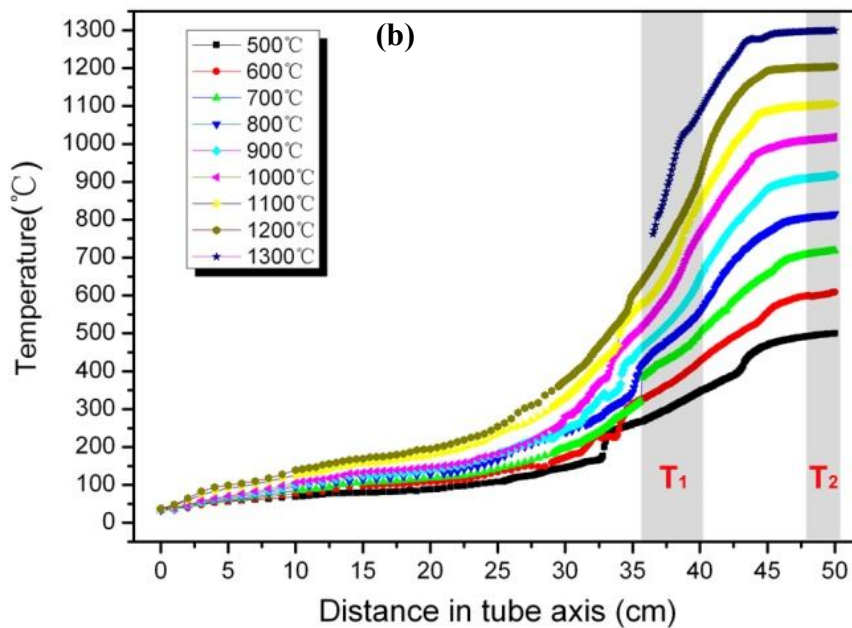
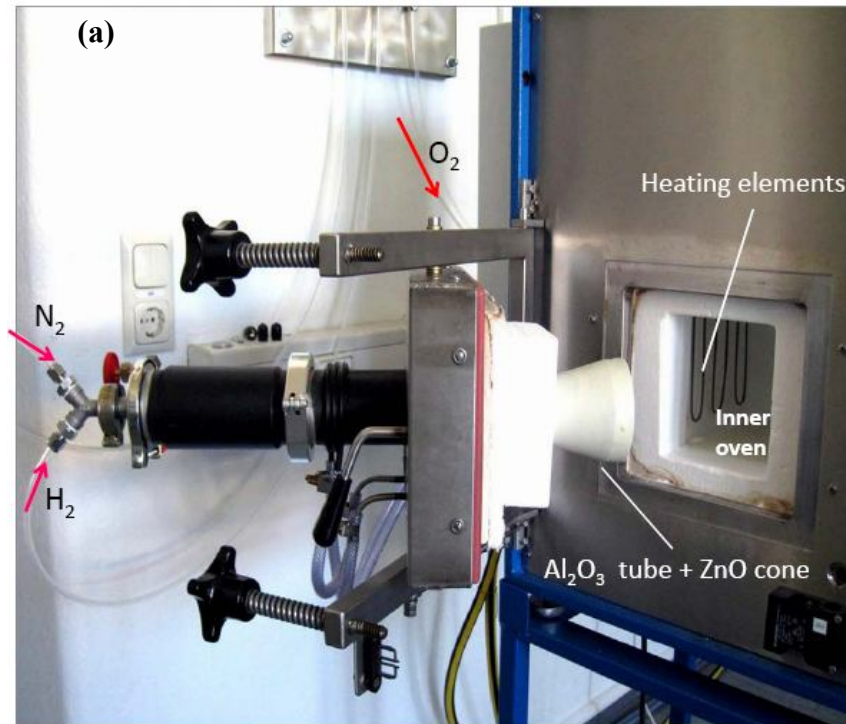


Figure 4.2 (a) the growth tube of open-system vapor transport method in HT-1800 furnace, and (b) the temperature profile in the growth tube.

of them suffered from the problem of tube breaking during the growth. Since Al_2O_3 ceramic tube cannot be eroded by H_2 gas and could be used for longer growth hours, an Al_2O_3 tube for the growth of ZnO single crystals was used as shown in Figure 4.4.

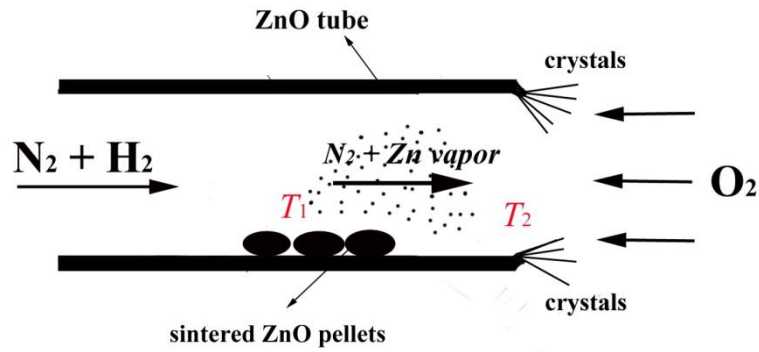


Figure 4.3: Illustration of the open-system vapor transport process for ZnO single crystals growth using a ZnO ceramic tube.

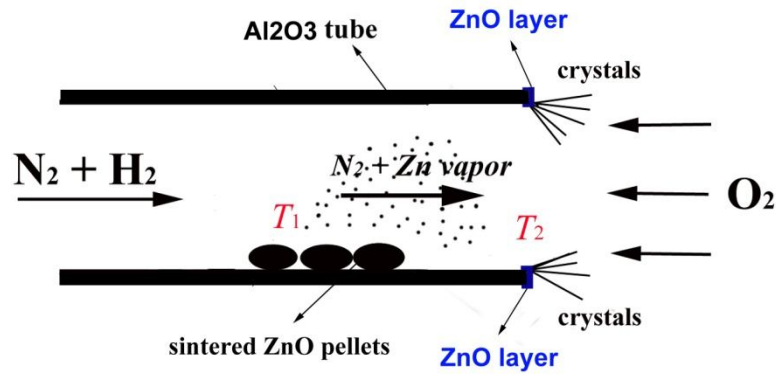


Figure 4.4: Illustration of the open-system vapor transport process for ZnO single crystals growth using an Al₂O₃ ceramic tube.

Since ZnO can easily diffuse into other ceramics, such as alumina, at high temperatures. [140], a layer of polycrystalline ZnO can be firmly coated on the tip of

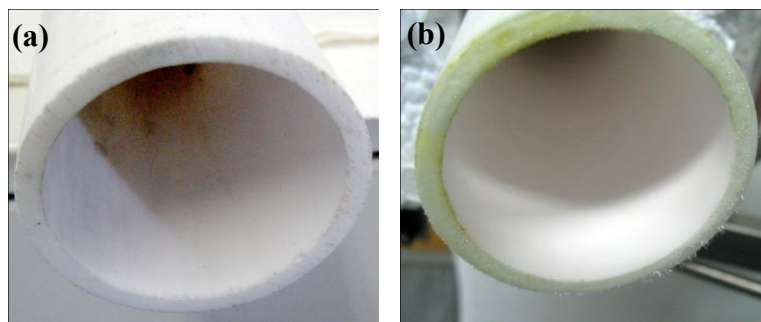


Figure 4.5: (a) original Al₂O₃ ceramic tube, and (b) coated Al₂O₃ ceramic tube with a layer of ZnO

Al₂O₃ tube, as shown in Figure 4.5, at a temperature of 1400 °C and flow rates of H₂, O₂ and N₂ gas of 21, 15, and 1200 sccm respectively,

4.3 Results

Typical clusters of ZnO single crystals grown by our vapor transport setup are located on the ZnO cone or on the tip of ZnO/Al₂O₃ tube, as shown in Figure 4.6. These needle-shaped ZnO single crystals grow on a layer of polycrystalline ZnO particles which provide the preferential nucleation sites. The as-grown needle-shaped

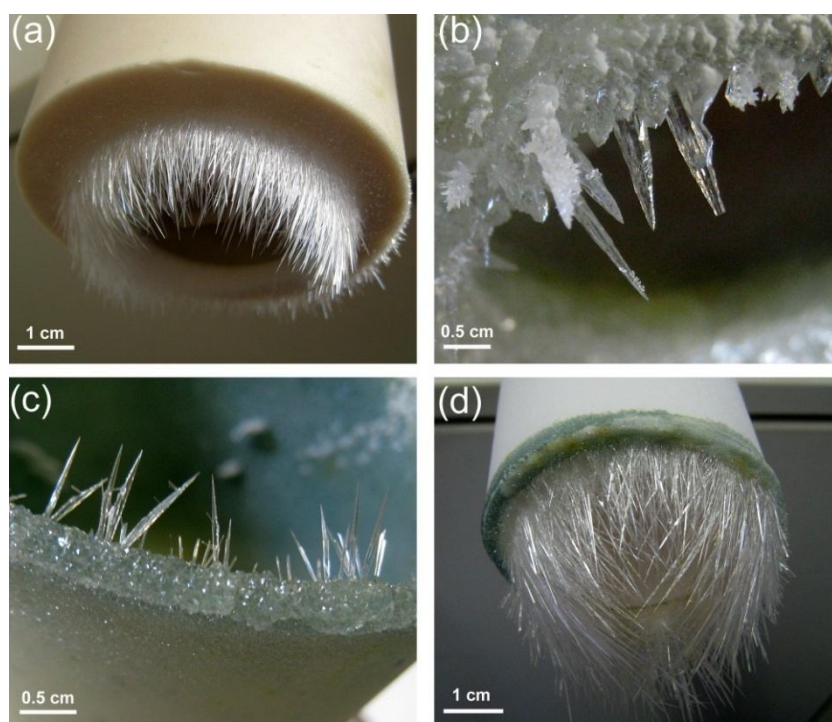


Figure 4.6: Clusters of ZnO single crystals grown by vapor transport method using (a)~(b) only ZnO tube, (c) Al₂O₃ tube + ZnO cone, (d) only Al₂O₃ tube.

crystals have typically a maximum length of 40 mm and a maximum diameter of 1 mm after a growth of 20 h. Occasionally, larger crystals can reach a diameter of 8 mm. The single crystals are transparent and clear. Typical needles are shown in Figure 4.7(a). The SEM image of a part of one needle is presented in Figure 4.7(b), which illustrates that the as-grown crystal typically has regular, flat and smooth surfaces.

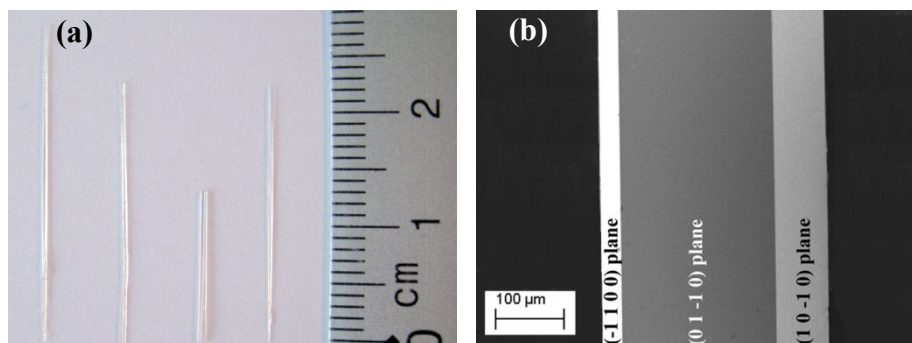


Figure 4.7: (a) Typical as-grown needle-shaped ZnO single crystals and (b) SEM image of the surface morphology of a ZnO crystal labeled with the indices of crystalline planes.

Figure 4.8(a) shows the electron backscatter diffraction (EBSD) Kikuchi pattern taken from a side face of the needle-shaped crystal, the crystals grow along the x -axis of the coordinate system in Figure 4.8(b), which is the c -axis oriented $[0001]$ direction in the

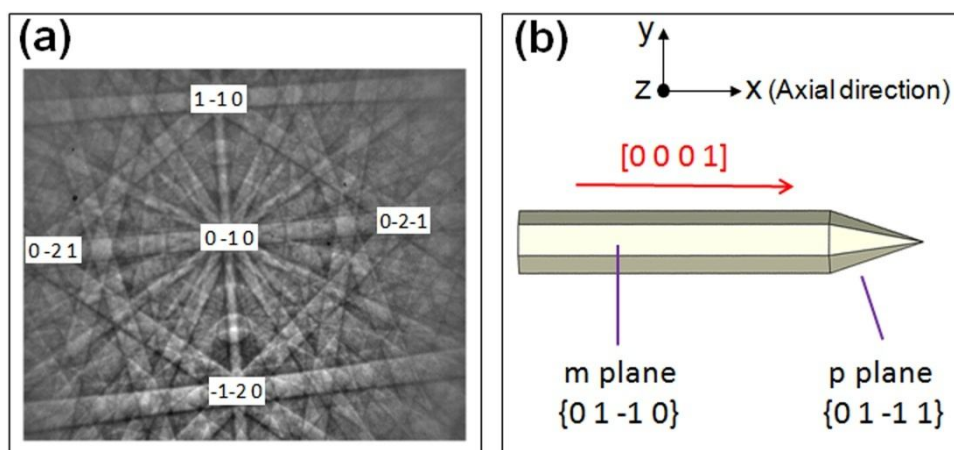


Figure 4.8: (a) Kikuchi pattern of the as-grown crystals by electron backscatter diffraction (SEM-EBSD) technique, and (b) orientation of the crystal geometry with axial polar direction and surrounding crystalline planes.

hexagonal wurtzite structure of ZnO. The surrounding side faces of regularly shaped needles are m -planes with indices $(01-10)$ and p -planes with indices $(01-11)$, as shown in the schematic model of the crystallographic geometry in Figure 4.8(b).

Low temperature PL spectra of the as-grown crystals were measured at 4.2 K to study the optical properties of the samples and the influence of the growth parameters.

Figure 4.9 represents a comparison between two samples where the growth parameters were varied quite substantially (see Table 4.2). The assignment of the PL

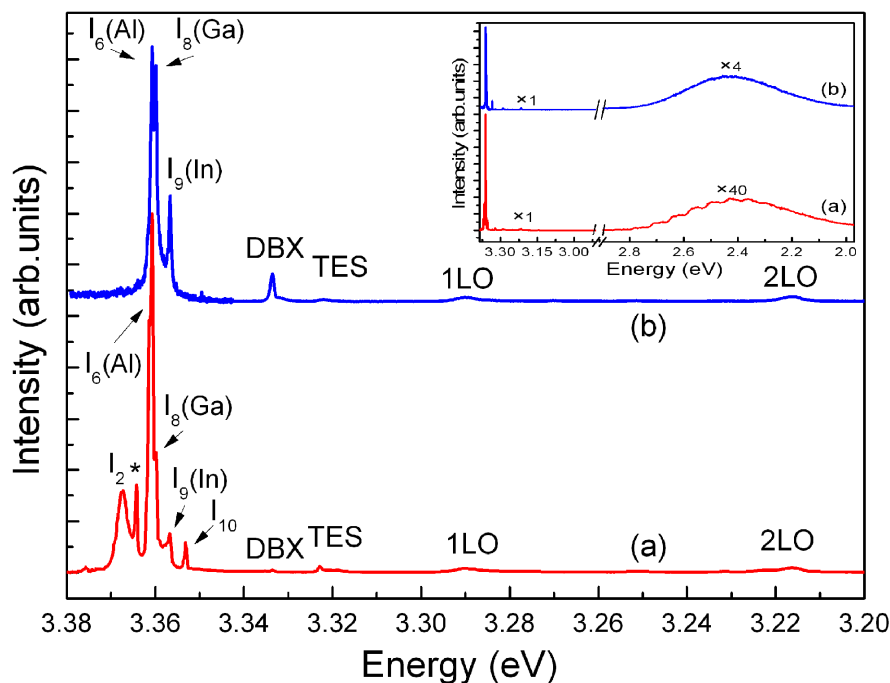


Figure 4.9: Comparison of PL spectra of two samples grown under different growth conditions (for the growth details see Table 4.2); Inset presents a wider range PL spectra of the two samples (the intensities of the green band were multiplied by a factor of 40 for sample (a) and a factor of 4 for sample (b) for better clarity).

Table 4.2: Growth parameters of two different crystals (a) and (b) used in PL measurement shown in Figure 4.9

Sample	(a)	(b)
Temperature (°C)	1300	1320
N ₂ flow rate (sccm)	800	1333
H ₂ flow rate (sccm)	8	50
O ₂ flow rate (sccm)	10	25
Growth time (h)	20	8

lines labeled in Fig.4.9 is based on the line positions, the energy separation among lines, and the comparison with literature [11]. The no-phonon excitonic range is dominated by the I_6 , I_8 , and I_9 lines, which have been attributed to the decay of bound

excitons to the neutral shallow donor impurities Al, Ga, and In, respectively. The line I_2 is the recombination of excitons bound to the ionized donor I_0 (In). The detected impurities are unintentionally introduced into the crystal during the growth or from the source material. The transition at 3.364 eV marked as * was not recognized before and will be further investigated in chapter 6. The peaks at 3.322, 3.289 and 3.216 eV are attributed to two-electron-satellites (TES) and phonon replica transitions (1LO and 2LO) of the bound excitons, respectively. The sharp line at 3.333 eV labeled DBX was assigned to the recombination of excitons bound to structural defects [11]. Making the assumption that the PL intensities of the peak at 3.333 eV is proportional to the densities of DBX-related structural defects; sample (a) shows significantly lower density of structural defects. The inset in Figure 4.9 presents a wider spectral range. The broad PL band in the green spectral region is different in both samples. The structure-less band in sample (b) is assigned in the literature to an oxygen vacancy defect [141] or an zinc vacancy defect [79], whereas sample (a) shows the characteristic structure of Cu-related green band [96].

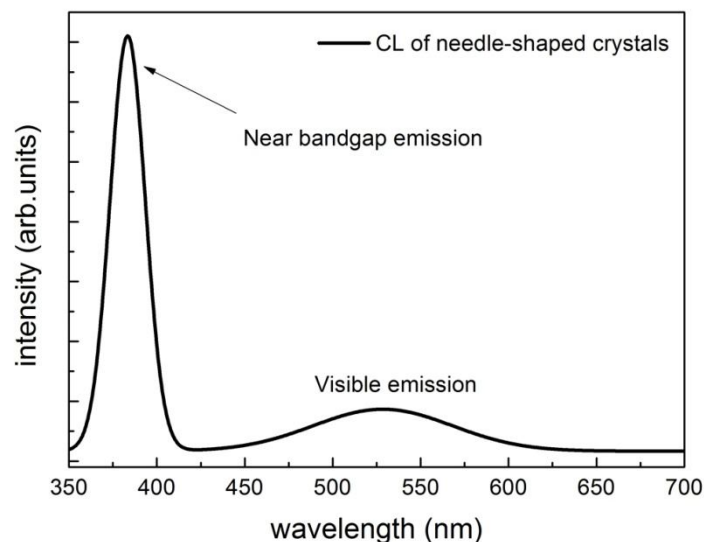


Figure 4.10: Room temperature cathodoluminescence of needle crystal grown by vapor transport method

Room temperature CL was also employed to characterize the needle crystals at

room temperature. Spectra are shown in Figure 4.10. The luminescence spectrum consists of the strong and sharp near band gap emission and the broad visible green emission, this behavior was also found in the room temperature PL spectra.

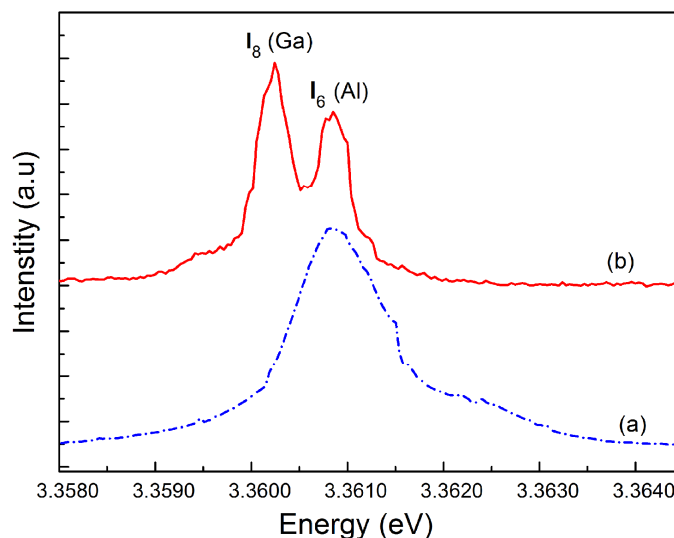


Figure 4.11: PL spectra measured at 4.2 K for the comparison ZnO single crystals between (a) HT crystals purchased from Crystec GmbH and (b) one of our vapor phase grown crystals.

Figure 4.11 compares the PL spectra (measured at 4.2 K) of a hydrothermally grown (Crystec GmbH) (a) and our vapor phase grown (b) ZnO crystal in the excitonic spectra range. The HT sample exhibits only the Al-bound exciton at 3.3608 eV. In sample (b) the Al-bound exciton and the Ga-bound exciton are detected. The spectrum of sample (a) shows in addition some other small peaks (I_9 or I_{10}) at energy between 3.3613 eV and 3.3630 eV, since the Al-related peak has a perfect Gaussian shape on its left side at 3.3600 eV \sim 3.3608 eV, it's possible to estimate the halfwidth of this Al-related peak. The halfwidth of the PL line in our vapor phase grown sample is smaller ($\Delta\lambda = 0.03 - 0.04$ nm) compared to the line in the commercially available hydrothermal crystal ($\Delta\lambda = 0.12$ nm). The broadening of the spectral linewidth indicates additional residual inhomogeneous strain fields or electrical fields in the sample, which could originate from inhomogeneous impurity contaminations, extended defects, or a lower crystallinity.

The conductivity of the as-grown needle-shaped ZnO crystals is n-type from

thermoelectric measurements or donor-dominated PL spectra. The temperature dependent thermoelectric power (TEP) is $-250 \mu\text{V/K}$ at room temperature by measuring the temperature difference and voltage between two ohmic contacts along c-axis [142]. The electrical resistivities of the samples were derived from I-V curves, which were measured between two Ohmic contacts made with In-Ga alloy at room temperature. Resistivities in the range of $0.5 \times 10^2 - 1.0 \times 10^2 \Omega \cdot \text{cm}$ were detected, which correspond to a free carrier concentration of about $0.5 \times 10^{15} \text{ cm}^{-3}$ (assuming a typical room temperature electron mobility of $140 \text{ cm}^2/\text{V} \cdot \text{s}$ [110]).

4.4 Dominant factors in crystal growth

The growth of ZnO single crystals in our open-system vapor phase setup depends on several factors. The growth duration, temperature, gas flow rate and source material, all influence the process of growth, the size, shape and optical properties of the crystals.

4.4.1 Growth duration

To investigate the specific influence of the growth duration in our vapor phase process, growth duration were selected from 2 h to 16 h, while keeping other parameters constant (furnace temperature $T = 1400 \text{ }^\circ\text{C}$, gas flow rate $f_{\text{N}_2} = 932 \text{ sccm}$, $f_{\text{H}_2} = 35 \text{ sccm}$, $f_{\text{O}_2} = 30 \text{ sccm}$). Pictures are shown in Figure 4.12. The crystal length is not proportional to the growth time. The growth rate in the first 4 hours is much slower than that in later hours. The growth rate ratio in c-direction and the direction perpendicular to c-axis is lower in beginning hours and gets faster in later hours. At first 4 hours, the diameter of needle crystals is quite small and even smaller than the diameter of its polycrystalline seeds. When the diameter of the needles reaches around 1 mm, it is difficult to increase it any more.

Generally, the longer the growth, the larger the ZnO crystal will be. However, it's not always the case. Firstly, the anisotropic feature of fairly fast growth in c direction

and relatively slow growth in other directions also restrain the diameter of

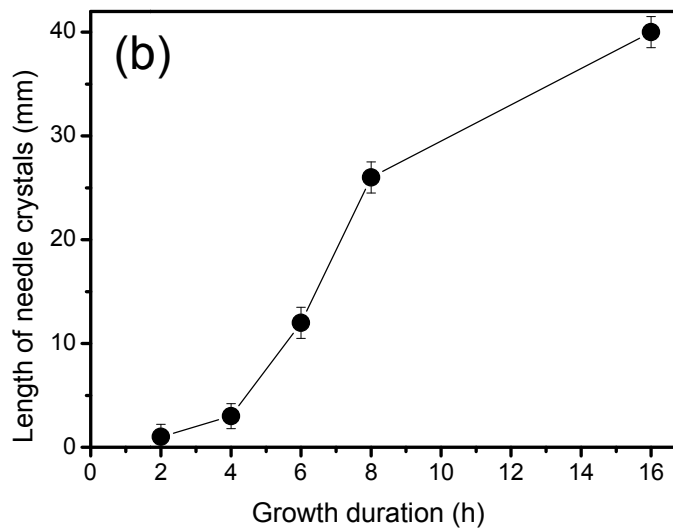
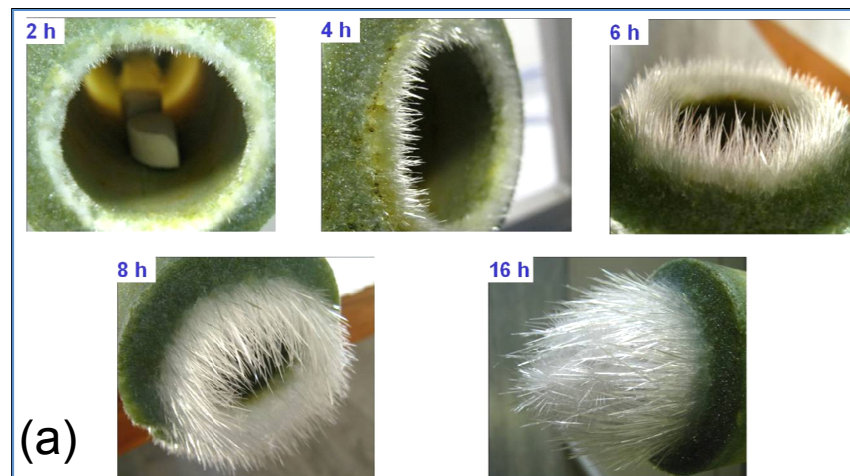


Figure 4.12: (a) The growth of ZnO crystals by vapor phase method at different duration hours while keeping other parameters the same, (b) average length of needle crystals vs. growth duration

ZnO crystals. Secondly, if the nucleation density near the tube tip is too high, the ceramic tube will be closed by the clusters of needle crystals. These are obstacles to get larger size of ZnO single crystal in the vapor phase method.

4.4.2 Growth temperature

While keeping a constant growth duration (8 h) and identical gas flow rates ($f_{N_2} =$

932 sccm, $f_{\text{H}_2} = 35$ sccm, $f_{\text{O}_2} = 30$ sccm), different furnace temperatures were selected from 1100 °C to 1400 °C and the results of growth were shown in Figure 4.13. If the furnace temperature was set to be lower than 1100 °C, no ZnO crystals are obtained; a growth temperature above 1400 °C for long hours is not allowed in our furnace. The growth temperature is the most significant factor for the growth of ZnO single crystals. It influences not only the reductive reaction of source materials, but also affects the nucleation on tube tip and the surface diffusions of atoms on the growing crystals. Crystal size and crystalline quality were improved with increase of furnace temperature from 1100 °C to 1400 °C. The reason seems to be the faster surface diffusion of atoms at higher growth temperature.



Figure 4.13: The growth of ZnO crystals by vapor phase method at different temperatures while keeping other parameters the same.

4.4.3 Gas flow rates

Influence of N_2 gas flow: N_2 gas is used as carrier gas to transport zinc vapor from the reductive region to the growth region. N_2 gas flow can also indirectly influence the crystal growth. As described in Figure 4.14, when the furnace temperature (1400 °C), growth duration (8 h), and flow rate of H_2 , O_2 ($f_{\text{H}_2} = 14$ sccm, $f_{\text{O}_2} = 12$ sccm) are fixed, N_2 flow rates are changed from 0.280 SLM (standard liters per minute) to 0.746 SLM. As shown in Figure 4.14, lower N_2 flow rates led to no crystal growth and

higher N_2 flows rate led to fast growth of ZnO needles. This could be understood by the reaction balance of ZnO reduction: $ZnO(s) + H_2 \rightleftharpoons Zn(g) + H_2O(g)$. At lower carrier (N_2) flow rate, the reduced zinc vapor cannot be effectively transported to



Figure 4.14: The growth of ZnO crystals by vapor phase method at different N_2 flow rates while keeping other parameters the same.

growth region and accumulated near the source ZnO pellets, which prevents the reaction balance to proceed towards the right direction. Little zinc vapor will be transported to the growth region, slower or even no crystal growth will happen. Contrarily, higher carrier flow rate will help the reaction balance to proceed towards right direction. More zinc vapors will be transported and faster crystal growth will be obtained. The proper flow rate for N_2 is 500 – 900 sccm.

Influence of H_2 gas flow: The role of H_2 gas flow is mainly to reduce the source material. When the H_2 flow rate is not so high (< 30 sccm), with the increase of H_2 flow rate, more zinc vapors will be produced and larger needle crystals will be obtained. However, too high H_2 flow rate should be avoided since it will introduce safety issues because of the explosion limit of H_2 gas at higher temperature [143, 144]; in addition, excessive H_2 gas will reduce the as-grown ZnO crystals again, or will produce more water vapors with O_2 .

Influence of O_2 gas flow: When the furnace temperature is above 1200 °C, and the flow rates of N_2 , H_2 are higher than 600 sccm, 15 sccm respectively, the higher the O_2 flow rate, the larger crystal we will get. When the N_2 flow rates are relatively low (eg $f_{N_2} < 600$ sccm), no needle crystals will be obtained if the O_2 flow rate is too high or too low. In other words, a suitable ratio of flow rates between O_2 and H_2 should be

fixed and this ratio is typically 0.5 -1.3 in our vapor phase growth. When the ratio is too small, most of the O_2 will be consumed by excessive H_2 , and there will be no crystals. When the ratio is too high, a portion of the excessive O_2 can flow into the growth tube to consume more H_2 gas and affect the reductive reaction of ZnO pellets.

The optimized gas flow rates for N_2 , H_2 and O_2 for the single crystal growth are around 800 sccm, 8 sccm and 10 sccm respectively.

4.4.4 Source material

The source material used is isostatically pressed ZnO powders, which were sintered at 800 °C to prevent too fast reductive reactions. How will the source material influence the crystal growth process? The answer is the zinc vapors production by reductive reactions. The reductive reactions are determined by the furnace temperature and gas flow rates. Since the weight loss of source ZnO pellets is proportional to the amount of produced zinc vapors, the weight loss of ZnO pellets was record to investigate the dependence on temperature and gas flow rates.

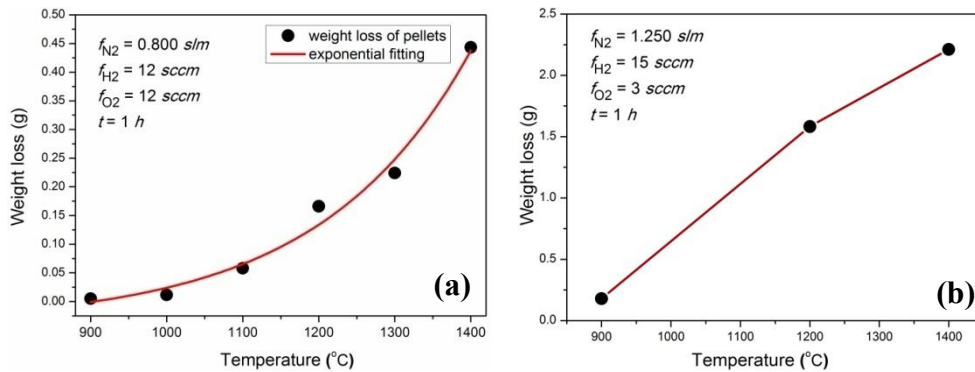


Figure 4.15: The weight loss of source ZnO pellets vs. furnace temperature at following conditions (a) flow rates $f_{N_2} = 0.800 \text{ slm}$, $f_{H_2} = 12 \text{ sccm}$, $f_{O_2} = 12 \text{ sccm}$, growth duration $t = 1 \text{ h}$ and (b) flow rates $f_{N_2} = 1.250 \text{ slm}$, $f_{H_2} = 15 \text{ sccm}$, $f_{O_2} = 3 \text{ sccm}$, growth duration $t = 1 \text{ h}$.

Dependence on furnace temperature: The weight loss of the ZnO source pellets vs. furnace temperature was plotted in Figure 4.15, two substantially different conditions ((a) flow rates $f_{N_2} = 0.800 \text{ slm}$, $f_{H_2} = 12 \text{ sccm}$, $f_{O_2} = 12 \text{ sccm}$, growth duration $t = 1 \text{ h}$

and (b) flow rates $f_{N_2} = 1.250$ slm, $f_{H_2} = 15$ sccm, $f_{O_2} = 3$ sccm, growth duration $t = 1$ h) give the same trend of the weight loss on temperature. Higher furnace temperature leads to larger weight loss of the ZnO source pellets. In other words, more zinc vapors could be produced and transported at higher furnace temperature. The different curvatures of the plotted curves are caused by the distinctive growth temperatures. When the flow rates ratio between H_2 and O_2 is close to 1:1, the reductive reaction of ZnO source pellets is most preferable in our vapor growth setup, and the weight loss of source pellets also increases faster with increasing temperature.

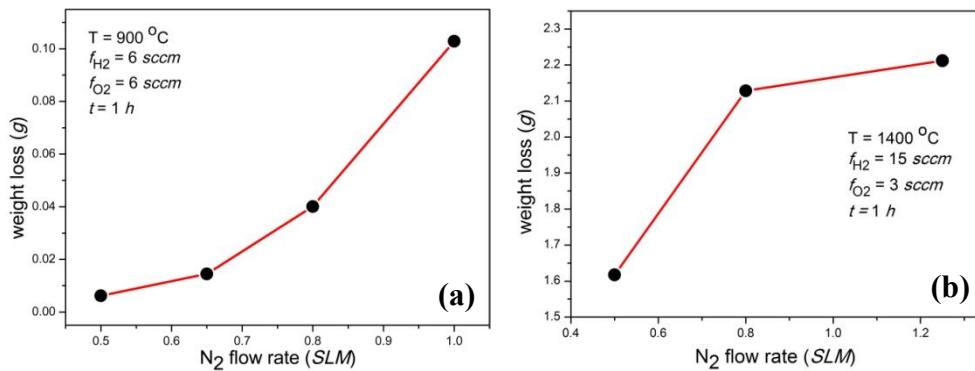


Figure 4.16: The weight loss of source ZnO pellets vs. N_2 flow rate at following conditions (a) furnace temperature $T = 900$ °C, flow rates $f_{H_2} = 6$ sccm, $f_{O_2} = 6$ sccm, growth duration $t = 1$ h and (b) furnace temperature $T = 1400$ °C, flow rates $f_{H_2} = 15$ sccm, $f_{O_2} = 3$ sccm, growth duration $t = 1$ h.

Dependence on N_2 flow rate: The weight loss of source ZnO pellets vs. the flow rate of carrier gas (N_2) at conditions (a) and (b) with distinctive parameters was plotted in Figure 4.16. Higher carrier gas flow rates result in larger weight loss of the ZnO pellets and more production of zinc vapors. This was already explained by the balance and direction of reductive reaction in section 4.4.3. Higher H_2 flow rates and higher furnace temperatures in condition (b) are easier to achieve the saturation reduction of ZnO pellets, which results in the different shapes of the plotted curves in Figure 4.16(a) and Figure 4.16(b).

Dependence on H_2 flow rate: The weight loss of source ZnO pellets vs. the flow rate of H_2 for different growth conditions (a) and (b) was plotted in Figure 4.17. The

main trend is that, the weight loss of source material is proportional to the H_2 flow rate; because the H_2 consumption is just proportional to the weight loss of ZnO source in the reductive reaction. However, when the H_2 gas flow is much smaller than that of O_2 , the weight loss of ZnO source is almost zero, as shown in Figure 4.17(b). This is because the H_2 gas with very small flow rates was consumed by large flow rates O_2 gas.

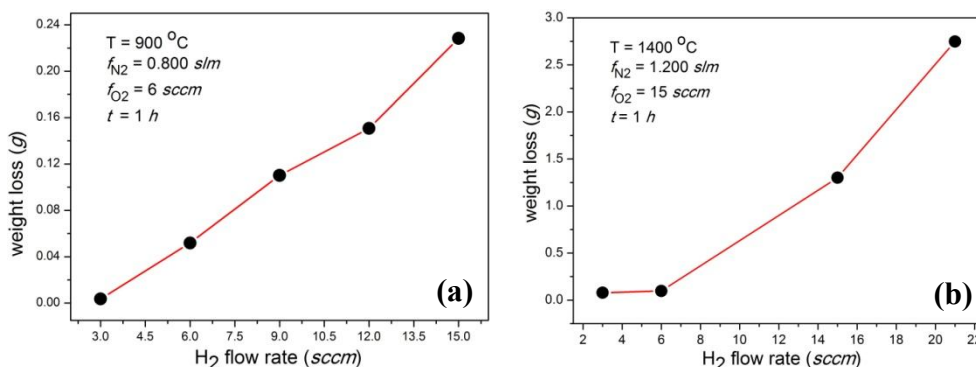


Figure 4.17: The weight loss of source ZnO pellets vs. H_2 flow rate at following conditions (a) furnace temperature $T = 900\text{ }^\circ\text{C}$, flow rates $f_{N_2} = 0.800\text{ slm}$, $f_{O_2} = 6\text{ sccm}$, growth duration $t = 1\text{ h}$ and (b) furnace temperature $T = 1400\text{ }^\circ\text{C}$, flow rates $f_{N_2} = 1.200\text{ slm}$, $f_{O_2} = 15\text{ sccm}$, growth duration $t = 1\text{ h}$.

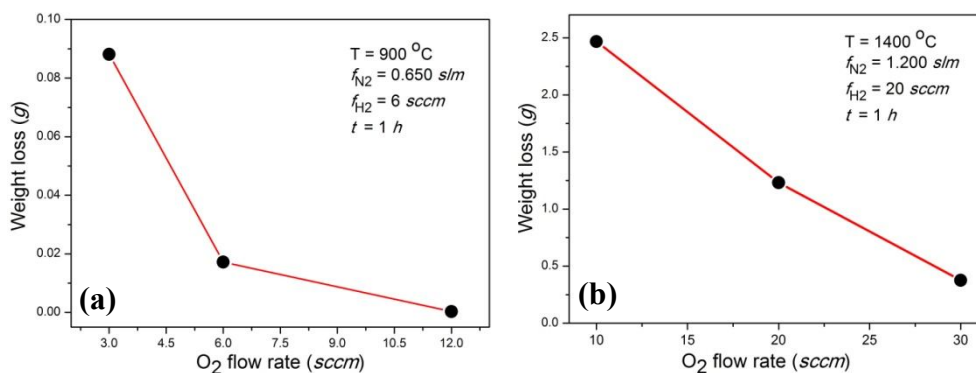


Figure 4.18: The weight loss of source ZnO pellets vs. O_2 flow rate at following conditions (a) furnace temperature $T = 900\text{ }^\circ\text{C}$, flow rates $f_{N_2} = 0.650\text{ slm}$, $f_{H_2} = 6\text{ sccm}$, growth duration $t = 1\text{ h}$ and (b) furnace temperature $T = 1400\text{ }^\circ\text{C}$, flow rates $f_{N_2} = 1.200\text{ slm}$, $f_{H_2} = 20\text{ sccm}$, growth duration $t = 1\text{ h}$.

Dependence on O_2 flow rate: The weight loss of the ZnO source pellets vs. the flow rate of O_2 at different conditions (a) and (b) was plotted in Figure 4.18. The reductive reaction is inversely proportional to the H_2 flow rate. An important reason accounts

for it is that a portion of O_2 flows into the reductive region. With the increase of O_2 flow rate, more H_2 gas will be consumed by oxygen. In addition, the byproduct water vapor is also an obstacle of the reductive reaction of source materials.

4.5 Discussion

The growth of ZnO single crystals was achieved by the vapor phase method without finely prepared seeds crystals, the elimination of seeds crystals greatly reduce the cost and the complexity of the crystal growth. Although there are no large-size single crystal seeds in our open-system vapor phase method, there are actually polycrystalline seeds on the inner surface of the ZnO cone and on the tip of the ZnO or Al_2O_3 tube. ZnO forms from the gaseous reaction between zinc vapor and O_2 , and nucleates on these polycrystalline seeds. Low density and larger size polycrystalline seeds, lead to lower density and the larger size the needle crystals.

In the growth region, the supersaturated vapor is not at equilibrium. In order to relieve the supersaturation and move towards equilibrium, the vapor crystallizes. The crystallization of ZnO is actually a combination of two processes: nucleation and crystal growth. The vapor supersaturation is an important parameter in both processes.

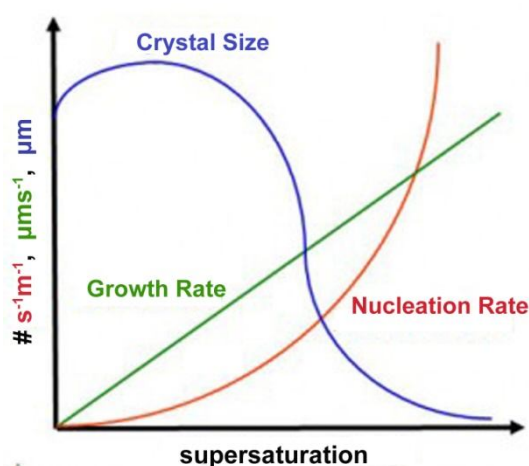


Figure 4.19: The influence of supersaturation on the nucleation rate, growth rate and crystal size [145].

The influence of supersaturation on crystallization is illustrated in Figure 4.19 [145]: At lower supersaturation, the growth rate of crystals is higher than the nucleation rate of nucleus, which will result in a larger crystal size. However, at higher supersaturation, the nucleation process overwhelmingly dominates the crystal growth, the size of the critical nucleus decreases and the number of the nucleus dramatically increases with increasing supersaturation [146], which ultimately results in smaller crystals. Therefore lower vapor saturation is suitable for the growth of ZnO single crystals from vapor phase.

In the growth of ZnO single crystals from vapor phase, the molecule diffusion on the growing crystal surface is considered to be the rate-controlling step. Generally the growth rate increases and the nucleation rate decreases with increasing temperatures for a given vapor supersaturation, it is attributed to the faster rate of incorporation of the absorbed molecule layer onto the growing crystal surface, and the faster surface diffusion of molecules on growing crystal surface at higher temperature.

At high vapor supersaturation, spontaneous nucleation happens; the growth usually results in high density of needle crystals, as shown in Figure 4.6 (d). One important reason is the spontaneous nucleation on high density of polycrystalline particle seeds. It will result in crowded growth space and prevent the further growth to larger size crystals.



Figure 4.20: Dendritic growth by high supersaturation of zinc vapor

Secondary nucleation results from the presence of growing crystals in the high

supersaturated vapor. These parent crystals have a catalyzing effect on the secondary nucleation phenomena. One notable problem arising from the secondary nucleation is the dendritic growth. It is probably formed by dust breeding. The dendritic crystals or whisker crystals appear on the as-grown crystals as shown in Figure 4.20 and 4.6(c). The dendritic crystals restrain the size of needle-shaped crystals, introduce additional structures defects and decrease the crystalline quality.

To get an optimized vapor supersaturation for the growth of ZnO single crystals, the growth parameters were optimized. Especially the H₂ flow rates and growth temperatures were selected in the range 5 ~ 10 sccm and 1300 ~ 1400 °C, respectively. How these parameters influence the crystal growth is focused in 3 points: the reductive reaction of source material, the nucleation of ZnO from the supersaturated vapor and the surface diffusion of ZnO atoms on the growing crystal.

The volume fraction of H₂ in the mixture of H₂, O₂ and N₂ should be limited to avoid the risk of explosion at temperatures above 1000 °C. In addition, excessive H₂ will “kill” the growing ZnO single crystals. Residual H₂ in the gas could introduce background donor concentration in the as-grown crystals.

4.6 Conclusion

The seed-free and open-system vapor phase method is a simple and low cost approach to grow good quality ZnO single crystals. The as-grown crystals are generally needle-shaped in morphology; and the largest crystals obtained are typically c-axis oriented needles with maximum length of 40 mm and maximum diameter of 1 mm. The needle-shaped crystals are n-type with main donors due to Al, Ga, and In impurities. The optimized gas flow rates of N₂, H₂ and O₂ for larger diameter needle crystals are around 800 sccm, 8 sccm and 10 sccm respectively. And the optimized growth was carried out at the temperature between 1300 °C and 1400 °C in the Al₂O₃ tube.

Chapter 5

Vapor phase growth of ZnO thin films on Si substrates

This chapter will describe the growth of ZnO thin films on Si substrates by the vapor phase method. Three different configurations of source material, oxidizers and growth tubes will be applied and compared in this chapter.

5.1 Introduction

To reduce the strains and dislocation density in epitaxial ZnO and related films, closely lattice-matched substrates are favored. In addition to ZnO substrates and GaN substrates, Sapphire, SiC, ScAlMgO₄ substrates are most commonly used for the epitaxial deposition of ZnO thin films [6]. A typical feature of the above substrates is that most of them share the same hexagonal structure with ZnO. Substrates with different crystalline structures, such as cubic Si, are more difficult to grow on high quality epitaxial ZnO layers; Furthermore, amorphous SiO_x layers will form between Si substrate and ZnO film. Both large-lattice-mismatch and amorphous layers deteriorate the quality of the deposited films. In spite of these difficulties, ZnO films on Si substrates are potentially needed in the integration of ZnO optoelectronics and traditional Si IC technology, such as transparent conductive oxide (TCO) contacts in silicon photovoltaics, or surface passivation layers on silicon devices [1, 147]. The following sections will be devoted to the vapor phase growth of ZnO thin film on Si substrates.

5.2 Growth principles and growth setup

The growth of ZnO thin films on Si substrates by vapor phase method was carried out in the same furnace setup shown in Figure 4.2 of chapter 4. However, different growth tubes were employed. The growth principles of ZnO films by vapor phase

method can be described by the illustration in Figure 5.1. Two concentric Al_2O_3 ceramic tubes (Anderman industrial ceramics, 99.8wt.% Al_2O_3 + 0.1wt.% SiO_2 , the dimensions are shown in Table 5.1) were bonded to a metal connector by an ceramic adhesive (Sauereisen Zement Nr.2). Two gas inlets were drilled on the metal connector, one for the flowing of N_2 and H_2 is connected to the inner space of smaller tube, and the other for the flowing of O_2 is connected to the space between two tubes. 8 uniformly distributed holes (10 mm in diameter) were drilled near the end of the smaller tube for the flowing of O_2 gas.

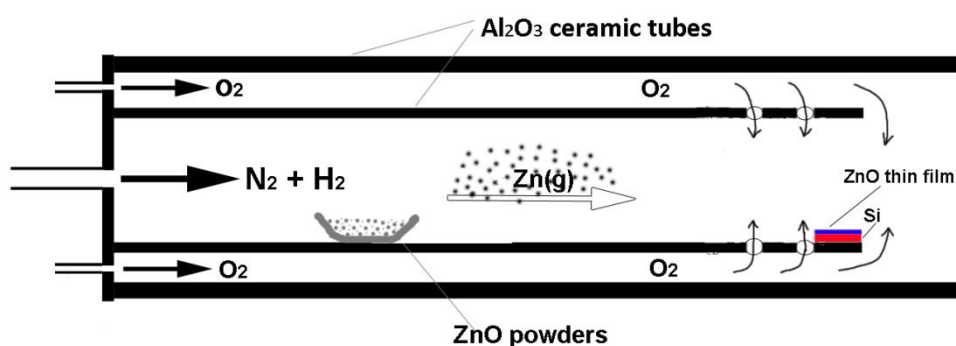


Figure 5.1: Illustration of the open-system vapor transport process for ZnO thin films on Si substrates in horizontal concentric Al_2O_3 tubes with ZnO powders as source materials.

The temperature profile along the tube axis is similar to that in Figure 4.2 of chapter 4. The source materials are in the form of ZnO powders (Chempur, 99.9% in purity).

Table 5.1: The dimensions of the Al_2O_3 growth tubes

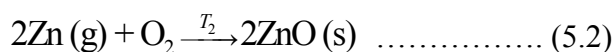
Items	Inner diameter	Outer diameter	Length
Smaller tube	38 mm	30 mm	500 mm
Larger tube	58 mm	48 mm	560 mm

A quartz boat filled with ZnO powders were placed in the smaller horizontal Al_2O_3 tube at elevated temperature (T_1 varying from 850 to 900 °C), Zinc vapor was produced

by the reaction in equation (5.1) and transported to the growth region by the carrier



gas N₂. The Si substrates at temperature T₂ were placed at the end of the small tube (T₂ was varied from 780 to 830 °C). Near the substrate surface, ZnO formed as described by equation (5.2), nucleated on the Si substrate, and finally grew to uniform epitaxial films.



Prior to the growth, the Si substrates ((100) and (111) planes were selected) were treated to remove the surface oxide layer: i) 5 min ultrasonic cleaning in 70 °C acetone, 3 min ultrasonic cleaning in de-ionized H₂O, ii) 5 min ultrasonic cleaning in 70 °C ethanol, 3 min ultrasonic cleaning in de-ionized H₂O, iii) 60 seconds etching in 10% HF solution, 3 min ultrasonic cleaning in de-ionized H₂O, iv) drying the Si substrates by flowing N₂ gas.

The typical flow rate for N₂, H₂ and O₂ are 600 sccm, 10 sccm and 10sccm respectively. The growth duration is chosen to be 0.5 - 2 h. Besides the above configuration method (labeled as *type I method*), we used 2 modifications of the growth method to improve the quality of the ZnO films on Si substrates.

In order to reduce the influence of large lattice mismatch and the SiO_x amorphous layer, ZnO seed layer were prepared on freshly etched Si substrates in following modified type II and type III methods. The seed layer was prepared by spin-coating 5 mM Zn(CH₃COO)₂ dissolved in ethanol and was subsequently annealed in O₂ at 300 °C for 30 min.

Type II method. The source material was changed from ZnO powders to Zn powders. The zinc vapor was generated by the thermal evaporation and transported by N₂ gas, as shown in Figure 5.2. No H₂ was involved in this process and lower

temperature was needed for the growth of ZnO thin films (T_2 was varied from 600 °C to 670 °C). The typical flow rate for N_2 and O_2 are 600 sccm and 4 sccm respectively. The growth duration is typically 0.5 – 2 h.

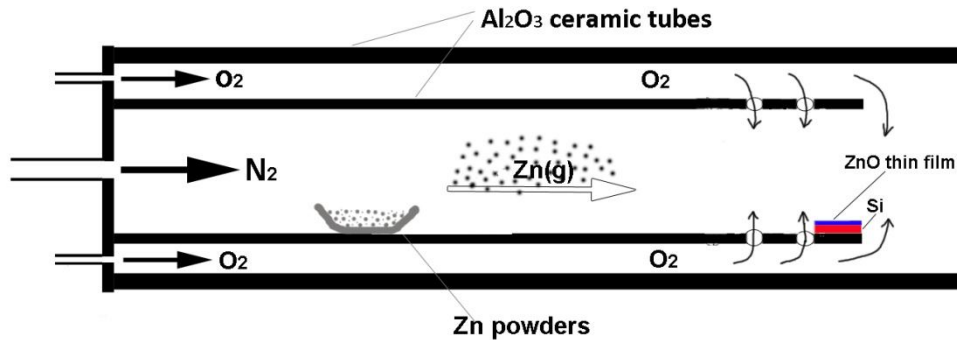


Figure 5.2: Illustration of the open-system vapor transport process for ZnO thin films on Si substrates in horizontal concentric Al_2O_3 tubes with Zn powders as source materials.

Type III method. Zn powder was chosen for the source materials; Since H_2O is a weaker oxidizer compared with O_2 , and weaker oxidizer was reported to be beneficial to the growth of homogeneous films [148], The oxidizer was replaced by H_2O vapor, which was carried by the Ar gas flow through heated water.

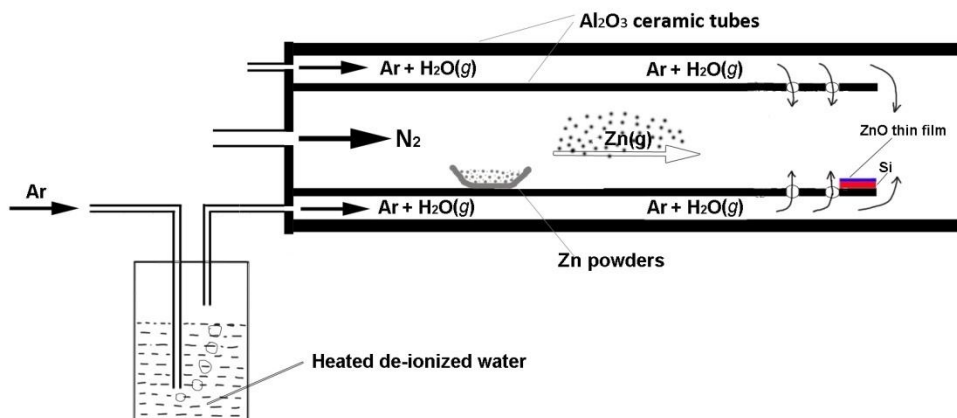


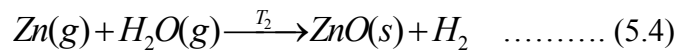
Figure 5.3: Illustration of the open-system vapor transport process for ZnO thin films on Si substrates in horizontal concentric Al_2O_3 tubes with H_2O as the oxidizer and Zn powders as source materials.

The vapor pressure of water [149] is dependent on the temperature and can be

approximated by equation (5.3). For example, when the de-ionized water was kept at

$$P_{H_2O} = \frac{1}{760} \exp\left(20.386 - \frac{5132K}{T(K)}\right) \text{ atm} \dots\dots\dots (5.3)$$

55 °C and the Ar flow rate is 50 sccm, the corresponding flow rate of water vapor will be about 7 sccm. The weaker oxidizer H₂O vapor reacts with zinc vapors as shown in equation (5.4)



(The temperature T₂ at growth region was varied from 600 °C to 670 °C). The typical flow rate for N₂, and Ar are 600 sccm, and 50 sccm respectively. The growth duration is chosen to be 0.5 – 2 h.

5.3 Results

For the type I vapor phase method, the SEM images of the as-grown ZnO thin films on (100) Si substrates are shown in Figure 5.4. The main feature of the surface

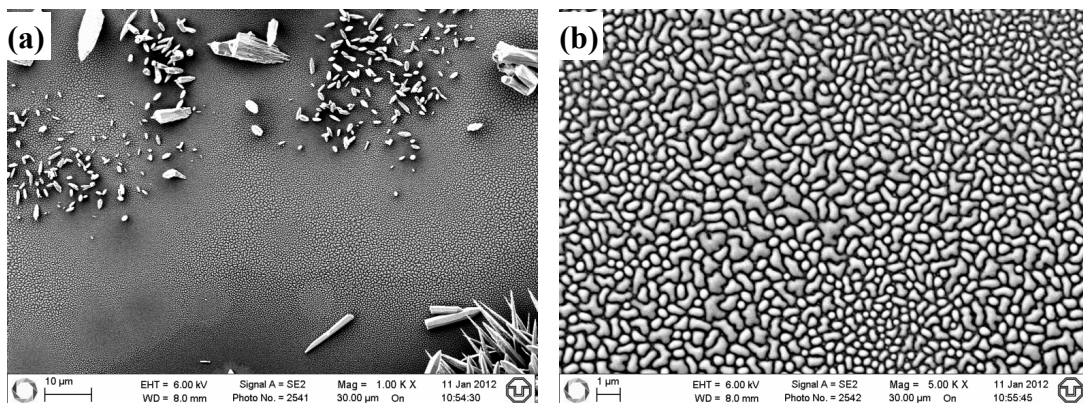


Figure 5.4: Typical SEM image of ZnO thin films on Si substrates grown by the type I vapor phase method, the image (b) is an enlargement of the central area in the image (a).

morphology is homogeneous bread-shaped particles together with some isolated microcrystals lying on the film surface. XRD spectra in Figure 5.5 show that the ZnO

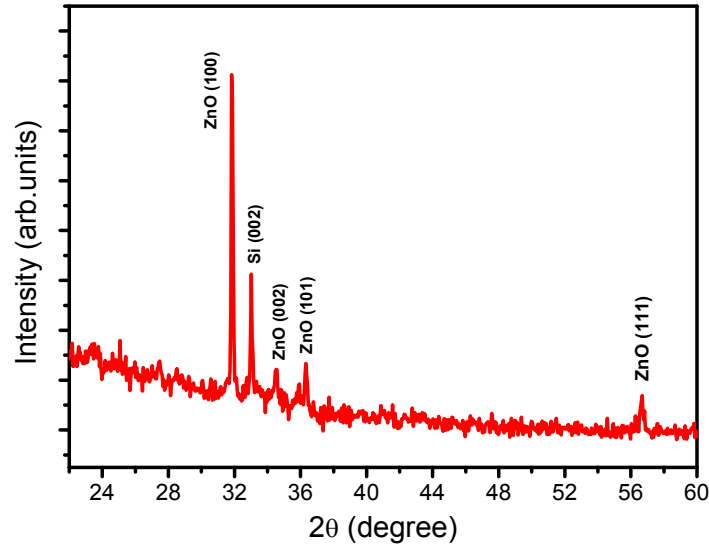


Figure 5.5: The XRD spectra of a ZnO thin film on (100) Si substrates grown by the type I vapor phase method.

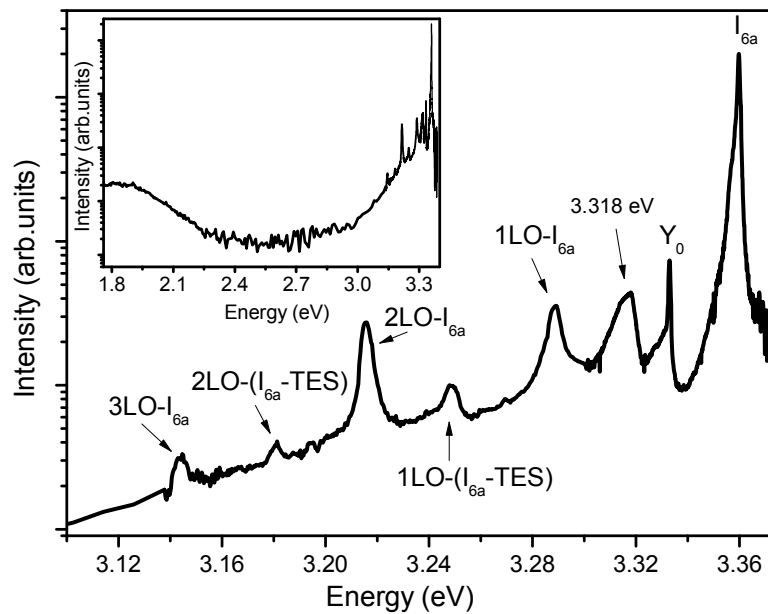


Figure 5.6: The PL spectra of an ZnO thin film on Si substrates grown by the type I vapor phase method, the insert shows the spectra of wider range from UV to visible.

thin films grown by the type I method have (100) preferential orientation. The PL spectra of the ZnO film samples are recorded in Figure 5.6, the emission intensity is

dominated by the Al related I_{6a} line and its phonon replicas. Y_0 stands for the transition of an exciton bound to structural defect. The peak at 3.318 eV is the transition of free electron to acceptor, and its origin was proved to be stacking faults by Cathodoluminescence (CL) and transmission electron microscope (TEM) [68].

For the type II vapor phase method, homogeneous ZnO layers are obtained on both (100) and (111) Si substrates and the characteristic surface morphology is microrods as shown in the SEM images in Figure 5.7. The XRD spectra in Figure 5.8 shows that the ZnO thin films on (100) and (111) Si substrates have always the (002) preferential orientation.

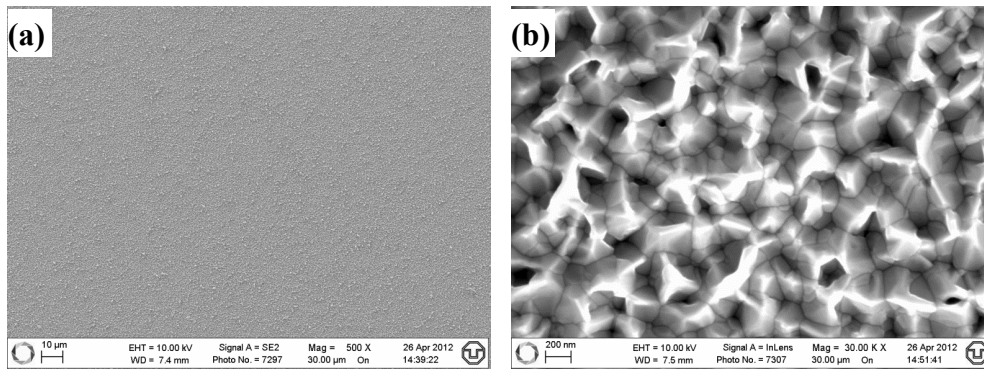


Figure 5.7: Typical SEM image of ZnO thin films on Si substrates grown by the type II vapor phase method, the image (b) is an enlargement of the central area in the image (a)

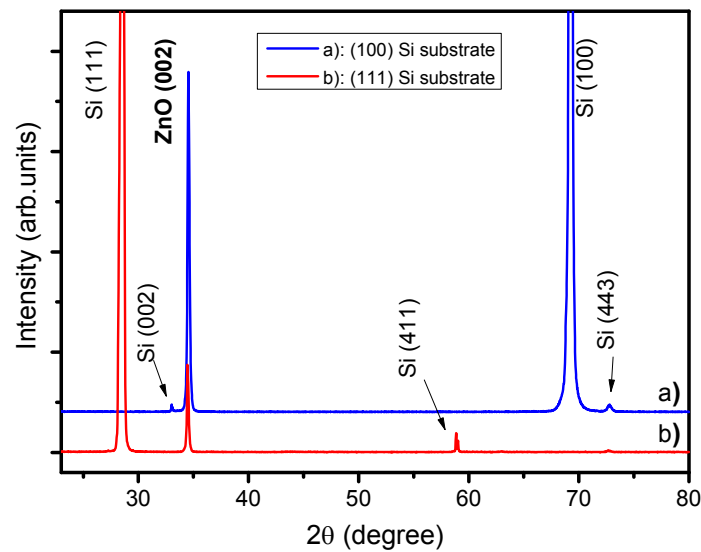


Figure 5.8: The XRD spectra of ZnO thin films on a): (100) Si substrates and b): (111) Si substrates grown by the type II vapor phase method

The low temperature PL spectra of the ZnO thin films grown by the type II vapor phase method are depicted in Figure 5.9(a). The broad excitonic emission at 3.367 eV is probably caused by the surface exciton recombination (SX), ionized donor (D^+X) or even the zinc interstitials [65, 107, 108, 150, 151]. The broad visible emission is centered at 1.9 eV (yellow color emission). DAP transition at 3.255 eV and its LO phonon replicas at lower energy position were observed. The nature of DAP transition was confirmed by the blue-shift of peak maximum position in the excitation power dependent PL spectra in Figure 5.9(b).

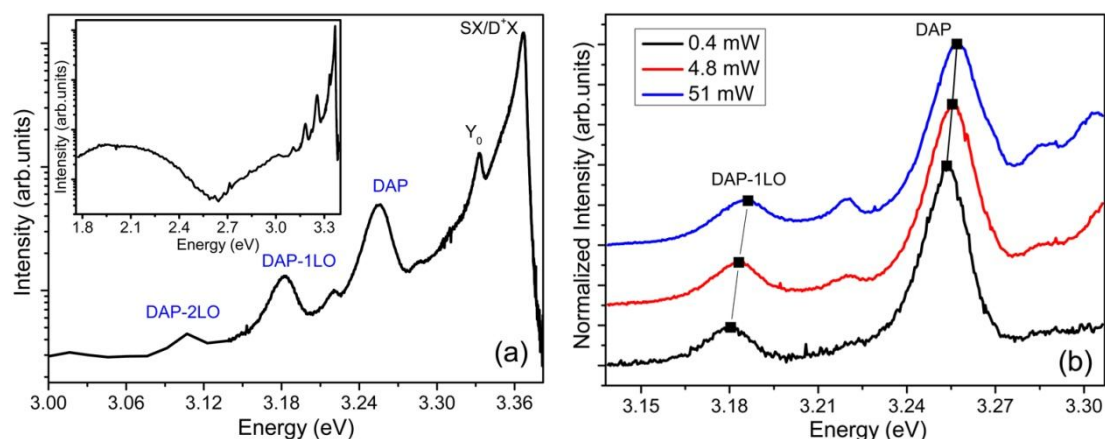


Figure 5.9: (a) The PL spectra of ZnO thin film on Si substrates grown by the type II vapor phase method, the insert shows the spectra of wider range from UV to visible; (b) The excitation dependent PL spectra in the range between 3.138 eV and 3.308 eV of the same sample.

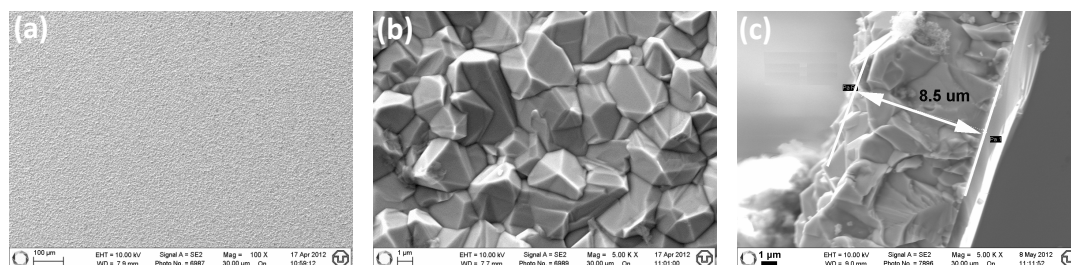


Figure 5.10: Typical SEM image of ZnO thin films on Si substrates grown by the type III vapor phase method, (b) is the enlargement of image (a), and (c) is the image of the cross-section

For the type III vapor phase method, continuous and uniform ZnO layers were

achieved on both (100) and (111) Si substrates. The surface morphologies of the layers are closely packed microcrystals with multifactes as shown in Figure 5.10(a-b). The thickness was measured to be 8.5 μm in the SEM as shown in Figure 5.10(c). The thickness of the deposited films could be adjusted by changing the growth duration.

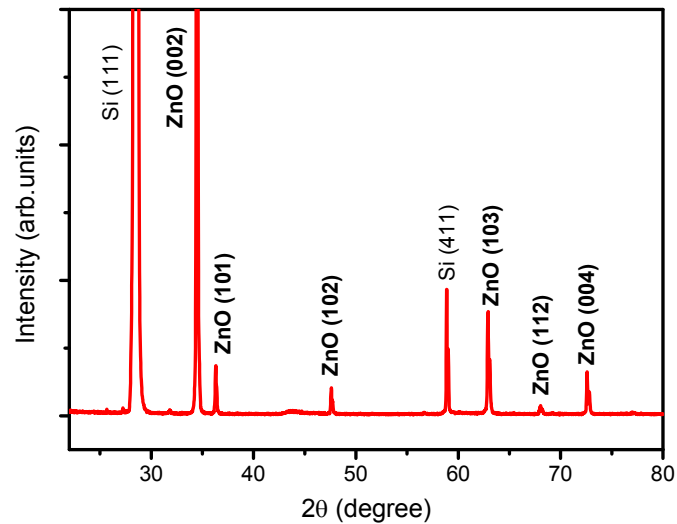


Figure 5.11: The XRD spectra of ZnO thin films on (111) Si substrates grown by the type III vapor phase method

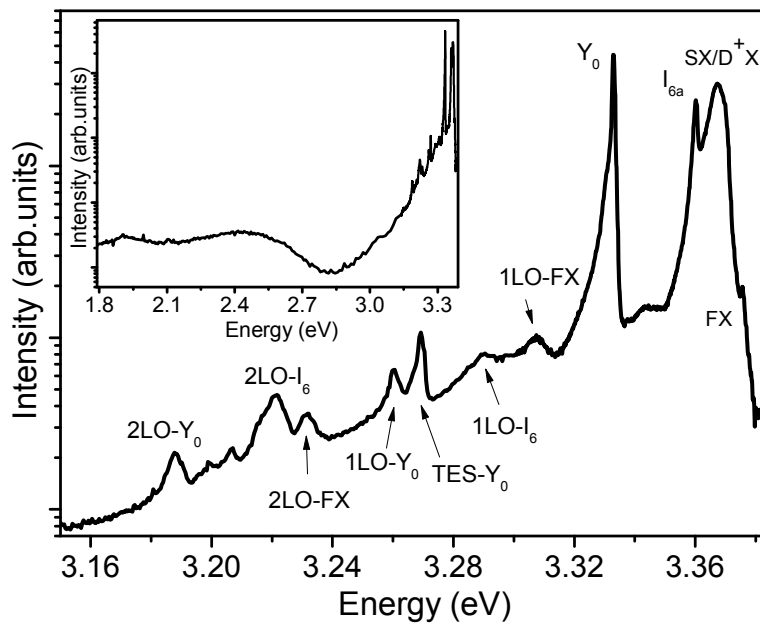


Figure 5.12: The PL spectra of ZnO thin film on Si substrates grown by the type III vapor phase method, the insert shows the spectra of wider range from UV to visible.

The XRD spectra in Figure 5.11 shows that the ZnO thin films on (111) Si substrates has the (002) preferential orientation. The low temperature PL spectra are depicted in Figure 5.12, the free exciton FX , and bound exciton I_{6a} were observed together with their LO phonon replicas. The intensity of Y_0 (bound structure exciton) was particularly high, which allowed the observation of the well-resolved TES transition (at 3.2698 eV) and LO phonon replica (at 3.2606 eV) of Y_0 line [103]. The broad visible bands centered in the yellow and green color region.

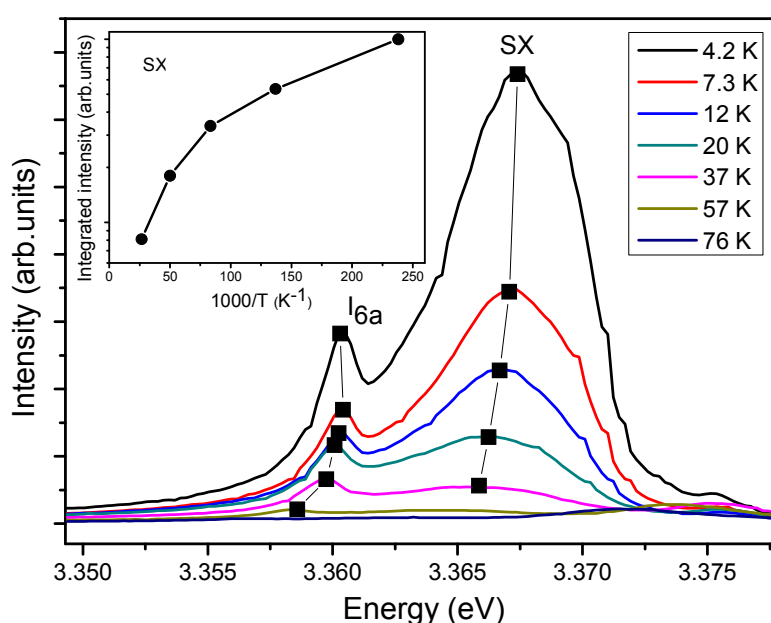


Figure 5.13: The temperature dependent PL spectra of the ZnO films grown by the type III vapor phase method at the bound excitonic range, the insert plots the integrated intensity of the 3.367 eV peak vs. $1000/T$, where T is the measurement temperature in Kelvin.

The broad peak at 3.367 eV is probably caused by the surface exciton (SX) recombination. The SX usually appears in nanostructure materials and depends on the surface-to-volume ratio [107, 108]. The temperature dependent behavior of the peak at 3.367 eV is shown in Figure 5.13.

5.4 DAP transitions in the as-grown films

The DAP transitions appeared in the ZnO thin films grown by the type II vapor

phase method without intentional doping. The nature of the DAP transition at 3.245 eV and its LO phonon replicas at lower energy positions was confirmed by the excitation power dependent PL spectra as shown in Figure 5.14. The excitation power changed from 0.12 mW to 48 mW, the corresponding DAP peak maximum shifted towards higher energy by about 11 meV. The position of DAP recombination (zero-phonon) is determined by equation (5.5):

$$\hbar\omega_{DAP} = E_g - (E_D + E_A) + \frac{e^2}{4\pi\epsilon\epsilon_0 R_{DA}} \quad \dots\dots\dots (5.5)$$

Where the R_{DA} in the Coulomb energy term is the effective distance of many discrete, well-defined distances between donors and acceptors. As discussed in Section 2.3.4, the largest R_{DA} and the lowest excitation power intensity will result in the smallest Coulomb attraction, and the energy position of corresponding DAP line is at the left edge (3.200 eV) of the broad peak, marked by a green cross in Figure 5.14. As a result, the addition of donor and acceptor ionization energy ($E_D + E_A$) is slightly smaller than 230 meV, assuming that the bandgap $E_g = 3.437$ eV at 4.2 K [11]. The free-to-bound

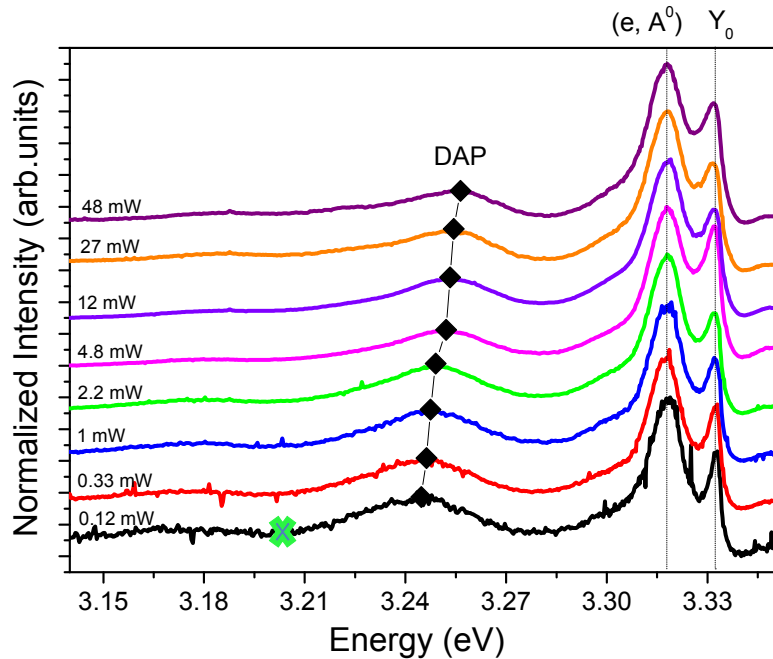


Figure 5.14: The excitation power dependent PL spectra of the as-grown ZnO thin films grown by the type II vapor phase method.

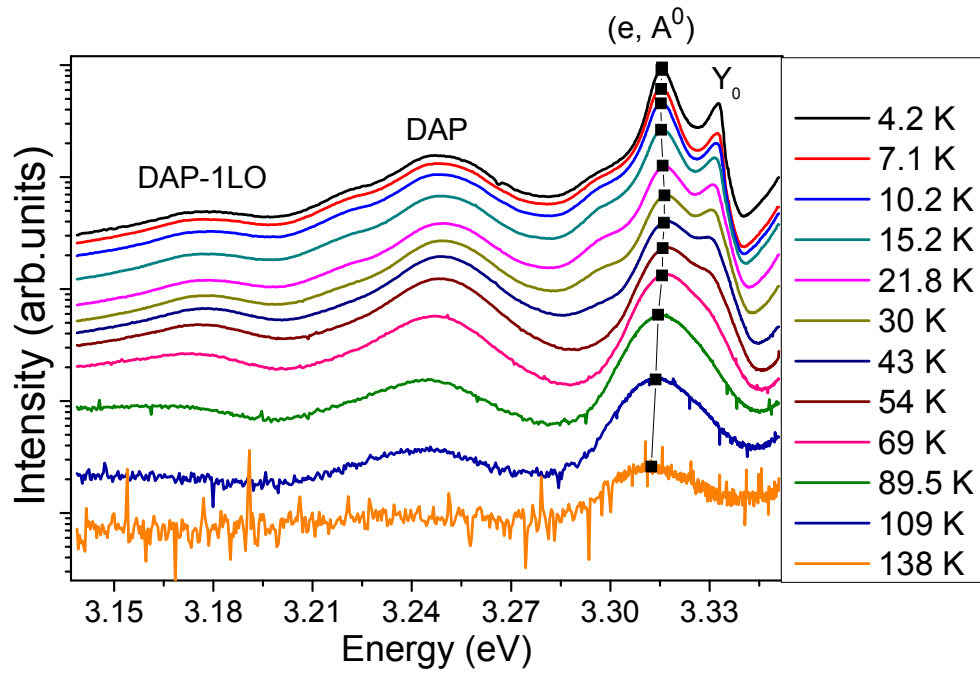


Figure 5.15: The temperature dependent PL spectra of the as-grown ZnO thin films grown by the type II vapor phase method.

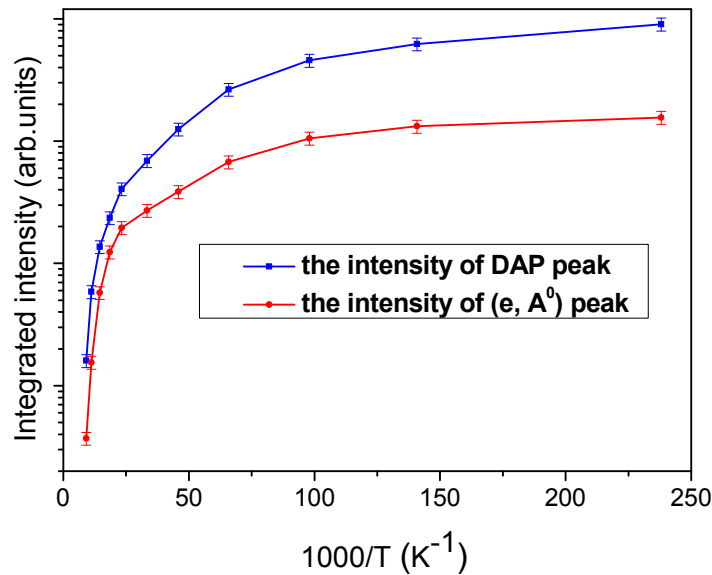


Figure 5.16: The integrated intensities of the DAP broad peak and the peak at 3.314 eV. vs. $1000/T$, where T is the measurement temperature in Kelvin.

transition (e, A^0) at 3.314 eV was suggested to account for the source of acceptor, which was originated from stacking faults [68]. To further investigate the DAP transition at 3.245 eV, the temperature dependent PL was measured from 4.2 K to 130 K, as shown in Figure 5.15. Correspondingly the integrated intensity of the DAP broad peak and the peak at 3.314 eV were plotted vs. $1000/T$ in Figure 5.16.

At higher temperatures, two curves have quite similar curvature, indicating the similar thermal dissociation energy. The acceptors in ZnO generally have larger binding energies than donors; the fitted thermal activation energy at higher temperatures should be related to acceptor species. That means that the acceptor in the DAP and the acceptor in (e, A^0) share the same thermal dissociation energy. In other words, the stacking faults related acceptor can account for the source of the observed DAP transition.

5.5 Discussion

In the type I vapor phase method, there are always some microcrystals on the surface of the uniform film because of the supersaturation of zinc vapor and relatively high growth temperatures. Immediately after the mixing of zinc vapor and O_2 gas, ZnO formed and nucleates on the substrate surface. 2D nucleation is the main mechanism and therefore uniform particle film forms on the silicon substrate. In the later period of the growth process, however, nucleation will still happen on the surface of the growing film due to the supersaturation of zinc vapor near the film surface, and they will grow to single crystals in micrometer scale (This is just the undesirable 3D nucleation.) due to the high growth temperature around 900 °C.

To ensure the reduction of ZnO source powders by incoming H_2 gas, the furnace temperature at around 900 °C cannot be greatly reduced. Furthermore, high furnace temperature leads to the formation of amorphous oxidized layer on the surface of Si substrates, which will reduce the quality of deposited film. In addition, high growth temperature is more inclined to induce thermal stress between the Si substrate and deposited film because of the large difference of thermal conductivity between silicon

and ZnO [6].

As a result, it's necessary to replace the source materials of ZnO powders by Zn powders, which can greatly reduce the growth temperature from 900 °C to around 670 °C, because lower temperatures are needed for the production of zinc vapor from metal Zn. That's the reason for shifting to the type II and III growth method. However, lower growth temperature could also lower down the crystallinity of as-grown films, that is probably the reason for the strong emission peaks originated from structural defects in the films by type III method.

Hydrogen is involved into the growth process in the form of H₂ gas or water vapor in the type I and III method, and there is no involvement of hydrogen in the type II method. The DAP transition appears only in the films grown by type II growth method is probably due to the lack of hydrogen compensation and hydrogen passivation of acceptors.

5.6 Conclusion

ZnO thin films were successfully deposited on Si substrates by open-system vapor phase method. Three different types of growth are employed: I) ZnO powders act as source material, Zn vapor is produced by the reductive reaction between H₂ gas and ZnO powders, O₂ gas acts as oxidizer; II) Zn powders act as source material, Zn vapor is produced by the thermal evaporation by metal Zn, O₂ gas acts as oxidizer; and III) Zn powders act as source material, Zn vapor is produced by the thermal evaporation by metal Zn, H₂O gas acts as weaker oxidizer. The type II and III methods with lower growth temperatures are easier to deposit homogenous ZnO films on Si substrate. The DAP transition at 3.245 eV and its phonon replicas are observed in the films grown by the hydrogen-free type II vapor phase method.

Chapter 6

Two unidentified PL emissions in vapor phase grown ZnO single crystals

Two unidentified PL emissions at 3.3643 eV and 3.3462 eV were observed in the vapor phase grown ZnO single crystals and hydrogenated crystals. The spectroscopic properties of these two emissions were studied and the possible origins are discussed in this chapter

6.1 Introduction

The low temperature photoluminescence (PL) from ZnO crystals has been extensively studied. More than ten different excitonic features are reported in the near-band-edge emissions. Part of these features have been unambiguously identified, such as I_4 (H), I_6 , I_{6a} (Al), I_8 (Ga) and I_9 (In), but there are still some controversies over the assignments of several transitions. In addition to the commonly known transition labeled as $I_0 - I_{11}$, two rarely reported [73, 103, 152] and unidentified emissions at 3.3643 eV and 3.3462 eV were observed in the vapor phase grown ZnO single crystals, the details of these two transitions will be shown in the following sections.

6.2 Details of the peak at 3.3643 eV

The investigated samples were ZnO single crystals grown by our vapor phase method using only Al₂O₃ tube, the growth is kept at 1300 °C for 20 h, and the gas flow rates of H₂, O₂ and N₂ are 8, 10, and 800 sccm respectively. In addition to the commonly observed I_6 , I_8 , I_9 transitions and their TES lines, a sharp PL emission at 3.3643 eV (labeled as P₁) is shown in Fig 6.1. P₁ is attributed to the recombination of an exciton bound to a shallow donor, due to the appearance of its TES lines [61]. Its

localization energy is 11.7 meV, the TES separation ($2P_z-1S$) is 29.4 meV, and the donor binding energy is 42.2 meV according to the Haynes rule [11, 153]. As discussed in Section 2.3.3, the splitting of the excited states of the donor into 2S and 2P states are usually observed. However, the 2S and 2P states in polar hexagonal semiconductors are additionally split into 2S, $2P_{xy}$ and $2P_z$ (where the hexagonal axis c is directed along z), because of the effects of anisotropy and the polar interaction with optical phonons [11, 51]. The three TES lines ($2S$, $2P_{xy}$ and $2P_z$) of the P_1 , as shown in Figure 6.2, were confirmed by comparing the spectra of several samples.

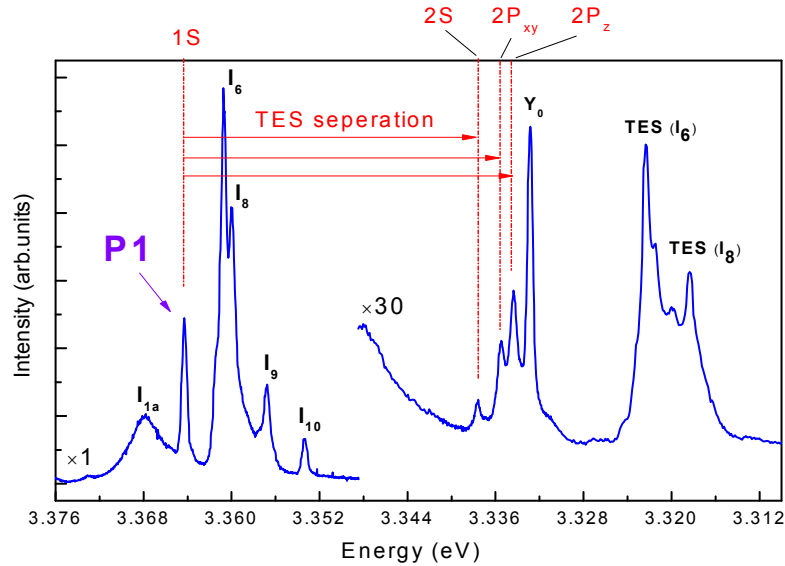


Figure 6.1: The PL spectra of an as-grown ZnO single crystal grown by vapor phase method, the spectra of the TES region was multiplied by a factor of 30 for better clarity.

B. K. Meyer et al. [11, 51] has proposed a linear relationship between the TES splitting values and the corresponding donor binding energy, by fitting the known shallow donors (I_4 , I_6 , I_9 and I_{10}). The splitting values of $2P_z - 2S$, $2P_{xy} - 2S$, $2P_{xy} - 2P_z$ vs. the donor binding energy are shown in Figure 6.2, the P_1 line and four others shallow donors are depicted in the figure according to their donor binding energies. Therefore, the TES splitting values of the P_1 line can be calculated from the fitted lines of B. K. Meyer, and are compared with our measured values in Table 6.1. The differences between calculated values and our measured values are due to the effects

of anisotropy in ZnO and the polar interaction with optical phonons, and the errors of the donor binding energy.

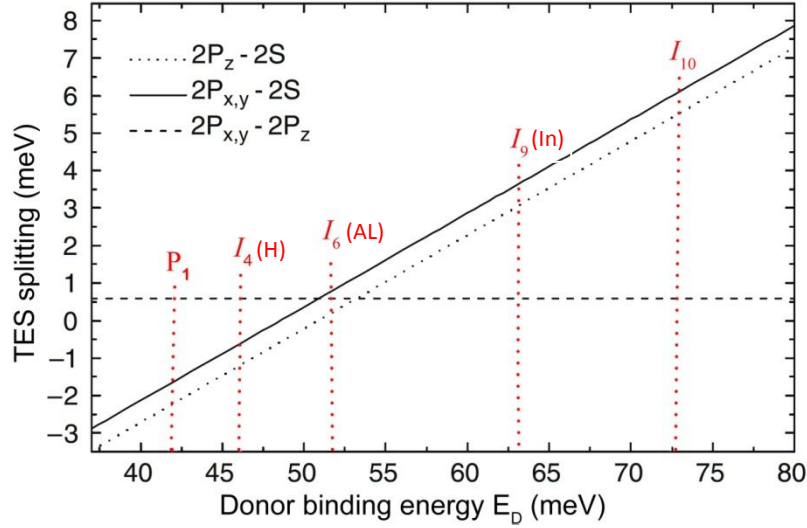


Figure 6.2: The linear relationship between the TES splitting and the corresponding donor binding energy [11], The P₁ line and four other shallow donors (*I*₄, *I*₆, *I*₉ and *I*₁₀) are depicted according to their donor binding energies.

Table 6.1: The TES splitting of the P₁ line at 3.3643 eV

Item	Estimated from Haynes' rule [11]	Our measured results
2P _{xy} - 2S	-1.7 meV	-2.1 meV
2P _z - 2S	-2.2 meV	-3.3 meV
2P _{xy} - 2P _z	+0.5 meV	+1.2 meV

The temperature dependent behavior of the P₁ line, as shown in Figure 6.3, is similar with that of *I*₆ and *I*₈. The intensity of P₁ emission is quenched when the temperature is above 40 K.

The defects accounting for the P₁ line are bulk defects, because the P₁ line can still be detected after the samples are etched in Orthophosphoric acid for 5 min. The defects are still stable in ZnO at 900 °C, as the P₁ line is still observable, as shown in Figure 6.4, when the samples are annealed in Ar atmosphere above 900 °C.

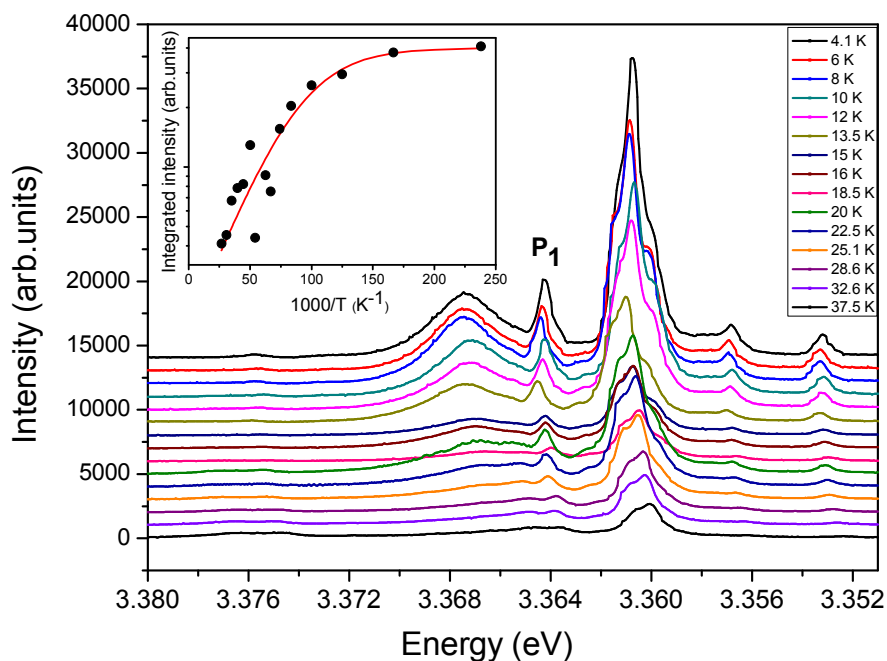


Figure 6.3: The temperature dependent PL spectra of the vapor phase grown ZnO crystals, and the insert shows the intensity of P1 line vs. the measurement temperature.

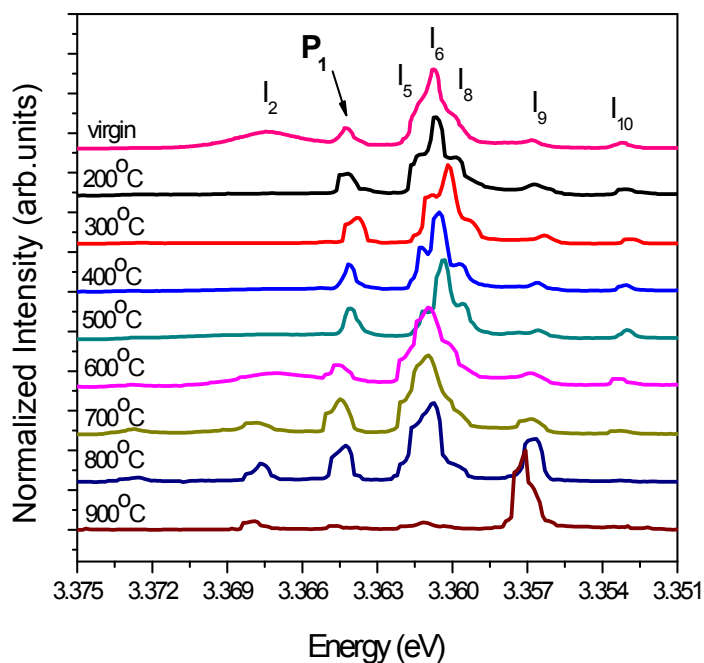


Figure 6.4: The PL spectra of ZnO crystal sample after annealing in Ar atmosphere at different temperature up to 900 °C.

6.3 Details of the peak at 3.3462 eV

The hydrogenation of the ZnO crystal was carried out by thermal annealing at 700 °C for 1 h in a silica ampoule filled with 0.5 atm hydrogen gas before sealing. The hydrogenation of the ZnO crystal leads to the appearance of the P₂ line at 3.3462 eV and a reduction of the P₁ line, as shown in Figure 6.5. In the hydrogenated sample, the Cu-related characteristic green band is also greatly depressed due to the passivation of the Cu deep acceptor by hydrogen [154].

Hydrogen in ZnO introduces two shallow donor levels: the one at 3.3628 eV, labeled as I₄, originates from substitutional hydrogen trapped within the oxygen vacancy; and the other at 3.3601 eV, labeled as H_{BC}, is due to interstitial hydrogen located at the bond-centered lattice site [86, 87]. The H_{BC} peak and its TES are observed after the hydrogenation.

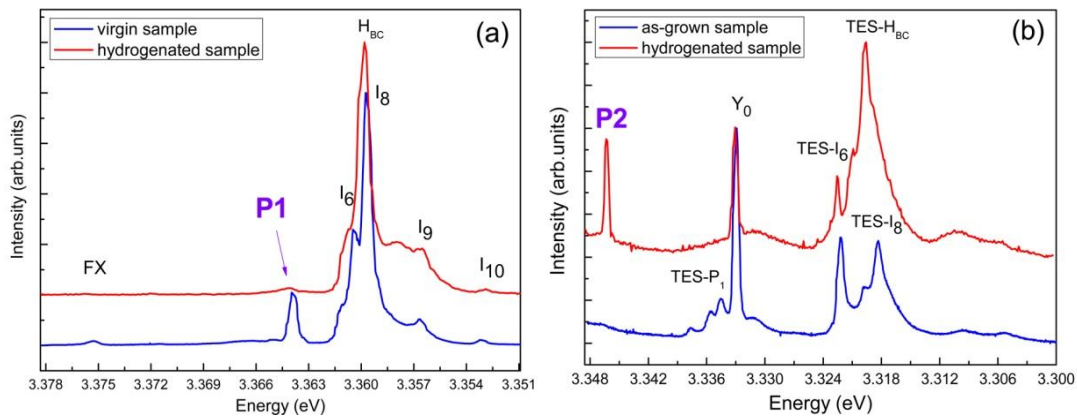


Figure 6.5: PL spectra of the hydrogenated (red curve) and as-grown (blue curve) ZnO crystal samples in the range of (a) 3.38~3.35 eV and (b) 3.35~3.30 eV.

The localization energy of P₂ transition is 29.8 meV [11], no TES transition is observed for P₂ line. Only if P₁ line appears in the virgin ZnO crystal sample, P₂ line could be detected in the PL spectra in the sample after hydrogenation.

6.4 Isochronal annealing after hydrogenation

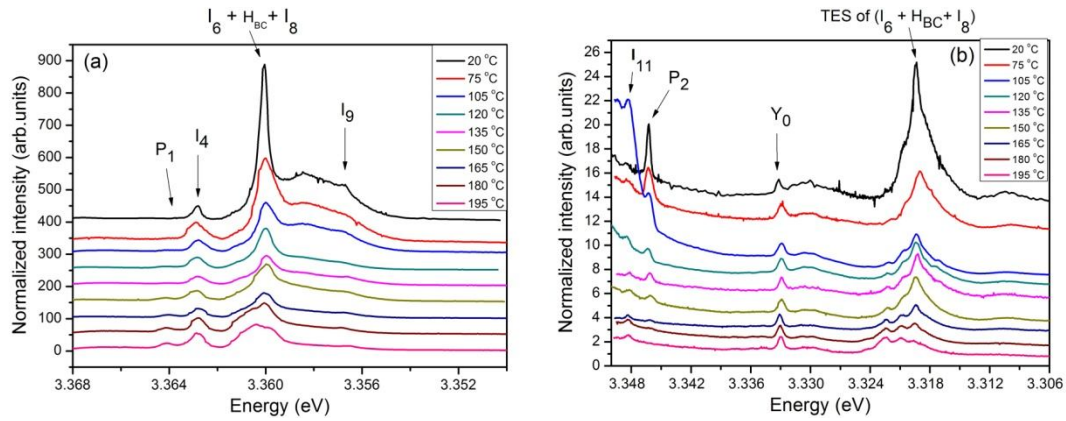


Figure 6.6: The PL spectra of the hydrogenated ZnO crystal sample after annealing at different temperatures from 75 °C to 195 °C (a) at the bound exciton range and (b) at the TES region.

The isochronal annealing series were carried out on the hydrogenated ZnO samples in ambient atmosphere for 30 min at different temperatures from 75 °C to 195 °C. The low temperature PL spectra of treated samples are shown in Figure 6.6. The spectra are normalized to the intensity of the Y_0 line. It is found that the Y_0 line has constant emission intensity when the sample is annealed below 200 °C. With the increase of annealing temperature, the P_2 line gradually weakens and disappears at around 200 °C. Conversely, the P_1 line reappears at around 120 °C and enhances with increasing temperature.

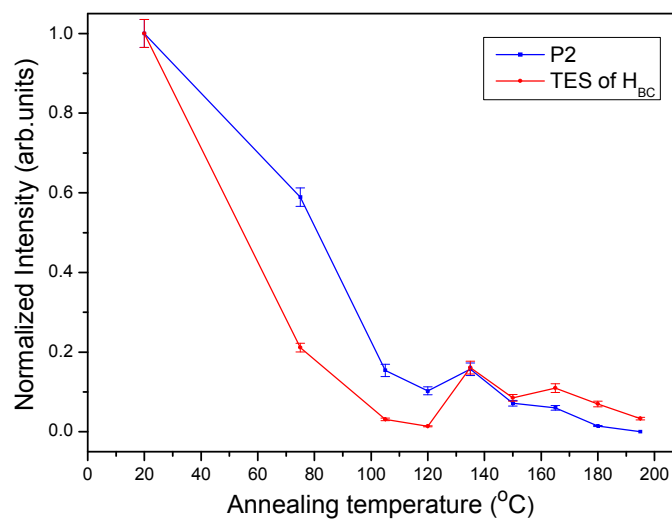


Figure 6.7: The normalized intensity of the P_2 line and the TES of H_{BC} line at different annealing temperatures

If we compare the intensity of the P_2 line and the intensity of the TES- H_{BC} in Figure 6.6(b), they show almost similar temperature dependence, as depicted in Figure 6.7.

6.5 Possible microscopic origins of the peak at 3.3643 eV and 3.3462 eV

There are very few reports about emission peaks in ZnO with similar energy positions of P_1 and P_2 line. The same transition could show small shift (several meV) of energy position in different samples because of the strain [155, 156].

Sann et al. [150] reported a 3.366 eV emission in ZnO powders and assigned it to interstitial Zn (Zn_i). However, the interstitial Zn has a quite low migration barrier (0.55 eV) [42, 151], and it's not stable at room temperature. Therefore, it cannot account for the reappearance of the P_1 line at 3.3643 eV after annealing above 120 °C.

Brandt et al. [152] observed a transition at 3.3465 eV (labeled as I_{12}) in ZnO thin films grown on a MgO or on a heavily aluminum-doped ZnO buffer layer with a distorted lattice. The recombination was determined to be an exciton bound to a neutral donor. Wagner et al. [103] found an emission at 3.3465 eV (labeled as Y_2) in Cermet melt grown ZnO wafer and assigned it to an excitonic recombination at extended structural defects with a distorted lattice structures. However, the structural defects model of the P_2 line cannot well explain the phenomena that, P_2 will be observed after hydrogenation, only if P_1 appears in the virgin sample.

Mendelsberg et al. [62, 73] observed two emissions at 3.365 eV and 3.348 eV and their TES transitions in Pb-implanted ZnO crystal, interstitial Pb and substitutional Pb on Zn site were proposed as origin of the two transitions. However, when considering the relatively large size, substitutional Pb impurities would not be able to move during the annealing below 200 °C, which cannot explain the PL intensities' reduction of P_2 line during the isochronal annealing process,

The microscopic nature of the P_1 line at 3.3643 eV and P_2 line at 3.3462 eV remains unclear. Tentatively, interstitial Pb may account for the P_1 line, because Pb is a trace impurity in the ZnO source material, and the interstitial Pb has smaller

formation energy than substitutional Pb in ZnO. Since the P₂ line and the H_{BC} line show a similar annealing temperature dependent behavior, a lead-hydrogen complex maybe the origin of the P₂ line. Hydrogenation makes the transformation of part interstitial Pb into Lead-hydrogen complex, and subsequent annealing makes the dissociation of Lead-hydrogen complex into interstitial Pb. Thermal diffusion of Pb into hydrothermally grown ZnO crystals does not result in the appearance of the P₁ line, however, our thermal diffusion of Pb at higher temperatures were not successful.

6.6 Conclusion

Two PL emission lines (P₁ at 3.3643 eV and P₂ at 3.3462 eV) are observed in our vapor phase grown ZnO single crystals. P₁ is attributed to the recombination of an exciton bound to a shallow donor with binding energy of 42.2 meV. Hydrogenation of the as-grown ZnO single crystal leads to the appearance of the P₂ line and a great reduction of P₁ line. Subsequent isochronal annealing in the ambient atmosphere leads to gradual reduction of P₂ and the reappearance of P₁. Hydrogen is supposed to be involved in the defect which is responsible for the P₂ line.

Chapter 7

Attempts for p-type doping in ZnO

In this chapter, the causes, progresses and strategies of the long standing p-type doping problem in ZnO will be summarized. The attempts for p-type doping by nitrogen and antimony will be outlined and experimentally tried.

7.1 Status of p-type doping in ZnO

The difficulty in achieving conductivity of both n- and p-type is still a major obstacle for ZnO and other wide bandgap semiconductors such as GaN, ZnS, ZnSe and ZnTe [6]. Wurtzite ZnO is a natural n-type semiconductor mainly because of the unintentionally incorporated and always-existing background impurities (such as H, Al, In and Ga) [11]. Free electron concentration beyond 10^{20} cm^{-3} is easy to achieve in ZnO [6]. However, even after half century's efforts, p-type doping is still a challenging topic in the field of ZnO research and applications.

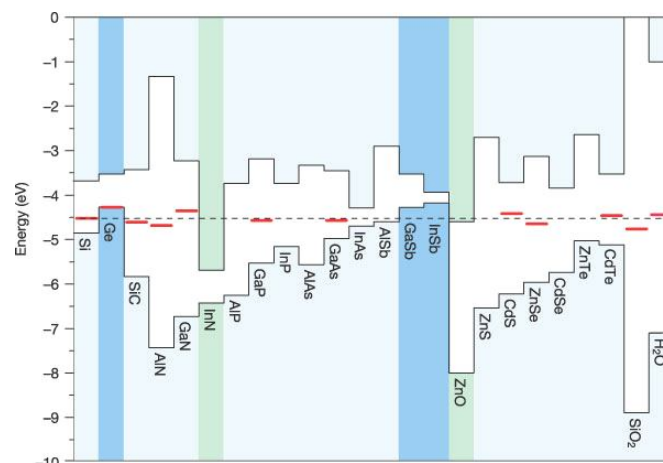


Figure 7.1: The alignment of the valence band maximum (VBM) and the conduction band minimum (CBM) of various semiconductors including ZnO, the dashed line indicates the universal level of hydrogen at the absolute energy scale [157].

The band alignment of ZnO and other semiconductors are shown in Figure 7.1,

obviously, the valence band maximum (VBM) of ZnO is low (about -8 eV) at the absolute energy scale [157]. The electron workfunctions of most elements lie in the range of 2 eV ~ 6 eV [158]. These two factors mean that, the electronic transition levels of most elements will be far from the VBM of ZnO, which determines the difficulty in achieving shallow acceptor levels in the band gap of ZnO [13].

In the last decade, the acceptor dopants were proposed from the group I (including IB) and group V elements. The group I elements (such as Li, Na) and group IB elements (such as Ag) substituting on Zn sites, or the group V elements (such as N, P, As, Sb) substituting on O sites are supposed to act as shallow acceptors. Especially N [159] and Li [160] are the most frequently adopted dopants because of the similar ionic radii to their substituting atom. Several “observed” p-type doped ZnO are reported and summarized in Table 7.1

Table 7.1: Summary of successful attempts to grow p-type doped ZnO [161]

Dopant	technique	$N_A(\text{cm}^{-3})$	type	$\mu(\text{cm}^2/\text{Vs})$	$P(\text{Ohm cm})$	Reference
N	CVD	1.06×10^{18}	<i>p</i>	0.34	17.3	[162]
P	Diffusion	-	<i>p</i>	-	-	[163]
P	Sputtering	$1.9 \times 10^{16} \sim 3.8 \times 10^{19}$	<i>p</i>	6.9~40.1	0.02~8.1	[164]
As	PLD	$10^{18} \sim 10^{21}$	<i>p</i>	0.1~50	$10^{-5} \sim 10$	[165]
As	Sputtering	9×10^{19}	<i>p</i>	4	-	[166]
As	PLD	$2.4 \times 10^{17} \sim 1.1 \times 10^{18}$	<i>p</i>	-	2.2~6.7	[167]
As	CVD	1.45×10^{18}	<i>p</i>	1.92	2.3	[168]
As	PLD	4×10^{19}	<i>p</i>	2	0.05	[169]
Sb	MBE	1×10^{16}	<i>p</i>	10	6	[170]
Sb	PLD	1.9×10^{17}	<i>p</i>	7.7	4.2	[171]
Li	PLD	6.04×10^{17}	<i>p</i>	1.75	5.9	[172]
N+Al	Sputtering	2.52×10^{17}	<i>p</i>	0.43	57.3	[173]
N+Al	Sputtering	1.45×10^{18}	<i>p</i>	1.62	2.64	[174]
N	PLD	-	<i>p</i>	8	-	[175]
Ag	PLD	$4.9 \times 10^{16} \sim 6.0 \times 10^{17}$	<i>p</i>	0.29~2.32	34~54	[176]
Na	CVD	10^{20}	<i>p</i>	2.1	-	[95]

Group I elements: Li [93, 177] introduces both donor and acceptor to ZnO. Interstitial Li_i is a deep donor at $E_V + 2.0$ eV and substitutional Li_{Zn} is a deep acceptor

at $E_V + 0.2$ eV [92]. The preferable form of Li defect is strongly dependent on the growth condition and Fermi level. Li_{Zn} is less stable than Li_i in the natural n-type ZnO. Interstitial Li_i and substitutional Li_{Zn} can compensate each other, which leads to the semi-insulating conductivity of hydrothermal ZnO crystals, although high concentration of Li up to 10^{17}cm^{-3} is reported. In addition, Li_{Zn} can be easily passivated by forming highly stable $\text{Li}_{\text{Zn}}\text{-H}$ complexes [92].

Na shows a similar behavior as Li [92]: Interstitial Na_i is a deep donor at $E_V + 1.9$ eV, and substitutional Na_{Zn} is a deep acceptor at $E_V + 0.3$ eV. Liu et al. [95] report on Na-doped p-type ZnO microwires using chemical vapor deposition (CVD). The p-type ZnO microwires were grown by a vapor-liquid-solid process from a mixture of zinc powder, graphite powder, and NaCl. However the reproducibility of the samples is doubted without further reports.

Group V elements: Nitrogen is the most reported acceptor doping because of the abundance of nitrogen chemicals in gaseous state. After years' of investigations, substitutional nitrogen on oxygen sites (N_O) is found to be a deep acceptor and hence cannot lead to hole conductivity in ZnO [98, 178]. Lyons et al. performed a

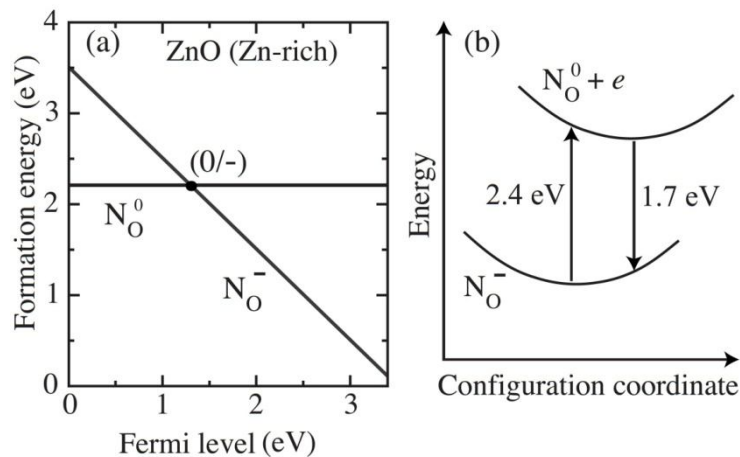


Figure 7.2: (a) Formation energy as a function of Fermi level E_F for N_O in ZnO under Zn-rich conditions. E_F is referenced to the VBM, and the position of the (0/-) acceptor level is indicated. (b) Configuration coordinate diagram indicating optical absorption and emission energies for exchanging an electron with the conduction band [98].

first-principles calculation on N in ZnO using hybrid functions [98]. The formation energy as a function of Fermi level E_F for N_O in ZnO under Zn-rich conditions is shown in Figure 7.2(a) and the Fermi level E_F is referenced to the VBM. From the calculation N_O can be stable in either the neutral or -1 charge states, with the acceptor level (0/-1) occurring at 1.3 eV above the VBM. N_O is therefore a deep acceptor in ZnO. The formation energy of substitutional N_O is quite small; since the as-grown ZnO samples are usually n-type and the Fermi level is close to the CBM.

In order to investigate the optical transitions, the configuration coordinate diagram of N_O was mapped in 7.2(b). Taking into account that the photons will be absorbed or emitted in vertical transitions (no change in atomic positions, because there is not enough time for fully lattice relaxation), the Frank-Condon shift between the absorption and emission lines is 0.7 eV, and the optical absorption and emission energies for exchanging an electron with the conduction band are 2.4 eV and 1.7 eV respectively. This was experimentally checked by photoluminescence [12, 179].

The solubility of nitrogen in ZnO is usually $10^{16}\sim 10^{18} \text{ cm}^{-3}$, which is too low to achieve hole concentration above 10^{19} cm^{-3} . Elevating the growth temperature is one way to enhance the solubility. However, N_2 molecule will form at elevated temperatures. Theoretical calculations point out that, N_2 molecule leads to localized states in the band gap either by forming an N_2O molecule or by breaking a Zn-O bond [180]. Nitrogen molecule will form from two interstitial nitrogen atoms, and interstitial oxygen facilitates the formation of N_2 by kicking out N_O to the interstitial sites [181]. The formation of nitrogen molecule in ZnO will cause low doping efficiency and degeneration of the p-type conductivity.

Substitutional nitrogen on oxygen site N_O can be easily passivated by forming $N_O\text{-H}$ complex which is thermally stable up to 700 °C [91, 182]. However, high temperature dehydrogenation is possible to dissociate the $N_O\text{-H}$ complex and realize nitrogen-doped p-type ZnO [183].

Other elements of group V (P, As, Sb) substituting on O sites are also deep acceptors because of the larger ionic radii and resulted larger lattice distortion [13].

Li_{Zn} and N_O candidates are deep acceptors in ZnO and do not contribute to the hole

conductivity. Several complexes including Li_{Zn} or N_{O} are proposed to form shallow acceptor level in the bandgap by theory, such as $\text{Li}_{\text{Zn}}\text{-N}_{\text{O}}$ [14], $\text{X}_{\text{Zn}}\text{-2V}_{\text{Zn}}$ ($\text{X} = \text{P}, \text{As}, \text{Sb}$) [15, 184].

In experimental characterization, inhomogeneous impurity incorporation makes the determination of the conductivity type via Hall Effect difficult and unreliable. Grain boundaries, surface conduction [185], impurities segregation and even the formation of 2D electron gas at the film/foreign substrate interface can introduce additional conduction channels [13]. The p-type conductivity may appear in isolated small domains inside the sample, such as N_{O} -induced hole conductivity in grain boundaries reported by Szyszka et al. [106].

To overcome above-mentioned problems, several strategies are proposed, such as codoping, pulse annealing, and non-equilibrium process.

Codoping: codoping is an approach that incorporates the desired acceptor defect together with a donor impurity, the donor impurity shifts the Fermi level away from

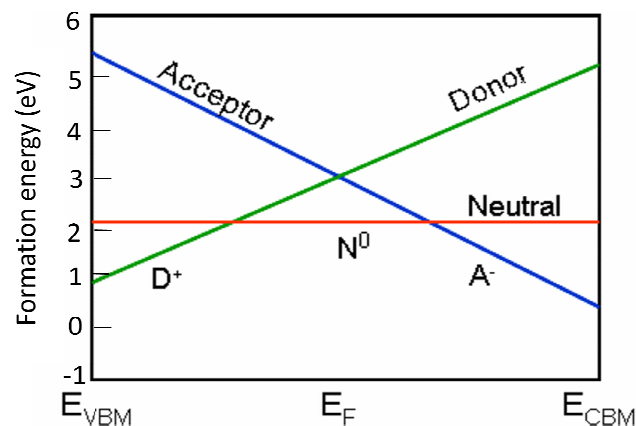


Figure 7.3: Schematic dependence of the formation energy of charged defects on the Fermi energy position [186].

the VBM towards the middle of the band gap. This results in a reduction of the acceptor formation energy and therefore enhances the acceptor solubility, as shown in Figure 7.3 [186]. The donor impurity can be removed by subsequent thermal annealing [183, 187].

Enhancement of the chemical potential of dopants: The doping efficiency of dopants can be enhanced by increasing the chemical activity of dopants. For example, NO, NO₂ and N₂O compounds have a higher N chemical activity than N₂ gas [188-191]. When the N₂ molecules are excited by plasma, the N chemical potential could be increased by as much as 1.5 eV [192]. Higher chemical potential is favored to lower formation energy and higher concentration of acceptor defects [77].

Non-equilibrium process: The incorporation of foreign impurities could be controlled by kinetics [193]. Therefore, non-equilibrium process, such as pulse annealing [194], is expected to get higher concentration of acceptor dopants.

Cluster doping: First-principles calculations on p-type doping of ZnO reveal that successful doping depends on a stable local chemical bonding [195]. A cluster-doping approach, in which a locally stable chemical environment is realized by involving few defects species and defects complexes, is expected to create shallow acceptor levels [196, 197].

Strain tuning: The preference of substitutional and interstitial incorporation can be tuned through external strain, either hydrostatic or piezoelectric. Doping induces a volume change around the dopant. When an external strain is applied in the same direction as the volume change, the solubility will be enhanced. Take Li for example, the acceptor defects Li_{Zn} in ZnO can be enhanced against the donor defects Li_i under a external strain in a suitable direction [198].

7.2 Own attempts for p-type doping by nitrogen

7.2.1 Nitrogen doping from DC plasma

The diffusion of nitrogen into ZnO was carried under the irradiation of N₂ DC plasma. The samples are vapor phase grown ZnO single crystals doped with lithium. The virgin ZnO crystal is subjected to 2 steps of treatments before N diffusion: i) annealing in flowing Ar at 600 °C for 2 h to remove the background hydrogen as much as possible and to lower down the Fermi level towards valence band; ii)

annealing in a sealed ampoule filled with 0.5 bar Ar at 600 °C for 2 h to create oxygen vacancies near the surface region (~1 μm in thickness). Mixture of N₂ and O₂ gas with volume ratio 1:2 instead of single N₂ gas was used as N source, because certain fractions (67 vol.%) of O₂ could enhance the radical N⁺ in the plasma [199, 200]. The ZnO sample is kept at 300 °C in the N plasma for 30 min as described in the section 3.3 of the chapter 3. The sample temperature is chosen to be 300 °C for two reasons: i) the temperature should be a little bit higher to enhance the diffusion of nitrogen; ii)

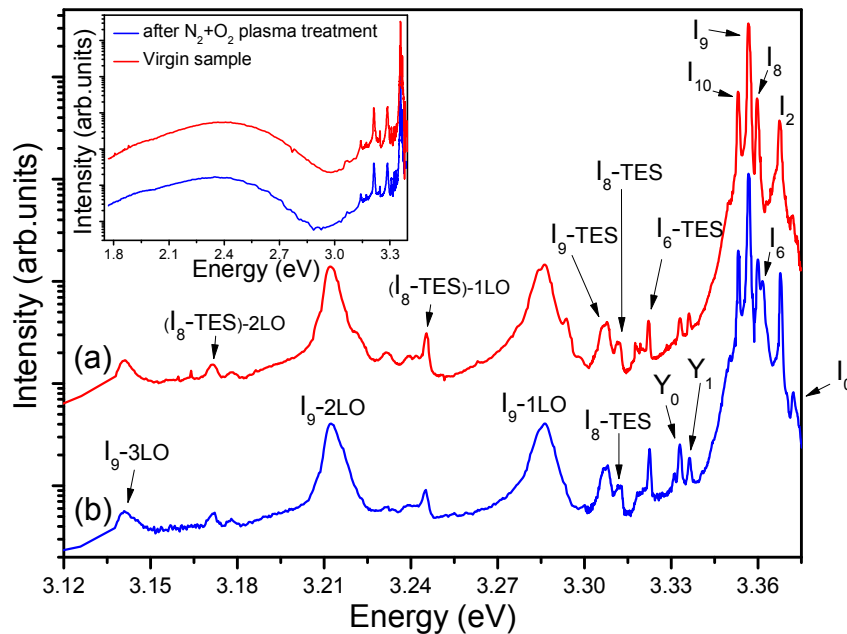


Figure 7.4: The PL spectra of the ZnO crystal sample (a) virgin sample and (b) sample after the N₂ DC plasma treatment at 300 °C, the insert shows wider range of spectra of both samples.

but a lower temperature should be chosen to avoid the formation of N₂ molecules. The low temperature PL spectra of the ZnO sample before and after the N plasma treatment are shown in Figure 7.4. Both spectra are dominated by I₂ (ionized In donor), I₆ (Al), I₈ (Ga), I₉ (In), I₁₀, and their TES and LO phonon replicas. Actually the two spectra show almost the same features, except the peak at 3.294 eV. It is not related to nitrogen because the peak at 3.294 eV disappears after the N plasma treatment. D. C. Look et al. [201] has assigned the peak at 3.317 eV to the emission of an acceptor-bound exciton (A⁰X), which is associated with the substitutional nitrogen.

However, the peak at 3.317 eV and its LO phonon replicas at 3.245 eV and 3.172 eV in our samples seems to be not related to nitrogen, because these peaks frequently appear in our vapor phase grown ZnO crystals without any nitrogen treatments. They are more likely to be the TES of $I_8(\text{Ga})$ and corresponding LO phonon replicas. There is no appearance of peaks at 3.311 eV and 3.346 eV related to the shallow acceptor defect of $\text{Li}_{\text{Zn}}\text{-N}_\text{O}$ [14].

7.2.2 Nitrogen doping from RF plasma

Since RF plasma has higher power intensity than general DC plasma, it's possible to diffuse higher concentration of nitrogen into ZnO crystals. The samples are commercial hydrothermal ZnO single crystals (Mateck GmbH) cut from one 10×10 mm wafer. The virgin ZnO crystals are subjected to 2 steps of treatments before N diffusion: i) annealing in flowing Ar at 600 °C for 2 h to remove the background hydrogen as much as possible and to lower down the Fermi level towards valence band; ii) annealing in a sealed ampoule filled with 0.5 bar Ar at 600 °C for 2 h to create oxygen vacancies near the surface region ($\sim 1 \mu\text{m}$ in thickness). N_2 RF plasma and N_2O RF plasma were employed for the nitrogen diffusion as described in the section 3.3 of the chapter 3. The N_2 RF plasma was produced with a RF power intensity of 80 mW/cm^2 . The chamber pressure was kept at 0.2 mbar. The ZnO sample was heated at 150 °C for 30 min and kept at a distance of 60 cm to the plasma source. The N_2O RF plasma was produced with a RF power intensity of 32 mW/cm^2 . The chamber pressure was kept at 0.2 mbar. The ZnO sample was heated at 200 °C for 30 min and kept at a distance of 30 cm to the plasma source. No obvious changes before and after the N diffusion were observed in the PL spectra excited by 325 nm He-Cd laser.

Below band gap excitation photoluminescence by 514.5 nm (2.4098 eV) Ar laser was recorded to check the deep acceptor emission of substitutional N_O . The emission peak is located at 730 nm (1.7 eV) according the N_O model proposed by Lyons et al. [98].

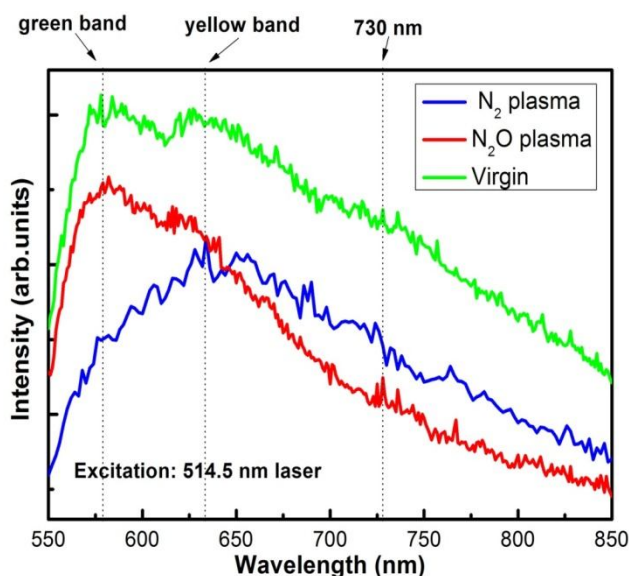


Figure 7.5: The below band gap excitation PL spectra of the ZnO crystal sample (a) virgin, (b) after the N_2 RF plasma treatment at $150^\circ C$, (c) after the N_2O RF plasma treatment at $200^\circ C$.

However, no emission peaks at 730 nm were observed in the below band gap excitation PL spectra, except the common green band at 550 nm and yellow band at 630 nm, as shown in Figure 7.5. The absence of peak at 730 nm is attributed to low efficiency of nitrogen introduction [13] and the formation of N_2 molecules [180, 181].

7.3 Our attempts for p-type doping by antimony

Although the substitutional defect Sb_O is a deep acceptor because of the large radii of antimony atom, the defect complex $Sb_{Zn}-2V_{Zn}$ was proposed by calculations to introduce a shallow acceptor level in the band gap [15].

The antimony doping was conducted by the type II vapor phase growth of ZnO films on Si substrate as described in chapter 5. The Sb metal powders (Chempur GmbH, 99.9999%) were mixed into the source material (Zn powders), and three different molar ratios (5, 15 and 30) between Zn and Sb were selected. The films were deposited onto (100) Si substrate at $650^\circ C$ for 2 h. The SEM images are shown in Figure 7.6. The ZnO films are composed of microrods, which have a diameter of about 200~300 nm. At larger Sb concentrations, these microrods have smooth

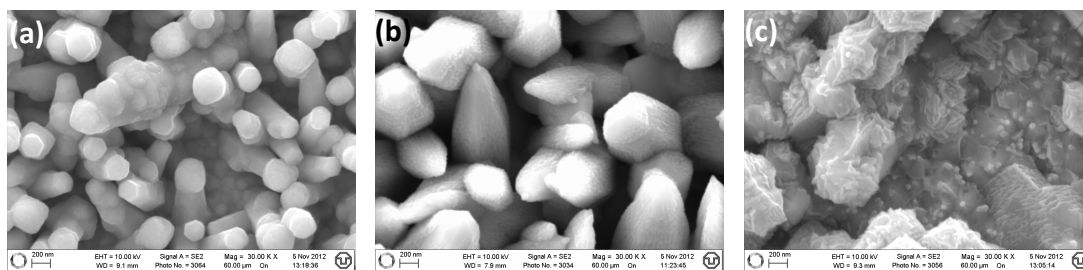


Figure 7.6: The SEM images of Sb doped ZnO films by the type II vapor phase method with different molar ratio between Zn and Sb: (a) 5, (b) 15, and (c) 30.

surfaces; and at smaller Sb concentrations, these microrods are covered by much smaller crystals.

The PL spectra of Sb-doped ZnO films grown from different Zn:Sb ratios are depicted in Figure 7.7, the spectra of three samples share the same features in the

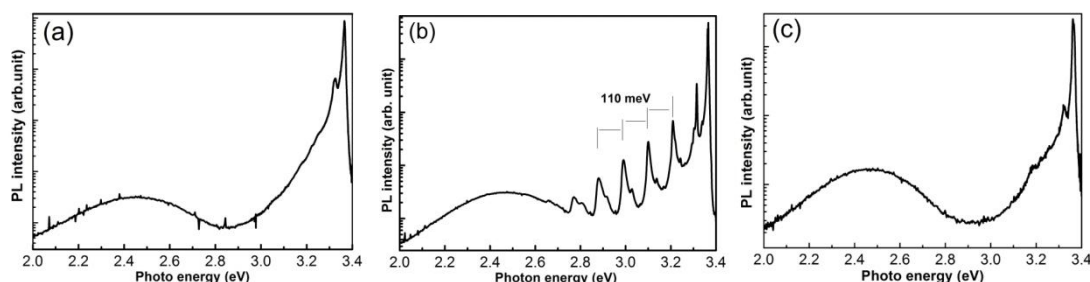


Figure 7.7: The PL spectra of Sb doped ZnO films by the type II vapor phase method with different molar ratio between Zn and Sb: (a) 5, (b) 15, and (c) 30.

bound excitonic range and the visible emission. However, the sample grown from medium Zn:Sb ratio shows different features from the others, where uniformly-spaced peaks appear with energy separation of 110 meV. The strong coupling could be the whispering gallery modes in ZnO microrods, which are microsized resonators with hexagonal cross section [202, 203]. It seems that these uniform-spacing peaks are not related to antimony.

The absence of PL peaks of the expected shallow acceptors ($Li_{Zn}-N_O$ and $Sb_{Zn}-2V_{Zn}$) needs further investigations. Reasons could be the low efficiency of introducing desired defects; or the compensation by background donors, such as Al, In, and Ga.

Since the hole effective mass is 2~3 times larger than the electron effective mass in ZnO [18], the acceptor ionization energy will be also 2~3 time larger than the donor ionization energy for shallow impurities, according to the effective mass approximation [59]. The shallow donor ionization energies are typically 46~72 meV [11], therefore the acceptor will be above 150 meV, which is too deep to provide free holes. This estimation is quite rough, but it gives one reason of the difficulty of p-type doping in ZnO.

The difficulties can also be explained in terms of the amphoteric defect model (ADM) by Walukiewicz et al. [204]. It is shown that the maximum free electron or hole concentration that can be achieved by doping is an intrinsic property of a given semiconductor and is fully determined by the location of the band edges with respect to a common energy reference, the Fermi level stabilization energy. It has been found that for sufficiently high damage density (gamma rays or electrons), the Fermi energy stabilizes at a certain energy and become insensitive to further damage. The location of this Fermi level stabilization energy E_{FS} does not depend on the type or doping level of the original material and therefore is considered to be an intrinsic property of a give material. For II-VI semiconductors, the Fermi level stabilization energy E_{FS} is located at about 4.9 eV below the vacuum level. The conduction band edge of ZnO is located very close to E_{FS} at $E_{FS} + 0.2$ eV, while the valence band edges of ZnO lies at the very low energy of $E_{FS} - 3.1$ eV. Such an alignment strongly favors n-type conductivity and leads to tremendous difficulties for p-type doping of ZnO.

7.4 Conclusion

The long-standing challenge of p-type doping in ZnO is mainly attributed to the spontaneous formation of compensating defects and the lack of appropriate acceptors with small ionization energy. The present status and proposed strategies of the p-type doping were reviewed and discussed. Two attempts for the p-type doping of ZnO were carried out by diffusing plasma-activated nitrogen into ZnO crystals after the growth and by doping antimony to ZnO films during the growth, although no

conclusive hole conductivity was detected in the doped samples.

Chapter 8

Outlook

In the present thesis, needle-shaped ZnO single crystals and homogenous ZnO films on Si substrates were successfully grown by employing a low cost and open-system vapor phase technique. Two unidentified PL emissions at 3.364 eV and 3.346 eV from the as-grown needle crystals were studied. The origins and status of long standing problem with p-type doping were explicitly analyzed, two attempts for the p-type doping were performed by post-growth diffusing plasma-activated nitrogen into ZnO needle crystals and by *in-situ* doping of antimony during the growth of ZnO films. Throughout the thesis, there are several aspects which deserve further investigations:

The control of nucleation, especially the prevention of spontaneous nucleation, in the vapor phase process is important for the growth of ZnO single crystals and ZnO thin films. Spontaneous nucleation introduced several problems: high densities of needle crystal clusters, dendritic crystals in the single crystal growth, and the surface microcrystals in the thin film deposition. These problems seriously hinder the improvement of the quality of ZnO single crystals and thin films. The promising approaches for better control of the vapor phase processes would be numerical simulation of the thermodynamics of growth, and careful adjustment of the supersaturation of zinc vapors.

In this thesis, all the vapor phase growth is carried out at atmospheric pressure. However, reduced pressures tend to reduce unwanted gas-phase reactions and improve film uniformity across the Si wafer; sub-atmospheric pressure can also lower down the growth rate of single crystals and lead to an improvement of the crystallinity. Low pressure vapor phase growth should be performed in later research.

The as-grown ZnO single crystals in our growth show only one typical morphology: needle shape. This is the typical anisotropic character of ZnO which has a preferential growth. The growth rates of the ZnO crystal in c-axis direction and in perpendicular

direction differ up to 100 times, measured by comparing the length and diameter of the needle crystals. Some impurity defects can regulate the growth rate in different crystal directions and influence the shape of the final crystals [145]. Impurities should be taken into account for the adjustment of crystal size and shapes.

Lead (Pb) exists in the source material (ZnO pellets and Zn powders) with a concentration of 10 ppm, Pb atoms could be the possible microscopic origin of the PL emission at 3.3643 eV. Pb implantations into the ZnO single crystal and thin films are necessary for verifying this hypothesis.

Publications and conference

- 1) X. Zhang, F. Herklotz, E. Hieckmann, J. Weber, P. Schmidt, *Vapor phase growth of ZnO single crystals*, J. Vac. Sci. Technol. A 29, 03A107 (2011).
- 2) X. Zhang, F. Herklotz, J. Weber, *Two unique Photoluminescence emissions in vapor phase grown ZnO single crystals*, To be submitted.
- 3) X. Zhang, F. Herklotz, J. Weber, *Vapor phase growth of ZnO single crystals*, oral presentation, The 6th International Workshop on ZnO and Related Materials, August 5-7, 2012, Changchun, China.
- 4) X. Zhang, F. Herklotz, J. Weber, *Vapor phase growth of ZnO single crystals*, poster, The DPG spring meeting in 2011, March 13-18, 2011, Dresden, Germany.
- 5) X. Zhang, F. Herklotz, J. Weber, *Two unique Photoluminescence emissions in vapor phase grown ZnO single crystals*, poster, The DPG spring meeting in 2012, March 25-30, 2012, Berlin, Germany.
- 6) X. Zhang, F. Herklotz, J. Weber, *Vapor phase growth of ZnO single crystals*, poster, The 12th Dresden Microelectronics Academy, September 3-8, 2012, Dresden, Germany.

Bibliography

- [1] T. Minami, "*Transparent conducting oxide semiconductors for transparent electrodes*", *Semiconductor Science and Technology*, **20**, S35-S44 (2005)
- [2] U. Özgür, D. Hofstetter and H. Morkoç, "*ZnO devices and applications: a review of current status and future prospects*", *Proceedings of the Ieee*, **98**, 1255-1268 (2010)
- [3] S. Chu, M. Olmedo, Z. Yang, J. Y. Kong and J. L. Liu, "*Electrically pumped ultraviolet ZnO diode lasers on Si*", *Applied Physics Letters*, **93**, 181106 (2008)
- [4] G. B. Murdoch, S. Hinds, E. H. Sargent, S. W. Tsang, L. Mordoukhovski and Z. H. Lu, "*Aluminum doped zinc oxide for organic photovoltaics*", *Applied Physics Letters*, **94**, 213301 (2009)
- [5] Y. J. Lee, D. S. Ruby, D. W. Peters, B. B. McKenzie and J. W. P. Hsu, "*ZnO nanostructures as efficient antireflection layers in solar cells*", *Nano Letters*, **8**, 1501-1505 (2008)
- [6] U. Ozgur, Y. I. Alivov, C. Liu, A. Teke, M. A. Reshchikov, S. Dogan, V. Avrutin, S. J. Cho and H. Morkoc, "*A comprehensive review of ZnO materials and devices*", *Journal of Applied Physics*, **98**, 041301 (2005)
- [7] L. N. Dem'yanets and V. I. Lyutin, "*Status of hydrothermal growth of bulk ZnO: Latest issues and advantages*", *Journal of Crystal Growth*, **310**, 993-999 (2008)
- [8] K. Jacobs, D. Schulz, D. Klimm and S. Ganschow, "*Melt growth of ZnO bulk crystals in Ir crucibles*", *Solid State Sciences*, **12**, 307-310 (2010)
- [9] J. Nause and B. Nemeth, "*Pressurized melt growth of ZnO boules*", *Semiconductor Science and Technology*, **20**, S45-S48 (2005)
- [10] P. Skupinski, K. Graszka, A. Mycielski, W. Paszkowicz, E. Lusakowska, E. Tymicki, R. Jakiela and B. Witkowski, "*Seeded growth of bulk ZnO by chemical vapor transport*", *Physica Status Solidi B-Basic Solid State Physics*, **247**, 1457-1459 (2010)
- [11] B. K. Meyer, H. Alves, D. M. Hofmann, W. Kriegseis, D. Forster, F. Bertram, J. Christen, A. Hoffmann, M. Strassburg, M. Dworzak, U. Haboek and A. V. Rodina, "*Bound exciton and donor-acceptor pair recombinations in ZnO*", *Physica Status Solidi B-Basic Solid State Physics*, **241**, 231-260 (2004)
- [12] M. Tarun, M. Z. Iqbal and M. McCluskey, "*Nitrogen is a deep acceptor in ZnO*", *Aip Advances*, **1**, 022105 (2011)
- [13] V. Avrutin, D. J. Silversmith and H. Morkoc, "*Doping Asymmetry Problem in ZnO: Current Status and Outlook*", *Proceedings of the Ieee*, **98**, 1269-1280 (2010)
- [14] X. H. Wang, B. Yao, D. Z. Shen, Z. Z. Zhang, B. H. Li, Z. P. Wei, Y. M. Lu, D. X. Zhao, J. Y. Zhang, X. W. Fan, L. X. Guan and C. X. Cong, "*Optical properties of p-type ZnO doped by lithium and nitrogen*", *Solid State Communications*, **141**, 600-604 (2007)
- [15] S. Limpijumnong, S. B. Zhang, S.-H. Wei and C. H. Park, "*Doping by Large-Size-Mismatched Impurities: The Microscopic Origin of Arsenic- or Antimony-Doped p-Type Zinc Oxide*", *Physical Review Letters*, **92**, 155504 (2004)
- [16] W. Jander and W. Stamm, "*Inner formation of solid anorganic compounds at high temperatures III announcement - Electrical conductivity, diffusion capacity and reaction capacity of some balas ruby in solid status*", *Zeitschrift Fur Anorganische Und Allgemeine Chemie*, **199**, 165-182 (1931)

- [17] C. Klingshirn, J. Fallert, H. Zhou, J. Sartor, C. Thiele, F. Maier-Flaig, D. Schneider and H. Kalt, "65 years of ZnO research - old and very recent results", *Physica Status Solidi B-Basic Solid State Physics*, **247**, 1424-1447 (2010)
- [18] H. Morkoc and U. Ozgur, *Zinc Oxide - Fundamentals, Materials and Device Technology*, WILEY-VCH, Weinheim, 2009.
- [19] H. Schulz and K. H. Thiemann, "Structure Parameters and Polarity of the Wurtzite Type Compounds Sic-2h and Zno", *Solid State Communications*, **32**, 783-785 (1979)
- [20] A. Ashrafi and C. Jagadish, "Review of zincblende ZnO: Stability of metastable ZnO phases", *Journal of Applied Physics*, **102**, 071101 (2007)
- [21] S. Q. Wang, "A comparative first-principles study of ZnS and ZnO in zinc blende structure", *Journal of Crystal Growth*, **287**, 185-188 (2006)
- [22] F. Z. Aoumeur, K. Benkabou and B. Belgoumene, "Structural and dynamical properties of ZnO in zinc-blende and rocksalt phases", *Physica B-Condensed Matter*, **337**, 292-297 (2003)
- [23] J. A. Sans, A. Segura, F. J. Manjon, B. Mari, A. Munoz and M. J. Herrera-Cabrera, "Optical properties of wurtzite and rock-salt ZnO under pressure", *Microelectronics Journal*, **36**, 928-932 (2005)
- [24] J. E. Jaffe, J. A. Snyder, Z. J. Lin and A. C. Hess, "LDA and GGA calculations for high-pressure phase transitions in ZnO and MgO", *Physical Review B*, **62**, 1660-1665 (2000)
- [25] M. Murayama and T. Nakayama, "Chemical Trend of Band Offsets at Wurtzite Zincblende Heterocrystalline Semiconductor Interfaces", *Physical Review B*, **49**, 4710-4724 (1994)
- [26] G. F. Koster, J. O. Dimmock, R. G. Wheeler and H. Statz, *The Properties of the Thirty-Two Point Groups*, M.I.T Press, Cambridge, MA, 1963.
- [27] A. B. M. A. Ashrafi, A. Ueta, A. Avramescu, H. Kumano, I. Suemune, Y. W. Ok and T. Y. Seong, "Growth and characterization of hypothetical zinc-blende ZnO films on GaAs(001) substrates with ZnS buffer layers", *Applied Physics Letters*, **76**, 550-552 (2000)
- [28] A. A. Ashrafi, A. Ueta, H. Kumano and I. Suemune, "Role of ZnS buffer layers in growth of zincblende ZnO on GaAs substrates by metalorganic molecular-beam epitaxy", *Journal of Crystal Growth*, **221**, 435-439 (2000)
- [29] G. H. Lee, T. Kawazoe and M. Ohtsu, "Room temperature near-field photoluminescence of zinc-blende and wurtzite ZnO structures", *Applied Surface Science*, **239**, 394-397 (2005)
- [30] S. K. Kim, S. Y. Jeong and C. R. Cho, "Structural reconstruction of hexagonal to cubic ZnO films on Pt/Ti/SiO₂/Si substrate by annealing", *Applied Physics Letters*, **82**, 562-564 (2003)
- [31] X. W. Sun, Z. J. Liu, Q. F. Chen, H. W. Lu, T. Song and C. W. Wang, "Heat capacity of ZnO with cubic structure at high temperatures", *Solid State Communications*, **140**, 219-224 (2006)
- [32] J. E. Jaffe and A. C. Hess, "Hartree-Fock Study of Phase-Changes in ZnO at High-Pressure", *Physical Review B*, **48**, 7903-7909 (1993)
- [33] C. Jagadish and S. J. Pearton, *Zinc oxide bulk, thin films and nanostructures: processing, properties, and applications*, Elsevier Science, 2006.
- [34] A. N. Mariano and R. E. Hanneman, "Crystallographic Polarity of ZnO Crystals", *Journal of Applied Physics*, **34**, 384-388 (1963)
- [35] C. Woll, "The chemistry and physics of zinc oxide surfaces", *Progress in surface science*, **82**, 55-120 (2007)
- [36] R. R. Reeber, "Lattice Parameters of ZnO from 4.2 Degrees to 296 Degrees K", *Journal of Applied Physics*, **41**, 5063-5066 (1970)

- [37] C. H. Bates, R. Roy and W. B. White, "New High-Pressure Polymorph of Zinc Oxide", *Science*, **137**, 993-993 (1962)
- [38] J. M. Recio, M. A. Blanco, V. Luana, R. Pandey, L. Gerward and J. S. Olsen, "Compressibility of the high-pressure rocksalt phase of ZnO", *Physical Review B*, **58**, 8949-8954 (1998)
- [39] Y. Wang, Y. Zhang, W. J. Chang, G. L. Lu, J. Z. Jiang, Y. C. Li, J. Liu and T. D. Hu, "Mn effect on wurtzite-to-cubic phase transformation in ZnO", *Journal of Physics and Chemistry of Solids*, **66**, 1775-1778 (2005)
- [40] P. Schroer, P. Kruger and J. Pollmann, "First-principles Calculation of the Electronic-Structure of the Wurtzite Semiconductors ZnO and ZnS", *Physical Review B*, **47**, 6971-6980 (1993)
- [41] Y. N. Xu and W. Y. Ching, "Electronic, Optical, and Structural-Properties of Some Wurtzite Crystals", *Physical Review B*, **48**, 4335-4351 (1993)
- [42] A. Janotti and C. G. Van de Walle, "Native point defects in ZnO", *Physical Review B*, **76**, 165202 (2007)
- [43] A. F. Kohan, G. Ceder, D. Morgan and C. G. Van de Walle, "First-principles study of native point defects in ZnO", *Physical Review B*, **61**, 15019-15027 (2000)
- [44] C. G. Van de Walle, "Defect analysis and engineering in ZnO", *Physica B-Condensed Matter*, **308**, 899-903 (2001)
- [45] P. Erhart and K. Albe, "First-principles study of migration mechanisms and diffusion of oxygen in zinc oxide", *Physical Review B*, **73**, 115207 (2006)
- [46] S. Lany and A. Zunger, "Dopability, intrinsic conductivity, and nonstoichiometry of transparent conducting oxides", *Physical Review Letters*, **98**, 045501 (2007)
- [47] C. H. Patterson, "Role of defects in ferromagnetism in Zn_{1-x}CoxO: A hybrid density-functional study", *Physical Review B*, **74**, 144432 (2006)
- [48] F. J. Himpsel, "Angle-Resolved Measurements of the Photoemission of Electrons in the Study of Solids", *Advances in Physics*, **32**, 1-51 (1983)
- [49] W. J. Fan, J. B. Xia, P. A. Agus, S. T. Tan, S. F. Yu and X. W. Sun, "Band parameters and electronic structures of wurtzite ZnO and ZnO/MgZnO quantum wells", *Journal of Applied Physics*, **99**, 013702 (2006)
- [50] W. R. L. Lambrecht, A. V. Rodina, S. Limpijumnong, B. Segall and B. K. Meyer, "Valence-band ordering and magneto-optic exciton fine structure in ZnO", *Physical Review B*, **65**, 075207 (2002)
- [51] C. F. Klingshirn, B. K. Meyer, A. Waag, A. Hoffmann and J. Geurts, *Zinc Oxide: From Fundamental Properties Towards Novel Applications*, Springer, 2010.
- [52] D. C. Reynolds, D. C. Look, B. Jogai, C. W. Litton, G. Cantwell and W. C. Harsch, "Valence-band ordering in ZnO", *Physical Review B*, **60**, 2340-2344 (1999)
- [53] Landolt-Börnstein, *Numerical Data and Functional Relationships in Science and Technology, Vol. III/17b and iii/41*, Springer-Verlag, Berlin, 1987.
- [54] V. A. Coleman and C. Jagadish, in *Zinc Oxide Bulk, Thin Films and Nanostructures*, eds. J. Chennupati and P. Stephen, Elsevier Science Ltd, Oxford, 2006, pp. 1-20.
- [55] K. Koike, K. Hama, I. Nakashima, G. Takada, K. Ogata, S. Sasa, M. Inoue and M. Yano, "Molecular beam epitaxial growth of wide bandgap ZnMgO alloy films on (111)-oriented Si substrate toward UV-detector applications", *Journal of Crystal Growth*, **278**, 288-292 (2005)
- [56] S. Shigemori, A. Nakamura, J. Ishihara, T. Aoki and J. Temmyo, "Zn_{1-x}Cd_xO film growth

- using remote plasma-enhanced metalorganic chemical vapor deposition*", Japanese Journal of Applied Physics Part 2-Letters & Express Letters, **43**, L1088-L1090 (2004)
- [57] T. Makino, Y. Segawa, M. Kawasaki, A. Ohtomo, R. Shiroki, K. Tamura, T. Yasuda and H. Koinuma, "*Band gap engineering based on $Mg_xZn_{1-x}O$ and $Cd_yZn_{1-y}O$ ternary alloy films*", Applied Physics Letters, **78**, 1237-1239 (2001)
- [58] Ü. Özgür and H. Morkoç, in *Zinc Oxide Bulk, Thin Films and Nanostructures*, eds. J. Chennupati and P. Stephen, Elsevier Science Ltd, Oxford, 2006, pp. 175-239.
- [59] P. Y. Yu and M. Cardona, *Fundamentals of semiconductors: physics and materials properties*, Springer Berlin, 1999.
- [60] S. W. Koch, M. Kira, G. Khitrova and H. M. Gibbs, "*Semiconductor excitons in new light*", Nature Materials, **5**, 523-531 (2006)
- [61] C. F. Klingshirn, *Semiconductor optics*, 2 edn., Springer Verlag, 2005.
- [62] R. J. Mendelsberg, *Photoluminescence of ZnO Grown by Eclipse Pulsed Laser deposition*, Ph.D thesis, University of Canterbury, 2009.
- [63] V. Heine, *Group Theory in Quantum Mechanics: An Introduction to Its Present Usage*, Dover Publications, 1993.
- [64] P. Miller, *Zinc Oxide: A spectroscopic investigation of bulk crystals and thin films*, Ph.D thesis, University of Canterbury, 2008.
- [65] B. K. Meyer, J. Sann, S. Lautenschlager, M. R. Wagner and A. Hoffmann, "*Ionized and neutral donor-bound excitons in ZnO*", Physical Review B, **76**, 184120 (2007)
- [66] A. Teke, U. Ozgur, S. Dogan, X. Gu, H. Morkoc, B. Nemeth, J. Nause and H. O. Everitt, "*Excitonic fine structure and recombination dynamics in single-crystalline ZnO*", Physical Review B, **70**, 195207 (2004)
- [67] C. F. Klingshirn, A. Waag, A. Hoffmann and J. Geurts, *Zinc Oxide: From Fundamental Properties Towards Novel Applications*, Springer, 2010.
- [68] M. Schirra, R. Schneider, A. Reiser, G. M. Prinz, M. Feneberg, J. Biskupek, U. Kaiser, C. E. Krill, K. Thonke and R. Sauer, "*Stacking fault related 3.31-eV luminescence at 130-meV acceptors in zinc oxide*", Physical Review B, **77**, 125215 (2008)
- [69] X. Zhang, T. Taliercio, S. Kolliakos and P. Lefebvre, "*Influence of electron-phonon interaction on the optical properties of III nitride semiconductors*", Journal of Physics: Condensed Matter, **13**, 7053 (2001)
- [70] A. Chernikov, V. Bornwasser, M. Koch, S. Chatterjee, C. N. Böttge, T. Feldtmann, M. Kira, S. W. Koch, T. Wassner, S. Lautenschläger, B. K. Meyer and M. Eickhoff, "*Phonon-assisted luminescence of polar semiconductors: Fröhlich coupling versus deformation-potential scattering*", Physical Review B, **85**, 035201 (2012)
- [71] S. Xu, S.-J. Xiong and S. Shi, "*Resonant coupling of bound excitons with LO phonons in ZnO: Excitonic polaron states and Fano interference*", The Journal of chemical physics, **123**, 221105 (2005)
- [72] A. L. Gurskii and S. V. Voitikov, "*Quantum defect approach for the effect of electron-phonon coupling on impurity recombination in semiconductors*", Solid State Communications, **112**, 339-343 (1999)
- [73] R. J. Mendelsberg, M. W. Allen, S. M. Durbin and R. J. Reeves, "*Photoluminescence and the exciton-phonon coupling in hydrothermally grown ZnO*", Physical Review B, **83**, 205202 (2011)

- [74] U. Fano, "*Effects of Configuration Interaction on Intensities and Phase Shifts*", *Physical Review*, **124**, 1866-1878 (1961)
- [75] K.-j. Jin and S. Xu, "*Fano resonance in the luminescence spectra of donor bound excitons in polar semiconductors*", *Applied Physics Letters*, **90**, 032107 (2007)
- [76] H. J. Queisser and E. E. Haller, "*Defects in semiconductors: Some fatal, some vital*", *Science*, **281**, 945-950 (1998)
- [77] C. G. Van de Walle and J. Neugebauer, "*First-principles calculations for defects and impurities: Applications to III-nitrides*", *Journal of Applied Physics*, **95**, 3851-3879 (2004)
- [78] F. Gallino, G. Pacchioni and C. Di Valentin, "*Transition levels of defect centers in ZnO by hybrid functionals and localized basis set approach*", *Journal of Chemical Physics*, **133**, 144512 (2010)
- [79] M. D. McCluskey and S. J. Jokela, "*Defects in ZnO*", *Journal of Applied Physics*, **106**, 071101 (2009)
- [80] K. Vanheusden, W. L. Warren, C. H. Seager, D. R. Tallant, J. A. Voigt and B. E. Gnade, "*Mechanisms behind green photoluminescence in ZnO phosphor powders*", *Journal of Applied Physics*, **79**, 7983-7990 (1996)
- [81] L. A. Kappers, O. R. Gilliam, S. M. Evans, L. E. Halliburton and N. C. Giles, "*EPR and optical study of oxygen and zinc vacancies in electron-irradiated ZnO*", *Nuclear Instruments and Methods in Physics Research Section B: Beam Interactions with Materials and Atoms*, **266**, 2953-2957 (2008)
- [82] L. S. Vlasenko and G. D. Watkins, "*Optical detection of electron paramagnetic resonance in room-temperature electron-irradiated ZnO*", *Physical Review B*, **71**, 125210 (2005)
- [83] A. Janotti and C. G. Van de Walle, "*Oxygen vacancies in ZnO*", *Applied Physics Letters*, **87**, 122102 (2005)
- [84] F. Tuomisto, V. Ranki, K. Saarinen and D. C. Look, "*Evidence of the Zn vacancy acting as the dominant acceptor in n-type ZnO*", *Physical Review Letters*, **91**, 205502 (2003)
- [85] L. S. Vlasenko and G. D. Watkins, "*Optical detection of electron paramagnetic resonance for intrinsic defects produced in ZnO by 2.5-MeV electron irradiation in situ at 4.2 K*", *Physical Review B*, **72**, 035203 (2005)
- [86] F. Herklotz, E. V. Lavrov and J. Weber, "*Photoluminescence study of hydrogen donors in ZnO*", *Physica B-Condensed Matter*, **404**, 4349-4353 (2009)
- [87] E. V. Lavrov, F. Herklotz and J. Weber, "*Identification of two hydrogen donors in ZnO*", *Physical Review B*, **79**, 165210 (2009)
- [88] C. G. Van de Walle, "*Hydrogen as a cause of doping in zinc oxide*", *Physical Review Letters*, **85**, 1012-1015 (2000)
- [89] S. F. J. Cox, E. A. Davis, S. P. Cottrell, P. J. C. King, J. S. Lord, J. M. Gil, H. V. Alberto, R. C. Vilao, J. P. Duarte, N. A. de Campos, A. Weidinger, R. L. Lichti and S. J. C. Irvine, "*Experimental confirmation of the predicted shallow donor hydrogen state in zinc oxide*", *Physical Review Letters*, **86**, 2601-2604 (2001)
- [90] E. V. Lavrov, F. Herklotz and J. Weber, "*Identification of Hydrogen Molecules in ZnO*", *Physical Review Letters*, **102**, 185502 (2009)
- [91] S. J. Jokela and M. D. McCluskey, "*Unambiguous identification of nitrogen-hydrogen complexes in ZnO*", *Physical Review B*, **76**, 193201 (2007)
- [92] M. G. Wardle, J. P. Goss and P. R. Briddon, "*Theory of Li in ZnO: A limitation for Li-based*

- p-type doping*", Physical Review B, **71**, 155205 (2005)
- [93] J. J. Lander, "Reactions of Lithium as a Donor and an Acceptor in ZnO", Journal of Physics and Chemistry of Solids, **15**, 324-334 (1960)
- [94] A. Carvalho, A. Alkauskas, A. Pasquarello, A. K. Tagantsev and N. Setter, "A hybrid density functional study of lithium in ZnO: Stability, ionization levels, and diffusion", Physical Review B, **80**, 195205 (2009)
- [95] W. Liu, F. X. Xiu, K. Sun, Y. H. Xie, K. L. Wang, Y. Wang, J. Zou, Z. Yang and J. L. Liu, "Na-Doped p-Type ZnO Microwires", Journal of the American Chemical Society, **132**, 2498-2499 (2010)
- [96] R. Dingle, "Luminescent Transitions Associated With Divalent Copper Impurities and the Green Emission from Semiconducting Zinc Oxide", Physical Review Letters, **23**, 579-581 (1969)
- [97] N. Y. Garces, L. Wang, L. Bai, N. C. Giles, L. E. Halliburton and G. Cantwell, "Role of copper in the green luminescence from ZnO crystals", Applied Physics Letters, **81**, 622-624 (2002)
- [98] J. L. Lyons, A. Janotti and C. G. Van de Walle, "Why nitrogen cannot lead to p-type conductivity in ZnO", Applied Physics Letters, **95**, 252105 (2009)
- [99] W.-J. Lee, J. Kang and K. J. Chang, "Defect properties and p-type doping efficiency in phosphorus-doped ZnO", Physical Review B, **73**, 024117 (2006)
- [100] C. H. Park, S. B. Zhang and S.-H. Wei, "Origin of p-type doping difficulty in ZnO: The impurity perspective", Physical Review B, **66**, 073202 (2002)
- [101] Y. R. Ryu, T. S. Lee and H. W. White, "Properties of arsenic-doped p-type ZnO grown by hybrid beam deposition", Applied Physics Letters, **83**, 87-89 (2003)
- [102] F. X. Xiu, Z. Yang, L. J. Mandalapu, D. T. Zhao, J. L. Liu and W. P. Beyermann, "High-mobility Sb-doped p-type ZnO by molecular-beam epitaxy", Applied Physics Letters, **87**, 152101 (2005)
- [103] M. Wagner, G. Callsen, J. Reparaz, J.-H. Schulze, R. Kirste, M. Cobet, I. Ostapenko, S. Rodt, C. Nenstiel and M. Kaiser, "Bound excitons in ZnO: Structural defect complexes versus shallow impurity centers", Physical Review B, **84**, 035313 (2011)
- [104] G. D. Mahan, "Intrinsic Defects in ZnO Varistors", Journal of Applied Physics, **54**, 3825-3832 (1983)
- [105] J. M. Carlsson, H. S. Domingos, P. D. Bristowe and B. Hellsing, "An Interfacial Complex in ZnO and Its Influence on Charge Transport", Physical Review Letters, **91**, 165506 (2003)
- [106] B. Szyszka, P. Loebmann, A. Georg, C. May and C. Elsaesser, "Development of new transparent conductors and device applications utilizing a multidisciplinary approach", Thin Solid Films, **518**, 3109-3114 (2010)
- [107] M. Biswas, Y. S. Jung, H. K. Kim, K. Kumar, G. J. Hughes, S. Newcomb, M. O. Henry and E. McGlynn, "Microscopic origins of the surface exciton photoluminescence peak in ZnO nanostructures", Physical Review B, **83**, 235320 (2011)
- [108] L. Wischmeier, T. Voss, I. Ruckmann and J. Gutowski, "Correlations between surface-excitonic emission bands in ZnO nanowires", Nanotechnology, **19**, 135705 (2008)
- [109] G. H. Coccoletzi and W. L. Mochan, "Excitons: from excitations at surfaces to confinement in nanostructures", Surface Science Reports, **57**, 1-58 (2005)
- [110] D. Ehrentraut, H. Sato, Y. Kagamitani, H. Sato, A. Yoshikawa and T. Fukuda, "Solvochemical growth of ZnO", Progress in Crystal Growth and Characterization of Materials, **52**, 280-335

- (2006)
- [111] V. Avrutin, G. Cantwell, J. Z. Zhang, J. J. Song, D. J. Silversmith and H. Morkoc, "*Bulk ZnO: Current Status, Challenges, and Prospects*", Proceedings of the Ieee, **98**, 1339-1350 (2010)
- [112] T. Sekiguchi, S. Miyashita, K. Obara, T. Shishido and N. Sakagami, "*Hydrothermal growth of ZnO single crystals and their optical characterization*", Journal of Crystal Growth, **214–215**, 72-76 (2000)
- [113] K. Maeda, M. Sato, I. Niikura and T. Fukuda, "*Growth of 2 inch ZnO bulk single crystal by the hydrothermal method*", Semiconductor Science and Technology, **20**, S49-S54 (2005)
- [114] D. Schulz, S. Ganschow, D. Klimm, M. Neubert, M. Roßberg, M. Schmidbauer and R. Fornari, "*Bridgman-grown zinc oxide single crystals*", Journal of Crystal Growth, **296**, 27-30 (2006)
- [115] D. Klimm, S. Ganschow, D. Schulz and R. Fornari, "*The growth of ZnO crystals from the melt*", Journal of Crystal Growth, **310**, 3009-3013 (2008)
- [116] D. Schulz, S. Ganschow, D. Klimm and K. Struve, "*Inductively heated Bridgman method for the growth of zinc oxide single crystals*", Journal of Crystal Growth, **310**, 1832-1835 (2008)
- [117] D. C. Look, D. C. Reynolds, J. R. Sizelove, R. L. Jones, C. W. Litton, G. Cantwell and W. C. Harsch, "*Electrical properties of bulk ZnO*", Solid State Communications, **105**, 399-401 (1998)
- [118] M. Mikami, T. Eto, J. Wang, Y. Masa and M. Isshiki, "*Growth of zinc oxide by chemical vapor transport*", Journal of Crystal Growth, **276**, 389-392 (2005)
- [119] J. M. Ntep, S. Said Hassani, A. Lussou, A. Tromson-Carli, D. Ballutaud, G. Didier and R. Triboulet, "*ZnO growth by chemical vapour transport*", Journal of Crystal Growth, **207**, 30-34 (1999)
- [120] O. Oda, *Compound semiconductor bulk materials and characterizations*, World Scientific, 2007.
- [121] E. M. Dodson and J. A. Savage, "*Vapour Growth of Single-Crystal Zinc Oxide*", Journal of Materials Science, **3**, 19-25 (1968)
- [122] K. Fischer, "*Vapor phase growth of ZnO crystals in an open flow system*", Journal of Crystal Growth, **34**, 139-144 (1976)
- [123] K. Nielsen, "*Growth of ZnO single crystals by the vapor phase reaction method*", Journal of Crystal Growth, **3**, 141-145 (1968)
- [124] X. Zhang, F. Herklotz, E. Hieckmann, J. Weber and P. Schmidt, "*Vapor phase growth of ZnO single crystals*", Journal of Vacuum Science & Technology A, **29**, 03A107 (2011)
- [125] R. Helbig, "*Über die züchtung von grösseren reinen und dotierten ZnO-kristallen aus der gasphase*", Journal of Crystal Growth, **15**, 25-31 (1972)
- [126] R. Triboulet and J. Perrière, "*Epitaxial growth of ZnO films*", Progress in Crystal Growth and Characterization of Materials, **47**, 65-138 (2003)
- [127] V. Craciun, J. Elders, J. G. E. Gardeniers and I. W. Boyd, "*Characteristics of High Quality ZnO Thin Films Deposited by Pulsed Laser Deposition*", Applied Physics Letters, **65**, 2963-2965 (1994)
- [128] P. R. Willmott and J. R. Huber, "*Pulsed laser vaporization and deposition*", Reviews of Modern Physics, **72**, 315-328 (2000)
- [129] M. A. Herman and H. Sitter, *Molecular beam epitaxy: fundamentals and current status*, Springer-Verlag Berlin, 1989.
- [130] D. Lide, *CRC Handbook of Chemistry and Physics*, 79th edn., CRC Press, Boca Raton, FL, 1999.

- [131] D. C. Look, K. Leedy, D. Tomich and B. Bayraktaroglu, "Mobility analysis of highly conducting thin films: Application to ZnO", *Applied Physics Letters*, **96**, 062102 (2010)
- [132] M. Kumar, S.-K. Kim and S.-Y. Choi, "Formation of Al-N co-doped p-ZnO/n-Si (100) heterojunction structure by RF co-sputtering technique", *Applied Surface Science*, **256**, 1329-1332 (2009)
- [133] X. Cui, T. Zhang, Z. Mei, Z. Liu, Y. Liu, Y. Guo, Q. Xue and X. Du, "Growth of single-crystalline ZnO film with two-dimensional periodic structure on Si (111) substrate by molecular beam epitaxy", *Journal of Crystal Growth*, **310**, 5428-5431 (2008)
- [134] F. Herklotz, *Hydrogen-related defects in ZnO and TiO₂*, Ph.D thesis, Technische Universität Dresden, 2011.
- [135] C. F. Bohren and E. Clothiaux, *Fundamentals of atmospheric radiation*, WILEY-VCH, Weinheim, 2006.
- [136] T. Schmidt, K. Lischka and W. Zulehner, "Excitation-power dependence of the near-band-edge photoluminescence of semiconductors", *Physical Review B*, **45**, 8989-8994 (1992)
- [137] Z. C. Feng, A. Mascarenhas and W. J. Choyke, "Low temperature photoluminescence spectra of (001) CdTe films grown by molecular beam epitaxy at different substrate temperatures", *Journal of Luminescence*, **35**, 329-341 (1986)
- [138] P. R. Okamoto, E. Levine and G. Thomas, "Kikuchi Maps for Hcp and Bcc Crystals", *Journal of Applied Physics*, **38**, 289-296 (1967)
- [139] K. Z. Baba-Kishi, "Review - Electron backscatter Kikuchi diffraction in the scanning electron microscope for crystallographic analysis", *Journal of Materials Science*, **37**, 1715-1746 (2002)
- [140] D. L. BRANSON, "Kinetics and mechanism of the reaction between zinc oxide and aluminum oxide", *Journal of the American Ceramic Society*, **48**, 591-595 (1965)
- [141] F. Leiter, H. Zhou, F. Henecker, A. Hofstaetter, D. M. Hofmann and B. K. Meyer, "Magnetic resonance experiments on the green emission in undoped ZnO crystals", *Physica B: Condensed Matter*, **308-310**, 908-911 (2001)
- [142] C. H. Lee, G. C. Yi, Y. M. Zuev and P. Kim, "Thermoelectric power measurements of wide band gap semiconducting nanowires", *Applied Physics Letters*, **94**, 022106 (2009)
- [143] E. Brandes and V. Schröder, "Explosionsgrenzen bei nichtatmosphärischen Bedingungen", *Chemie Ingenieur Technik*, **81**, 153-158 (2008)
- [144] C. L. Tang, Z. H. Huang, C. Jin, J. J. He, J. H. Wang, X. B. Wang and H. Y. Miao, "Explosion characteristics of hydrogen-nitrogen-air mixtures at elevated pressures and temperatures", *International Journal of Hydrogen Energy*, **34**, 554-561 (2009)
- [145] A. Myerson, *Handbook of industrial crystallization (Second Edition)* Butterworth-Heinemann, 2002.
- [146] F. Römer and T. Kraska, "Homogeneous nucleation and growth in supersaturated zinc vapor investigated by molecular dynamics simulation", *The Journal of chemical physics*, **127**, 234509 (2007)
- [147] K. Ellmer, A. Klein and B. Rech, *Transparent Conductive Zinc Oxide: Basics and Applications in Thin Film Solar Cells*, Springer, 2008.
- [148] T. Terasako, K. Taira, K. Taniguchi, M. Yagi and S. Shirakata, "Structural and optical properties of ZnO films grown by atmospheric pressure CVD methods using different source

- materials*", *physica status solidi (c)*, **8**, 509-511 (2011)
- [149] D. M. Murphy and T. Koop, "Review of the vapour pressures of ice and supercooled water for atmospheric applications", *Quarterly Journal of the Royal Meteorological Society*, **131**, 1539-1565 (2005)
- [150] J. Sann, J. Stehr, A. Hofstaetter, D. M. Hofmann, A. Neumann, M. Lerch, U. Haboeck, A. Hoffmann and C. Thomsen, "Zn interstitial related donors in ammonia-treated ZnO powders", *Physical Review B*, **76**, 195203 (2007)
- [151] D. G. Thomas, "Interstitial Zinc in Zinc Oxide", *Journal of Physics and Chemistry of Solids*, **3**, 229-237 (1957)
- [152] M. Brandt, H. von Wenckstern, G. Benndorf, M. Lange, C. P. Dietrich, C. Kranert, C. Sturm, R. Schmidt-Grund, H. Hochmuth, M. Lorenz, M. Grundmann, M. R. Wagner, M. Alic, C. Nenstiel and A. Hoffmann, "Identification of a donor-related recombination channel in ZnO thin films", *Physical Review B*, **81**, 073306 (2010)
- [153] A. Schildknecht, R. Sauer and K. Thonke, "Donor-related defect states in ZnO substrate material", *Physica B-Condensed Matter*, **340**, 205-209 (2003)
- [154] E. V. Lavrov, J. Weber and F. Börrnert, "Copper dihydrogen complex in ZnO", *Physical Review B*, **77**, 155209 (2008)
- [155] T. Gruber, G. M. Prinz, C. Kirchner, R. Kling, F. Reuss, W. Limmer and A. Waag, "Influences of biaxial strains on the vibrational and exciton energies in ZnO", *Journal of Applied Physics*, **96**, 289-293 (2004)
- [156] M. R. Wagner, T. P. Bartel, R. Kirste, A. Hoffmann, J. Sann, S. Lautenschläger, B. K. Meyer and C. Kisielowski, "Influence of substrate surface polarity on homoepitaxial growth of ZnO layers by chemical vapor deposition", *Physical Review B*, **79**, 035307 (2009)
- [157] C. G. Van de Walle and J. Neugebauer, "Universal alignment of hydrogen levels in semiconductors, insulators and solutions", *Nature*, **423**, 626-628 (2003)
- [158] H. B. Michaelson, "The Work Function of Elements and Its Periodicity", *Journal of Applied Physics*, **48**, 4729-4733 (1977)
- [159] A. Tsukazaki, A. Ohtomo, T. Onuma, M. Ohtani, T. Makino, M. Sumiya, K. Ohtani, S. F. Chichibu, S. Fuke and Y. Segawa, "Repeated temperature modulation epitaxy for p-type doping and light-emitting diode based on ZnO", *Nature Materials*, **4**, 42-46 (2004)
- [160] J. Sann, A. Hofstaetter, D. Pfisterer, J. Stehr and B. K. Meyer, "Acceptor doping in ZnO with group - I elements", *physica status solidi (c)*, **3**, 952-955 (2006)
- [161] O. Maksimov, "Recent Advances and Novel Approaches of P-Type Doping of Zinc Oxide", *Reviews on Advanced Materials Science*, **24**, 26-34 (2010)
- [162] X. Li, Y. Yan, T. A. Gessert, C. DeHart, C. L. Perkins, D. Young and T. J. Coutts, "p-type ZnO thin films formed by CVD reaction of diethylzinc and NO gas", *Electrochemical and Solid State Letters*, **6**, C56-C58 (2003)
- [163] S. Jang, J. J. Chen, B. S. Kang, F. Ren, D. P. Norton, S. J. Pearton, J. Lopata and W. S. Hobson, "Formation of p-n homojunctions in n-ZnO bulk single crystals by diffusion from a Zn3P2 source", *Applied Physics Letters*, **87** (2005)
- [164] Z. G. Yu, P. Wu and H. Gong, "Control of p- and n-type conductivities in P doped ZnO thin films by using radio-frequency sputtering", *Applied Physics Letters*, **88**, 132114 (2006)
- [165] Y. R. Ryu, S. Zhu, D. C. Look, J. M. Wrobel, H. M. Jeong and H. W. White, "Synthesis of p-type ZnO films", *Journal of Crystal Growth*, **216**, 330-334 (2000)

- [166] D. C. Look, G. M. Renlund, R. H. Burgener and J. R. Sizelove, "*As-doped p-type ZnO produced by an evaporation/sputtering process*", Applied Physics Letters, **85**, 5269-5271 (2004)
- [167] V. Vaithianathan, B. T. Lee, C. H. Chang, K. Asokan and S. S. Kim, "*Characterization of As-doped, p-type ZnO by x-ray absorption near-edge structure spectroscopy*", Applied Physics Letters, **88**, 222113 (2006)
- [168] J. C. Sun, J. Z. Zhao, H. W. Liang, J. M. Bian, L. Z. Hu, H. Q. Zhang, X. P. Liang, W. F. Liu and G. T. Du, "*Realization of ultraviolet electroluminescence from ZnO homojunction with n-ZnO/p-ZnO : As/GaAs structure*", Applied Physics Letters, **90**, 121128 (2007)
- [169] C. Yuen, S. F. Yu, E. S. P. Leong, S. P. Lau, K. Pita, H. Y. Yang and T. P. Chen, "*Room temperature deposition of p-type arsenic doped ZnO polycrystalline films by laser-assist filtered cathodic vacuum arc technique*", Journal of Applied Physics, **101**, 094905 (2007)
- [170] L. J. Mandalapu, Z. Yang, F. X. Xiu, D. T. Zhao and J. L. Liu, "*Homojunction photodiodes based on Sb-doped p-type ZnO for ultraviolet detection*", Applied Physics Letters, **88**, 041107 (2006)
- [171] W. Guo, A. Allenic, Y. B. Chen, X. Q. Pan, Y. Che, Z. D. Hu and B. Liu, "*Microstructure and properties of epitaxial antimony-doped p-type ZnO films fabricated by pulsed laser deposition*", Applied Physics Letters, **90**, 242108 (2007)
- [172] J. G. Lu, Y. Z. Zhang, Z. Z. Ye, Y. J. Zeng, H. P. He, L. P. Zhu, J. Y. Huang, L. Wang, J. Yuan, B. H. Zhao and X. H. Li, "*Control of p- and n-type conductivities in Li-doped ZnO thin films*", Applied Physics Letters, **89**, 112113 (2006)
- [173] J. G. Lu, Z. Z. Ye, F. Zhuge, Y. J. Zeng, B. H. Zhao and L. P. Zhu, "*p-type conduction in N-Al co-doped ZnO thin films*", Applied Physics Letters, **85**, 3134-3135 (2004)
- [174] J. G. Lu, Z. Z. Ye, G. D. Yuan, Y. J. Zeng, F. Zhuge, L. P. Zhu, B. H. Zhao and S. B. Zhang, "*Electrical characterization of ZnO-based homojunctions*", Applied Physics Letters, **89**, 053501 (2006)
- [175] A. Tsukazaki, A. Ohtomo, T. Onuma, M. Ohtani, T. Makino, M. Sumiya, K. Ohtani, S. F. Chichibu, S. Fuke, Y. Segawa, H. Ohno, H. Koinuma and M. Kawasaki, "*Repeated temperature modulation epitaxy for p-type doping and light-emitting diode based on ZnO*", Nature Materials, **4**, 42-46 (2005)
- [176] H. S. Kang, B. D. Ahn, J. H. Kim, G. H. Kim, S. H. Lim, H. W. Chang and S. Y. Lee, "*Structural, electrical, and optical properties of p-type ZnO thin films with Ag dopant*", Applied Physics Letters, **88**, 202108 (2006)
- [177] N. Garces, L. Wang, N. Giles, L. Halliburton, D. Look and D. Reynolds, "*Thermal diffusion of lithium acceptors into ZnO crystals*", Journal of Electronic Materials, **32**, 766-771 (2003)
- [178] S. Lany and A. Zunger, "*Generalized Koopmans density functional calculations reveal the deep acceptor state of N_O in ZnO*", Physical Review B, **81**, 205209 (2010)
- [179] R. Huang, S. G. Xu, W. H. Guo, L. Wang, J. Song, T. W. Ng, J. A. Huang, S. T. Lee, S. W. Du and N. Wang, "*Nitrogen deep acceptors in ZnO nanowires induced by ammonia plasma*", Applied Physics Letters, **99**, 143112 (2011)
- [180] N. H. Nickel and M. A. Gluba, "*Defects in Compound Semiconductors Caused by Molecular Nitrogen*", Physical Review Letters, **103**, 145501 (2009)
- [181] J. Gao, R. Qin, G. Luo, J. Lu, Y. Leprince-Wang, H. Ye, Z. Liao, Q. Zhao and D. Yu, "*First-principles study of the formation mechanisms of nitrogen molecule in annealed ZnO*",

- Physics Letters A, **374**, 3546-3550 (2010)
- [182] S. Jokela and M. McCluskey, "*Structure and stability of N-H complexes in single-crystal ZnO*", Journal of Applied Physics, **107**, 113536 (2010)
- [183] W. Liu, S. L. Gu, J. D. Ye, S. M. Zhu, Y. X. Wu, Z. P. Shan, R. Zhang, Y. D. Zheng, S. F. Choy, G. Q. Lo and X. W. Sun, "*High temperature dehydrogenation for realization of nitrogen-doped p-type ZnO*", Journal of Crystal Growth, **310**, 3448-3452 (2008)
- [184] W.-J. Lee, J. Kang and K. J. Chang, "*Electronic structure of phosphorus dopants in ZnO*", Physica B: Condensed Matter, **376-377**, 699-702 (2006)
- [185] D. C. Look, B. Claflin and H. E. Smith, "*Origin of conductive surface layer in annealed ZnO*", Applied Physics Letters, **92**, 122108 (2008)
- [186] Y. Yan and S. H. Wei, "*Doping asymmetry in wide-bandgap semiconductors: Origins and solutions*", Physica Status Solidi B-Basic Solid State Physics, **245**, 641-652 (2008)
- [187] X. Tang, Y. Deng, D. Wagner, L. Yu and H. Lü, "*Possible approach to fabricate p-type ZnO through the Be-N codoping method: First-principles calculations*", Solid State Communications, **152**, 1-4 (2012)
- [188] Y. F. Yan, S. B. Zhang and S. T. Pantelides, "*Control of doping by impurity chemical potentials: Predictions for p-type ZnO*", Physical Review Letters, **86**, 5723-5726 (2001)
- [189] T. Barnes, J. Leaf, S. Hand, C. Fry and C. Wolden, "*A comparison of plasma-activated N₂ / O₂ and N₂O / O₂ mixtures for use in ZnO: N synthesis by chemical vapor deposition*", Journal of Applied Physics, **96**, 7036-7044 (2004)
- [190] X. Y. Chen, Z. Z. Zhang, B. Yao, M. M. Jiang, S. P. Wang, B. H. Li, C. X. Shan, L. Liu, D. X. Zhao, H. F. Zhao and D. Z. Shen, "*Control of N/N(2) species ratio in NO plasma for p-type doping of ZnO*", Journal of Applied Physics, **110**, 053305 (2011)
- [191] H. Matsui, H. Saeki, T. Kawai, H. Tabata and B. Mizobuchi, "*N doping using N₂O and NO sources: From the viewpoint of ZnO*", Journal of Applied Physics, **95**, 5882-5888 (2004)
- [192] E.-C. Lee, Y. S. Kim, Y. G. Jin and K. J. Chang, "*Compensation mechanism for N acceptors in ZnO*", Physical Review B, **64**, 085120 (2001)
- [193] Y. Marfaing and A. Lusson, "*Doping engineering of p-type ZnO*", Superlattices and Microstructures, **38**, 385-396 (2005)
- [194] J. Xu, R. Ott, A. S. Sabau, Z. W. Pan, F. X. Xiu, J. L. Liu, J. M. Erie and D. P. Norton, "*Generation of nitrogen acceptors in ZnO using pulse thermal processing*", Applied Physics Letters, **92**, 151112 (2008)
- [195] L. G. Wang and A. Zunger, "*Cluster-doping approach for wide-gap semiconductors: The case of p-type ZnO*", Physical Review Letters, **90**, 256401 (2003)
- [196] J. Furthmüller, F. Hachenberg, A. Schleife, D. Rogers, F. H. Teherani and F. Bechstedt, "*Clustering of N impurities in ZnO*", Applied Physics Letters, **100**, 022107 (2012)
- [197] T. M. Borseth, F. Tuomisto, J. S. Christensen, E. V. Monakhov, B. G. Svensson and A. Y. Kuznetsov, "*Vacancy clustering and acceptor activation in nitrogen-implanted ZnO*", Physical Review B, **77**, 045204 (2008)
- [198] J. Y. Zhu and S. H. Wei, "*Tuning doping site and type by strain: Enhanced p-type doping in Li doped ZnO*", Solid State Communications, **151**, 1437-1439 (2011)
- [199] S. Gangil, A. Nakamura, Y. Ichikawa, K. Yamamoto, J. Ishihara, T. Aoki and J. Temmyo, "*P-type nitrogen-doped ZnO thin films on sapphire (1 1 (2)over-bar-0) substrates by remote-plasma-enhanced metalorganic chemical vapor deposition*", Journal of Crystal Growth,

- 298**, 486-490 (2007)
- [200] Z. Z. Zhang, Z. P. Wei, Y. M. Lu, D. Z. Shen, B. Yao, B. H. Li, D. X. Zhao, J. Y. Zhang, X. W. Fan and Z. K. Tang, "*p-Type ZnO on sapphire by using O-2-N-2 co-activating and fabrication of ZnO LED*", *Journal of Crystal Growth*, **301**, 362-365 (2007)
- [201] D. C. Look, D. C. Reynolds, C. W. Litton, R. L. Jones, D. B. Eason and G. Cantwell, "*Characterization of homoepitaxial p-type ZnO grown by molecular beam epitaxy*", *Applied Physics Letters*, **81**, 1830-1832 (2002)
- [202] C. Czekalla, T. Nobis, A. Rahm, B. Q. Cao, J. Zuniga-Perez, C. Sturm, R. Schmidt-Grund, M. Lorenz and M. Grundmann, "*Whispering gallery modes in zinc oxide micro- and nanowires*", *Physica Status Solidi B-Basic Solid State Physics*, **247**, 1282-1293 (2010)
- [203] T. Nobis, E. M. Kaidashev, A. Rahm, M. Lorenz and M. Grundmann, "*Whispering gallery modes in nanosized dielectric resonators with hexagonal cross section*", *Physical Review Letters*, **93**, 103903 (2004)
- [204] W. Walukiewicz, "*Intrinsic limitations to the doping of wide-gap semiconductors*", *Physica B-Condensed Matter*, **302**, 123-134 (2001)

Acknowledgement

First of all I would like to thank my supervisor Prof. Dr. Jörg Weber for providing me the opportunity to perform this work in the HLP Laboratory for semiconductor physics in TU Dresden. This work would not have been done without his great support, guidance, inspiration and encouragement in the past four years. I still vividly remember that, there is one time; I received an email about the revise of my paper from Prof. Weber at 22:50 in late evening. I especially appreciate the freedom atmosphere he offered me as well as the way of doing research he taught me.

I gratefully thank Dr. Frank Herklotz for his kind help throughout the work. His efforts were contained into every aspects of my dissertation. I will never forget the long hours' discussions and overnight measurements together with him in the lab. I also thank Dr. Julien Dangbegnon for his great support in the furnace construction, thin film deposition and characterization.

I would like to thank Prof. Dr. Peer Schmidt for his willing agreement to referee this work.

I would like to express my thanks to all members in the chair of semiconductor physics. TU Dresden. Especially I thank Dr. Edward Lavrov for the interview by him when I came to Dresden for the first time and valuable discussions with him during the work. I thank PD. Dr. Ellen Hickenmann for microscopic characterizations. I thank Dr. Jiahe Chen for sharing his experience in scientific career. I thank Dr. Vladimir Kolkovsky and Leopold Scheffler for the support in electrical measurements. I thank Ms. Steffi Gerber for the kind and patient help when I met difficulties in German language. I thank Mr Berthold Köhler and Ms. Simone Behrendt for the support in technique problems. I thank Ronald Stübner for the translation of the abstract into German, In addition, My thank also goes to all other group members: Matthias Allardt, Karsten Kurasch, Sandro Koch, Dirk Bastin, Dr. Dietmar Temmler, and Yuri Kutin.

I thank my colleagues Jenny Eilers and Stefan Uhlig from Fraunhofer-IKTS (The Fraunhofer Institute for Ceramic Technologies and Systems) for the meaningful

discussions in the bimonthly seminars.

I would like to thank Mr. Diethart Langbein from the Gfe Freiberg GmbH for the making of ZnO and Al₂O₃ ceramic tubes.

Finally, I would like to express my deep appreciation to my Mom, Dad /(-in-law), family for their constant supports and encouragements. Especially I want to thank my beloved wife Jing Zhang for her love and tireless support which are always the most powerful motivation in my life.

I gratefully acknowledge the financial support from the European Regional Development Fund and the Free State of Saxony (SAB 14253/2423).

Erklärung

Diese Dissertation wurde am Institut für Angewandte Physik/Halbleiterphysik, Technische Universität Dresden unter der wissenschaftlichen Betreuung von Prof. Dr. Jörg Weber angefertigt.

Hiermit versichere ich, dass ich die vorliegende Arbeit ohne unzulässige Hilfe Dritter und ohne Benutzung anderer als der angegebenen Hilfsmittel angefertigt habe; die aus fremden Quellen direct oder indirect übernommen Gedanken sind als solche kenntlich gemacht. Die Arbeit wurde bisher weder im Inland noch im Ausland in gleicher oder ähnlicher Form einer anderen Prüfungsbehörde vorgelegt.

Ich erkenne die Promotionsordnung der Fakultät Mathematik und Naturwissenschaften an der Technische Universität Dresden vom 23.02. 2011 an.

.....

Xi Zhang, Dresden, 26.8.2013